

Development of Semicrystalline
Morphology of Poly(L-lactic acid) During
Processing of a Vascular Scaffold.

Thesis by
Artemis Ailianou

In Partial Fulfillment of the Requirements for the degree
of
Doctor of Philosophy



CALIFORNIA INSTITUTE OF TECHNOLOGY
Pasadena, California
2014
(Defended May 5, 2014)

© 2014
Artemis Ailianou
All Rights Reserved

ACKNOWLEDGEMENTS

There are many people who have contributed to my success at Caltech. First of all, I would like to thank my advisor Julie Kornfield, who believed in me from the beginning. Through Julie's mentoring I learned how to be a better scientist, a better communicator, and a better person overall. I would also like to thank my committee (Professors Bob Grubbs, David Tirrell, and Mikhail Shapiro) for spending the time to read and evaluate my dissertation.

I am indebted to Dr. Jim Oberhauser of Abbott Vascular for initiating and maintaining the collaborative research that is the topic of this dissertation, as well as overseeing the funding for it. I'm extremely grateful for Dr. Mary Beth Kossuth's mentoring and for answering all my questions about stents and scaffolds as I was trying to understand my data. Few graduate students have the opportunity to collaborate directly with industry and get a glimpse about what matters in the "real world"—I feel very lucky to be one of them.

I have been extremely lucky to have worked with two different groups of collaborators in my graduate student career. My first collaboration with Prof. Rastogi's group at Loughborough University gave me the opportunity to travel to the UK, Italy, France, The Netherlands, and Portugal for a combination of experiments and conferences and helped me build the foundations of my knowledge on polymer microstructure. I'm appreciative to Dr. Sara Ronca and Mr. Giuseppe Forte both for our collaborative scientific work on Ultra High Molecular Weight Polyethylene but also for their mentoring and lasting friendship. I acknowledge funding from the National Science Foundation – Materials World Network for providing the monetary support for all the travel during that project.

My work wouldn't have been possible without the support from several Caltech staff members and beamline scientists at National Labs. At Caltech, I would like to thank Mike Roy for always understanding my poorly drawn sketches when I needed to make a part; Joe Drew for being the go-to person when I needed to find things or have them fixed; Suresh Gupta for maintaining the computer cluster and server that I've used to analyze my data; Marcy Fowler, Andrea Arias, and Yvette Grant for trying to make the Kornfield group run as smoothly as possible (not an easy task!), and Kathy Bubash, who makes sure that all the

forms are signed and that all requirements are met from matriculation to graduation. For my X-ray scattering experiments, I'm grateful for the support of Drs. Lixia Rong and Lin Yang at Brookhaven National Lab, Drs. Alexander Hexemer, Nobumichi Tamura, Eric Schaible and Martin Kunz at Lawrence Berkeley National Lab, and Dr. Zhonghou Cai at Argonne National Lab. I'm especially appreciative of Dr. Tamura for taking some of his own time to perform proof of concept microdiffraction experiments for me, and Dr. Cai for helping me run my first microdiffraction experiments even when he had to wake up in the middle of the night.

The best part of my time at Caltech has been the people I met. I have been extremely lucky to share office and lab space with a wonderful group of colleagues. I still remember the first time I talked to Dr. Zuli Kurji when I was considering joining the Kornfield group. Zuli has been a mentor, a friend, a dance buddy, and one of the best people to have around during beamtime. Dr. Paul Pirogovsky joined the group the same time I did, but we didn't really bond until a neutron scattering beamtime a year after that. I need to thank Paul for helping me with all things electrical and mechanical in the lab, for helping me collect data during one of my many beamtimes, for many interesting conversations, and for commiserating about life as graduate students. Dr. Jeremy Wei was already a seasoned grad student when I joined the Kornfield group and has provided life advice along the way. Amy Fu and Boyu Li have become great friends, and even though we work on completely different projects we're still able to bounce ideas off each other (and do a fair amount of gossiping). I enjoyed many conversations with many other previous and current Kornfield group members including Dr. Loddie Foose, Dr. Ruoyu Zhang, Dr. Matthew Mattson, Akira Takagi, Dennis Ko, Karthik Ramanchandran, Yulan Lin, and Dan Zhou.

Outside the lab, I bonded with the incoming Chemical Engineering class of 2008 and made many friends through dancing with the Ballroom Dance and Ballet club, participating in the Graduate Student Council, and attending the free food events sponsored by the Center for Diversity, the office for International Student Programs, the Alumni Association, and the Caltech Y. I need to thank all the staff that made those programs possible, in particular Portia Harris of the Center for Diversity, and Laura Flower Kim and Daniel Yoder of the

International Student Programs. In no particular order, Dr. Heather McCaig, Dr. David Levitan, Dr. Nick Hoh, Dr. Christine Loza, Aileen Hui, and Casey Handmer have carried me through personal crises, illness, and difficult times at work, and they were there to celebrate successes, dance performances, and birthdays. My friends from college and high school kept me sane by reminding me that there's a different world outside Caltech. Esteban Hufstedler's love and support made the research for and writing of this dissertation possible.

Of course, none of this would have happened without the love and continuous encouragement from my parents and extended family. I'm very grateful that my parents never held me back from fulfilling my dreams even though it meant that I would live at least 7000 miles away from them for many years. Lastly, I want to acknowledge the influence of my paternal grandmother, Olga, who was one of the first women to attend the National Technical University of Athens, Greece and has inspired me with her intrepidness, her sharp mind, and creativity.

ABSTRACT

New and promising treatments for coronary heart disease are enabled by vascular scaffolds made of poly(L-lactic acid) (PLLA), as demonstrated by Abbott Vascular's bioresorbable vascular scaffold. PLLA is a semicrystalline polymer whose degree of crystallinity and crystalline microstructure depend on the thermal and deformation history during processing. In turn, the semicrystalline morphology determines scaffold strength and biodegradation time. However, spatially-resolved information about the resulting material structure (crystallinity and crystal orientation) is needed to interpret *in vivo* observations.

The first manufacturing step of the scaffold is tube expansion in a process similar to injection blow molding. Spatial uniformity of the tube microstructure is essential for the consistent production and performance of the final scaffold. For implantation into the artery, solid-state deformation below the glass transition temperature is imposed on a laser-cut subassembly to crimp it into a small diameter. Regions of localized strain during crimping are implicated in deployment behavior.

To examine the semicrystalline microstructure development of the scaffold, we employed complementary techniques of scanning electron and polarized light microscopy, wide-angle X-ray scattering, and X-ray microdiffraction. These techniques enabled us to assess the microstructure at the micro and nano length scale. The results show that the expanded tube is very uniform in the azimuthal and axial directions and that radial variations are more pronounced. The crimping step dramatically changes the microstructure of the subassembly by imposing extreme elongation and compression. Spatial information on the degree and direction of chain orientation from X-ray microdiffraction data gives insight into the mechanism by which the PLLA dissipates the stresses during crimping, without fracture.

Finally, analysis of the microstructure after deployment shows that it is inherited from the crimping step and contributes to the scaffold's successful implantation *in vivo*.

Acknowledgements	iii
Abstract.....	vi
Table of Contents	viii
List of Figures.....	ix
List of Tables	xi

Chapter 1: Introduction

1.1 Chemical structure and uses of poly(L-lactic acid)	I-1
1.2 Semicrystalline morphology of PLLA.....	I-2
1.3 Vascular scaffolds made of PLLA	I-5
1.4 Objective	I-8
1.5 Organization	I-8
References.....	I-9

Chapter 2: Axial, Azimuthal, and Radial Variation of PLLA Morphology After Tube Expansion

2.1 Introduction.....	II-1
2.2 Results.....	II-6
2.3 Discussion.....	II-16
2.4 Conclusions.....	II-19
2.5 Methods	II-20
References.....	II-25

Chapter 3: Effect of Crimping on Scaffold Morphology

3.1 Introduction.....	III-1
3.2 Results.....	III-4
3.3 Discussion.....	III-12
3.4 Conclusions.....	III-17
3.5 Methods	III-18
References.....	III-22

Chapter 4: Effect of Deployment on Scaffold Morphology

4.1 Introduction.....	IV-1
4.2 Results.....	IV-3
4.3 Discussion.....	IV-11
4.4 Conclusions.....	IV-15
4.5 Methods	IV-17
References.....	IV-22

Appendix A: Data Analysis code

A.1 Reduction of data to obtain $I(\Phi)$	A-1
A.2 Extraction of quantitative values from $I(\Phi)$	A-2
A.3 Function used to extract values from the $I(\Phi)$ curves	A-3

LIST OF FIGURES

<i>Figure</i>	<i>Page</i>
1.1 Ring-opening polymerization of L-lactic acid.....	I-1
1.2 Domains and dimensions of crystalline lamellae.....	I-3
1.3 Orthorhombic unit cell of PLLA's α form.....	I-4
1.4 Balloon angioplasty and stenting	I-6
2.1 Expanded tubing and as-cut subassembly.....	II-2
2.2 Schematic of specimen geometry.....	II-4
2.3 Relationship between of diffraction patterns and chain axis	II-5
2.4 Motivation for X-ray scattering experiments.....	II-7
2.5 Coarse grain view of the specimens under polarized light	II-7
2.6 Cropped polarized light micrographs of the specimens	II-8
2.7 Representative scattering pattern of PLLA specimens.....	II-9
2.8 Definition of quantities to characterize uniformity.....	II-11
2.9 Overview of X-scattering characterization results.....	II-14
2.10 Polarized light micrographs of thin W and Y sections.....	II-15
2.11 Polarized light micrographs of thin U sections.....	II-16
2.12 Image of an as-cut subassembly.....	II-20
2.13 Determination of Michel-Levy colors.....	II-22
2.14 Setup of beamline NSLS X9.....	II-24
3.1 Digital rendering of a crimped scaffold subassembly	III-2
3.2 Scanning Electron Micrographs of a crimped subassembly.....	III-4
3.3 SEM images of a microfissure on a single U crest	III-5
3.4 Polarized light micrographs of W and U sections	III-6
3.5 Orientation analysis of a W section.....	III-7
3.6 X-ray microdiffraction patterns for the area scan at the inner bend	III-9
3.7 Quantitative analysis of the area scan at the inner bend	III-10
3.8 Selected microdiffraction patterns acquired at crazes	III-11
3.9 Schematic of the polymer chain orientation evolution during crimping...	III-12
3.10 Schematic of the mechanism of lamellar rupture and fragment rotation.	III-16
3.11 Determination of U crest bend angle	III-19

3.12 Rotations of the thin U section under polarized light.....	III-20
3.13 Determination of orientation distribution with polarized light	III-21
4.1 Definition of inner and outer bends of the scaffold crests	IV-2
4.2 SEM of scaffolds subjected to failure <i>in vitro</i>	IV-4
4.3 High magnification SEM of diamond-shaped voids	IV-4
4.4 Polarized light micrographs of sections from deployed U	IV-5
4.5 Selected microdiffraction patterns at the outer bend of the U section	IV-7
4.6 Selected microdiffraction patterns at the arms of the U section.....	IV-8
4.7 Quantitative analysis of the line scans of the U section	IV-9
4.8 Selected microdiffraction patterns at the inner bend of the U section	IV-10
4.9 Schematic of the forces involved in deployment.....	IV-11
4.10 Chain orientation at the surfaces of a diamond-shaped void	IV-14
4.11 Schematic of formation mechanism of diamond-shaped voids	IV-15
4.12 Schematic of the intersection of the orientation and diffraction spheres.	IV-19
4.13 Schematic of the hexagonal (110) plane and it unit normal.....	IV-21

LIST OF TABLES

<i>Table</i>	<i>Page</i>
2.1 Variation of WAXS I_{\max} of the specimens	II-12
2.2 Variation of WAXS q-FWHM of the specimens	II-12
2.3 Variation of Φ -max of the specimens	II-13
2.4 Variation of Φ -FWHM of the specimens.....	II-13

CHAPTER 1

Introduction

1.1 Chemical structure and uses of poly(L-lactic acid)

Poly(L-lactic acid) (PLLA) is an aliphatic polyester made of lactic acid (2-hydroxy propionic acid) monomers. Lactic acid exists into two isomers: L(-) and D(+). The L(-) isomer is the most common form but the D(+) isomer can be produced by microorganisms or through racemization.¹ Industrial polymerization of lactic acid is typically done via ring opening polymerization (ROP) that yields a high molecular weight (>100,000 g/mol) polymer (Fig. 1.1)². The properties of a PLLA grade depend highly on the ratio of L- and D-isomers, and it is common practice to polymerize a controlled amount of the two isomers to tailor its properties for a specific application. Pure poly(L-lactic acid) (PLLA) is a semicrystalline polymer with 70% maximum achievable crystallinity, whereas poly(L-D-lactic acid) random copolymer is completely amorphous.

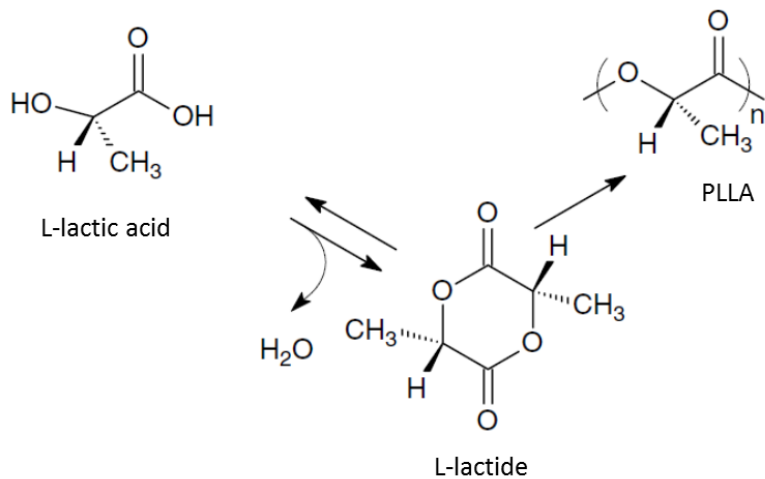


Figure 1.1 Ring-opening polymerization of L-lactic acid.

PLLA is considered a “green” polymer because it is biodegradable and its monomer can be made through fermentation of renewable plant sources, such as plant derived starch and sugars.³ Worldwide production of PLLA was 180,000 metric tons in 2012 and is expected to reach 800,000 by 2020.⁴ PLLA is a versatile polymer that can be processed with injection molding, sheet extrusion, blow molding, film forming, or fiber spinning to make consumer products such as films, bottles, and fibers for carpets and apparel^{1,5}. Because of its biocompatibility and biodegradation, PLLA can be used for medical applications. In 1966, the U.S. Army Medical Biomechanical Research Laboratory evaluated PLLA filaments, films, and coatings for use as surgical implants.⁶ Since then, PLLA has been used for fixing fractures in bones^{7–11}, sutures¹², endovascular implants^{13–15}, and even aesthetic medicine¹⁶.

1.2 Semicrystalline morphology of PLLA

Semicrystalline polymers have a nanostructure with both crystalline and amorphous domains (Fig. 1.2). The crystalline domains confer strength while the amorphous domains confer toughness and flexibility. The macroscopic properties of the material depend strongly on the fraction of crystalline material (degree of crystallinity), and on the morphology, spatial arrangement, size, and orientation distribution of the crystallites.

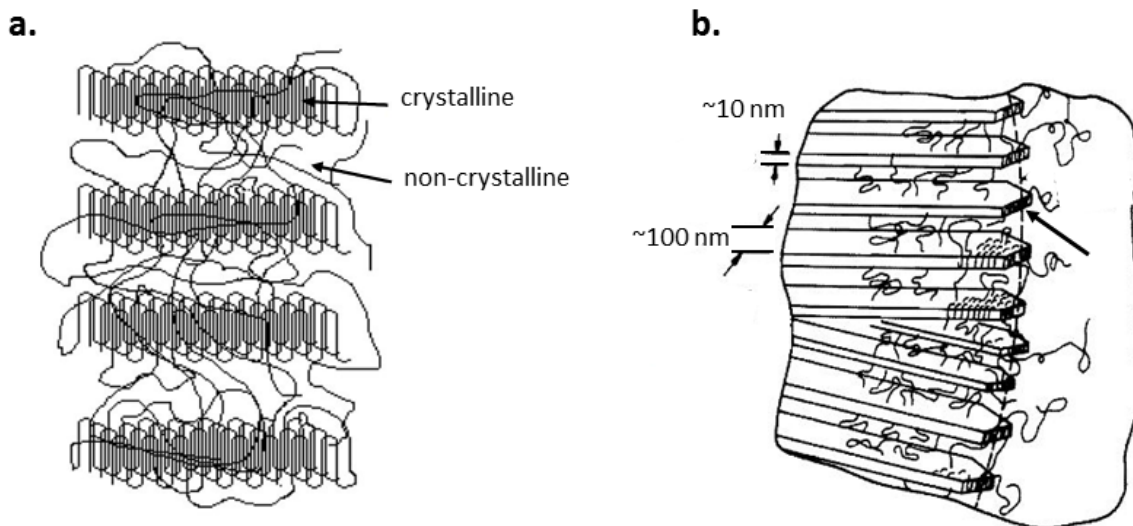


Figure 1.2 a) Schematic of crystalline and non-crystalline domains. Typical thickness of lamellar crystals is 10 nm. b) Enlarged view of the lamella/amorphous polymer interface. The leftmost arrow points at an individual lamella. Figure adapted from Shultz¹⁷.

Crystallites grow by reorganizing random-coil chains into platelet-like lamellae bounded by the inter-lamellar region and separated by regions of non-crystalline material. Lamellae form when polymer chains enter and re-enter the polymer crystal, which results in lamellar dimensions much smaller than the chain length (Fig. 1.3).

PLLA has four different crystal morphs: α , α' , β , and γ . The α morph forms during crystallization from the melt at temperatures above 120 °C or from solution. It has an orthorhombic unit cell with dimensions $a = 10.68 \text{ \AA}$, $b = 6.16 \text{ \AA}$, and c (fiber axis) = 28.86 \AA ¹⁸ (Fig. 1.3)¹. Initially thought of as a slightly disordered α phase, α' was first identified by Zhang *et al.*¹⁹ and determined that its unit cell is hexagonal with dimensions $a = b = 6.20 \text{ \AA}$, and $c = 28.80 \text{ \AA}$ ^{20,21}. A contradictory study by Wasanasuk *et al.* has reported

¹ There are several reported values for the dimensions of the α unit cell. The first reported values were $a = 10.70 \text{ \AA}$, $b = 6.45 \text{ \AA}$, and c (fiber axis) = 27.80 \AA ⁴³, but subsequent studies have reported dimensions of $a = 10.68 \text{ \AA}$, $b = 6.16 \text{ \AA}$, and $c = 28.86 \text{ \AA}$ ¹⁸, and $a = 10.5 \text{ \AA}$, $b = 6.1 \text{ \AA}$, and $c = 28.80 \text{ \AA}$ ⁴⁴. The accepted values are from Ref. 16.

that the α' unit cell is orthorhombic, with dimensions $a = 10.80 \text{ \AA}$, $b = 6.20 \text{ \AA}$, and $c = 28.80 \text{ \AA}^{22}$. The β morph forms when PLLA fibers are made through hot-drawing melt-spinning²³ or solution spinning²⁴, and it has an trigonal unit cell with dimensions $a = b = 10.52 \text{ \AA}$ and $c = 8.80 \text{ \AA}^{24}$. The γ morph forms by epitaxial crystallization on hexamethylbenzene at $155 \text{ }^\circ\text{C}$, and it has an orthorhombic unit cell with $a = 9.95$, $b = 6.25$, and $c = 8.80 \text{ \AA}$. For industrial applications other than fiber spinning and drawing, the α and α' morphs are the most relevant.

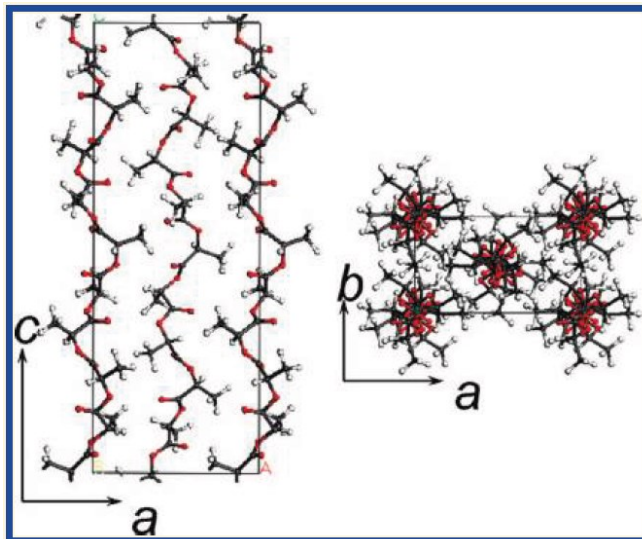


Figure 1.3 Schematic representation of the orthorhombic unit cell of PLLA's α form. See text for unit cell dimensions. Figure from Wasanasuk.¹⁸

The crystal polymorphism of PLLA has a large influence on its properties. For example, a high content in α morph results in high strength and high modulus but also, brittleness. Because industrial process like injection molding and film drawing are performed at temperatures that favor crystallization of the α morph, PLLA is often modified to suppress brittle behavior. Toughening of PLLA can be achieved by varying

the stereoisomer content^{25,26}, blending²⁷⁻²⁹, plasticizing³⁰⁻³², and copolymerizing³³. Brittleness can also be avoided by tailoring the crystalline/amorphous ratio and the degree of orientation by varying processing conditions, e.g. controlling the shear in injection molding³⁴ or changing the draw ratio of films^{35,36}.

Certain applications, e.g. medical implants, require pure PLLA, so toughness and high strength must be modulated by processing only. For manufacturing processes that involve strains in the solid state, a high content of α' to α is desired because it renders PLLA more ductile. Simultaneous wide-angle x-ray scattering and digital scanning calorimetry studies have shown that the α' to α transition happens in the solid state at temperatures between 100 and 120°C²¹ (above PLLA's glass transition temperature, $T_g \approx 60^\circ\text{C}$). Therefore, a high degree of crystallization and alignment of α' could only be achieved at relatively low temperatures, close to the T_g . However, little is known about the strain phase behavior of *pure* poly(L-lactic) acid near T_g .

1.3 Vascular scaffolds made of PLLA

Coronary heart disease is the leading cause of the death in the United States³⁷ and in the world³⁸. Coronary heart disease is associated with the narrowing of the arterial vessels due to the buildup of atherosomatic plaque. This results in hypertension, ischemia, angina, and in the case of compete occlusions, a heart attack. Lifestyle changes such as exercise and cessation of smoking and/or medication can lower the risk of heart attacks. Some patients might need a more aggressive treatment for revascularization, usually either coronary bypass surgery, or balloon angioplasty combined with stenting. In coronary bypass surgery, a vessel graft is used to bypass the occluded artery in order to restore blood

flow. In balloon angioplasty, an obstructed vessel is enlarged by compressing the atheromatic plaque against the vessel walls by means of an inflatable balloon. Stents are expandable slotted tubes that are implanted in the artery and provide support to the newly expanded vessel once the balloon is withdrawn (Fig 1.4).

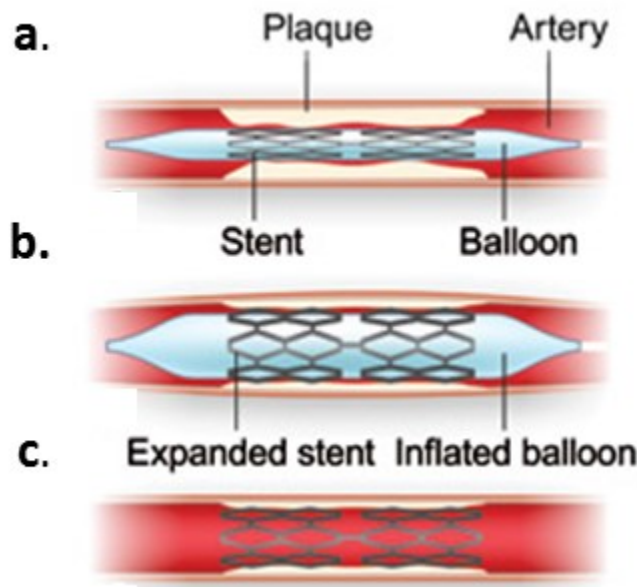


Figure 1.4 a) A stent on a balloon is delivered in the artery narrowed by atherosomatic plaque. b) The stent is expanded when the balloon is inflated, and it enlarges the diameter of the artery by pushing the plaque against the arterial walls. c) The balloon is removed but the stent remains to support the enlarged vessel.

Typically, stents are made of either bare metal (BMS), or they can be drug-eluting (DES). Even though they are generally safe, there are several concerns about their long-term performance. The biggest concern is late stent thrombosis due to continuous inflammation by the presence of a foreign body in the vessel. Furthermore, their stiffness prohibits restoration of regular vasomotion or further diameter enlargement, and their permanent nature makes any additional procedures in neighboring vessels more

challenging.³⁹ These concerns were considered, and temporary polymeric bioresorbable scaffolds were suggested as an alternative in 1988, only two years after the first metal stents had been implanted in humans.¹⁵ However, it took two decades of research before cardiovascular scaffolds were tested in human clinical trials¹⁵.

Bioresorbable polymeric scaffolds are both biodegradable and resorbable, i.e. their degradation products in the body enter metabolic pathways. PLLA is an excellent bioresorbable polymer because its monomer, lactic acid, is already produced by the body. Polymeric vascular scaffolds currently in development and clinical trials are made of PLLA, or PLLA copolymerized with other biocompatible polymers like poly(caprolactone) and poly(glycolic acid).⁴⁰ One of the most successful bioresorbable scaffolds, manufactured by Abbott Vascular, is made entirely out of PLLA and has already demonstrated the clinical safety and efficacy required to receive the CE mark⁴¹. The mechanical performance and hydrolytic degradation of the scaffold *in vivo* depends on its semicrystalline morphology, because amorphous domains are more susceptible to hydrolysis.¹ Additionally, the distribution and alignment of crystalline domains affects the strength of semicrystalline PLLA⁴². Therefore, in order to fully understand the *in vivo* performance of the scaffold we need to fully characterize the spatial distribution of microstructure of PLLA in the scaffold.

1.4 Objective

The manufacture and use of a poly(L-lactic acid) scaffold involves three key steps: tube expansion, crimping, and deployment. Tube uniformity during expansion is required for consistent scaffold performance across patients, whereas the crimping and deployment steps determine the scaffold's *in vivo* performance. Little is known about the effects of crimping on the morphology of metal stents, much less of polymeric scaffolds. The morphology after deployment depends highly on the semicrystalline morphology created during crimping, but until now there was no thorough investigation of the connection between the two. This thesis presents the results of the investigations on the microstructure evolution from tube expansion through deployment.

1.5 Organization

Chapter 2 employs polarized light microscopy (POM) and wide-angle X-ray diffraction to assess the axial, azimuthal, and radial variation of the expanded PLLA tube used to make the bioresorbable scaffold. The effects of crimping on semicrystalline morphology are studied with POM and X-ray microdiffraction and are presented in Chapter 3. In Chapter 4, the relationship between microstructure developed during crimping and deployment is presented.

References

- (1) Henton, D. E.; Gruber, P.; Lunt, J.; Randall, J. Natural Fibers, Biopolymers, and Biocomposites 16. Polylactic Acid Technology. In *Natural Fibers, Biopolymers, and Biocomposites*; 2005; pp. 527–578.
- (2) Lim, L.-T.; Auras, R.; Rubino, M. Processing Technologies for Poly(lactic Acid). *Prog. Polym. Sci.* **2008**, *33*, 820–852.
- (3) Inkinen, S.; Hakkarainen, M.; Albertsson, A.-C.; Södergård, A. From Lactic Acid to Poly(lactic Acid) (PLA): Characterization and Analysis of PLA and Its Precursors. *Biomacromolecules* **2011**, *12*, 523–532.
- (4) Carus, M. Growth in PLA bioplastics: a production capacity of over 800,000 tonnes expected by 2020 http://www.bioplasticsmagazine.com/en/news/meldungen/PLA_Growth.php.
- (5) Radjabian, M.; Kish, M. H.; Mohammadi, N. Structure–property Relationship for Poly(lactic Acid) (PLA) Filaments: Physical, Thermomechanical and Shape Memory Characterization. *J. Polym. Res.* **2012**, *19*, 9870.
- (6) Kulkarni, R. K.; Pani, K. C.; Neuman, C.; Leonard, F. *Polylactic Acid for Surgical Implants*; Washington, D.C., 1966; pp. 4–17.
- (7) Leenslag, J. W.; Pennings, A. J.; Bos, R. R. M.; Rozema, F. R.; Boering, G. Resorbable Materials of poly(L-Lactide). VI. Plates and Screws for Internal Fracture Fixation. *Biomaterials* **1987**, *8*, 70–73.
- (8) Kinoshita, Y.; Kirigakubo, M.; Kobayashi, M.; Tabata, T.; Shimura, K.; Ikada, Y. Study on the Efficacy of Biodegradable poly(L-Lactide) Mesh for Supporting Transplanted Particulate Cancellous Bone and Marrow: Experiment Involving Subcutaneous Implantation in Dogs. *Biomaterials* **1993**, *14*, 729–736.
- (9) Howard, D.; Partridge, K.; Yang, X.; Clarke, N. M. P.; Okubo, Y.; Bessho, K.; Howdle, S. M.; Shakesheff, K. M.; Oreffo, R. O. C. Immunoselection and Adenoviral Genetic Modulation of Human Osteoprogenitors: In Vivo Bone Formation on PLA Scaffold. *Biochem. Biophys. Res. Commun.* **2002**, *299*, 208–215.
- (10) Bos, R. R.; Rozema, F. R.; Boering, G.; Nijenhuis, a J.; Pennings, a J.; Verwey, a B.; Nieuwenhuis, P.; Jansen, H. W. Degradation of and Tissue Reaction to Biodegradable poly(L-Lactide) for Use as Internal Fixation of Fractures: A Study in Rats. *Biomaterials* **1991**, *12*, 32–36.
- (11) Hasegawa, Y.; Sakano, S.; Iwase, T.; Warashina, H. The Long-Term Behavior of Poly-L-Lactide Screws in a Minipig Fracture Model: Preliminary Report. *J. Biomed. Mater. Res.* **2002**, *63*, 679–685.

(12) Heino, A.; Naukkarinen, A.; Kulju, T.; Törmälä, P.; Pohjonen, T.; Mäkelä, E. A. Characteristics of poly(L-Lactic Acid) Suture Applied to Fascial Closure in Rats. *J. Biomed. Mater. Res.* **1996**, *30*, 187–192.

(13) Venkatraman, S.; Boey, F.; Lao, L. L. Implanted Cardiovascular Polymers: Natural, Synthetic and Bio-Inspired. *Prog. Polym. Sci.* **2008**, *33*, 853–874.

(14) Sarno, G.; Bruining, N.; Onuma, Y.; Garg, S.; Brugaletta, S.; De Winter, S.; Regar, E.; Thuesen, L.; Dudek, D.; Veldhof, S.; et al. Morphological and Functional Evaluation of the Bioresorption of the Bioresorbable Everolimus-Eluting Vascular Scaffold Using IVUS, Echogenicity and Vasomotion Testing at Two Year Follow-up: A Patient Level Insight into the ABSORB A Clinical Trial. *Int. J. Cardiovasc. Imaging* **2012**, *28*, 51–58.

(15) Thatcher, L. G. Endovascular Stents. In *Polymers for Vascular and Urogenital applications*; Shalaby, S.; Burg, K. J. L.; Shalaby, W., Eds.; CRC Press: Boca Raton, FL, 2012; pp. 89–116.

(16) Sculptra Aesthetic is Different in the way that it Works
<http://www.sculptraaesthetic.com/consumer/how-is-sculptra-aesthetic-different.aspx>.

(17) Shultz, J. M. *Polymer Crystallization*; Oxford University Press: Washington,, D.C., 2001.

(18) Wasanasuk, K.; Tashiro, K.; Hanesaka, M.; Ohhara, T.; Kurihara, K.; Kuroki, R.; Tamada, T.; Ozeki, T.; Kanamoto, T. Crystal Structure Analysis of Poly (L -Lactic Acid) Alpha Form On the Basis of the 2-Dimensional Wide-Angle Synchrotron X-Ray and Neutron Diffraction Measurements. *Macromolecules* **2011**, *44*, 6441–6452.

(19) Zhang, J.; Duan, Y.; Sato, H.; Tsuji, H.; Noda, I.; Yan, S.; Ozaki, Y. Crystal Modifications and Thermal Behavior of Poly L -Lactic Acid) Revealed by Infrared Spectroscopy. *Macromolecules* **2005**, *38*, 8012–8021.

(20) Kawai, T.; Rahman, N.; Matsuba, G.; Nishida, K.; Kanaya, T.; Nakano, M.; Okamoto, H.; Kawada, J.; Usuki, A.; Honma, N.; et al. Crystallization and Melting Behavior of Poly (L-Lactic Acid). *Macromolecules* **2007**, *40*, 9463–9469.

(21) Zhang, J.; Tashiro, K.; Tsuji, H.; Domb, A. J. Disorder-to-Order Phase Transition and Multiple Melting Behavior of Poly (L -Lactide) Investigated by Simultaneous Measurements of WAXD and DSC. *Macromolecules* **2008**, *41*, 1352–1357.

(22) Wasanasuk, K.; Tashiro, K. Crystal Structure and Disorder in Poly(l-Lactic Acid) Δ Form (α' Form) and the Phase Transition Mechanism to the Ordered A Form. *Polymer* **2011**, *52*, 6097–6109.

(23) Hoogsteen, W.; Postema, A. R.; Pennings, A. J.; Ten Brinke, G.; Zugenmaier, P. Crystal Structure, Conformation and Morphology of Solution-Spun poly(L-Lactide) Fibers. *Macromolecules* **1990**, *23*, 634–642.

(24) Puiggali, J.; Ikada, Y.; Tsuji, H.; Cartier, L.; Okihara, T.; Lotz, B. The Frustrated Structure of Poly (L-Lactide). *Polymer* **2000**, *41*, 8921–8930.

(25) Tsuji, H.; Ikada, Y. Stereocomplex Formation between Enantiomeric Poly(lactic Acid)s. XI. Mechanical Properties and Morphology of Solution-Cast Films. *Polymer* **1999**, *40*, 6699–6708.

(26) Fujita, M.; Sawayanagi, T.; Abe, H.; Tanaka, T.; Iwata, T.; Ito, K.; Fujisawa, T.; Maeda, M. Stereocomplex Formation through Reorganization of Poly (L-Lactic Acid) and Poly (D-Lactic Acid) Crystals. *Macromolecules* **2008**, *41*, 2852–2858.

(27) Bai, H.; Xiu, H.; Gao, J.; Deng, H.; Zhang, Q.; Yang, M.; Fu, Q. Tailoring Impact Toughness of poly(L-Lactide)/poly(ϵ -Caprolactone) (PLLA/PCL) Blends by Controlling Crystallization of PLLA Matrix. *ACS Appl. Mater. Interfaces* **2012**, *4*, 897–905.

(28) Bai, H.; Huang, C.; Xiu, H.; Gao, Y.; Zhang, Q.; Fu, Q. Toughening of Poly(l-Lactide) with Poly(ϵ -Caprolactone): Combined Effects of Matrix Crystallization and Impact Modifier Particle Size. *Polymer* **2013**, *54*, 5257–5266.

(29) Rathi, S.; Chen, X.; Coughlin, E. B.; Hsu, S. L.; Golub, C. S.; Tzivanis, M. J. Toughening Semicrystalline Poly(lactic Acid) by Morphology Alteration. *Polymer* **2011**, *52*, 4184–4188.

(30) Saeidlou, S.; Huneault, M. a.; Li, H.; Park, C. B. Poly(lactic Acid) Crystallization. *Prog. Polym. Sci.* **2012**, *37*, 1657–1677.

(31) Kulinski, Z.; Piorkowska, E.; Gadzinowska, K.; Stasiak, M. Plasticization of poly(L-Lactide) with Poly(propylene Glycol). *Biomacromolecules* **2006**, *7*, 2128–2135.

(32) Liu, H.; Zhang, J. Research Progress in Toughening Modification of Poly(lactic Acid). *J. Polym. Sci. Part B Polym. Phys.* **2011**, *49*, 1051–1083.

(33) Cho, J.; Baratian, S.; Kim, J.; Yeh, F.; Hsiao, B. S.; Runt, J. Crystallization and Structure Formation of Poly (L -Lactide- Co - Meso -Lactide) Random Copolymers: A Time-Resolved Wide- and Small-Angle X-Ray Scattering Study. *Polymer* **2003**, *44*, 711–717.

(34) Ghosh, S.; Viana, J. C.; Reis, R. L.; Mano, J. F. Oriented Morphology and Enhanced Mechanical Properties of Poly(l-Lactic Acid) from Shear Controlled Orientation in Injection Molding. *Mater. Sci. Eng. A* **2008**, *490*, 81–89.

(35) Smith, P. B.; Leugers, A.; Kang, S.; Hsu, S. L.; Yang, X.; Al, S. E. T. An Analysis of the Correlation between Structural Anisotropy and Dimensional Stability for Drawn Poly(lactic Acid) Films. *J. Appl. Polym. Sci.* **2001**, *82*, 2497–2505.

(36) Wong, Y. S.; Stachurski, Z. H.; Venkatraman, S. S. Orientation and Structure Development in Poly(lactide) under Uniaxial Deformation. *Acta Mater.* **2008**, *56*, 5083–5090.

(37) Hoyert, D.; Hu, J. *National Vital Statistics Reports Deaths : Preliminary Data for 2011; 2012*; Vol. 61, pp. 1–52.

(38) Mackay, J.; Mensah, G. A. *Deaths from Coronary Heart Disease*; 2004; pp. 48–49.

(39) Onuma, Y.; Ormiston, J.; Serruys, P. W. Bioresorbable Scaffold Technologies. *Circ. J.* **2011**, *75*, 509–520.

(40) Onuma, Y.; Serruys, P. W. Bioresorbable Scaffold: The Advent of a New Era in Percutaneous Coronary and Peripheral Revascularization? *Circulation* **2011**, *123*, 779–797.

(41) Abbott Announces International Launch of the AbsorbTM Bioresorbable Vascular Scaffold <http://www.abbott.com/news-media/press-releases/abbott-announces-international-launch-of-the-absorb-bioresorbable-vascular-scaffold.htm>.

(42) Dias, J. C.; Ribeiro, C.; Sencadas, V.; Botelho, G.; Ribelles, J. L. G.; Lanceros-Mendez, S. Influence of Fiber Diameter and Crystallinity on the Stability of Electrospun Poly(l-Lactic Acid) Membranes to Hydrolytic Degradation. *Polym. Test.* **2012**, *31*, 770–776.

(43) Kalb, B.; Pennings, a. J. General Crystallization Behaviour of Poly(l-Lactic Acid). *Polymer* **1980**, *21*, 607–612.

(44) Kobayashi, J.; Asahi, T.; Ichiki, M.; Oikawa, a.; Suzuki, H.; Watanabe, T.; Fukada, E.; Shikinami, Y. Structural and Optical Properties of Poly Lactic Acids. *J. Appl. Phys.* **1995**, *77*, 2957.

Chapter 2

Axial, Azimuthal, and Radial Variation of PLLA Morphology After Tube Expansion

2.1 Introduction

New and promising treatments for coronary heart disease are enabled by vascular scaffolds made of poly(L-lactic acid) (PLLA)¹ as demonstrated by Abbott's Bioresorbable Vascular Scaffold (BVS, Fig 2.1).² Clinical performance of PLLA scaffolds depends on the uniformity of structure within a given scaffold and the uniformity across batches of multiple scaffolds. Consistent microstructure and wall thickness of the tube are required for even deployment, uniform acute radial strength, and structural integrity^{2,3} after implantation in the artery. PLLA is a semicrystalline polymer whose degree of crystallinity and crystalline microstructure depend on the thermal and deformation history during processing.⁴⁻⁸ In turn, the semicrystalline morphology determines scaffold strength and biodegradation time.^{9,10} A key processing step that affects the axial, azimuthal, and radial variations of structure in BVS is the expansion of an extruded tube of PLLA into the thin-walled tube from which the scaffolds are cut.

The expanded tube is produced in a process similar to stretch-blow molding: an extruded tube "preform" is placed in a mold; compressed air is admitted into the preform; the preform is heated from room temperature to a temperature above the glass transition to allow for stretching driven by the elevated pressure inside the preform and axial tension applied to the distal end of the preform; and the expansion process is complete once the

preform's outer diameter (OD) reaches the inner diameter (ID) of the mold. Typically, the axial elongational strain is 20% and the azimuthal elongational strain is approximately 400% (greater for material elements near the ID than for those near the OD). The resulting expanded tube is then removed from the mold, ready to be laser-cut into "as-cut" subassemblies (Fig. 2.1). Controlling this tube-expansion process—and hence, the tube material properties—is crucial for consistent scaffold performance across all patients.

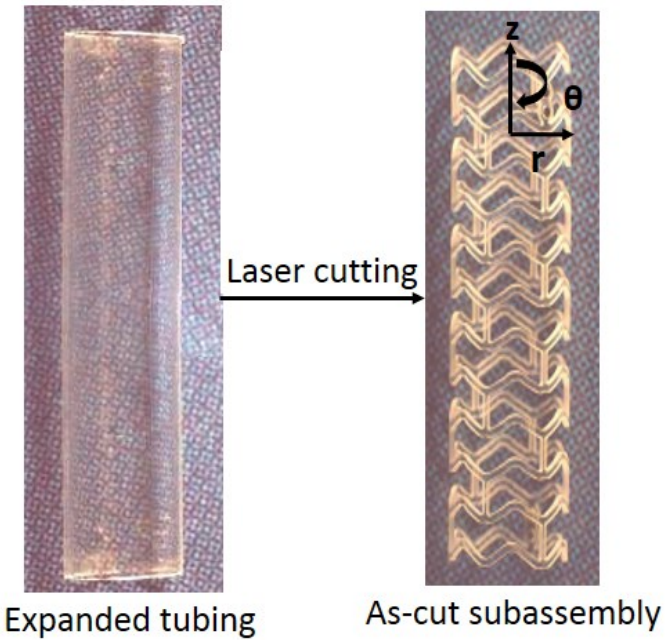


Figure 2.1: The expanded tube is laser cut into the as-cut subassembly (3 mm dia. and 18 mm long). Struts are 200 microns wide and 150 microns thick. Cylindrical coordinates are used: $z \equiv$ axial, $\theta \equiv$ azimuthal, and $r \equiv$ radial. Images provided by Abbott Vascular.

Similar to stretch blow molding¹¹, the expansion process drives strain-induced polymer crystallization. The expansion deforms the polymeric material most strongly in the azimuthal direction, leading to a preferential orientation of the molecular axis of the PLLA chains around the tube circumference, which imparts high resistance to radial loading.⁸ The expanded tubing is more crystalline than the extruded tubing, and therefore

has higher strength and better dimensional stability.⁸ Blow molding of semicrystalline polymers is an intricate process that is performed near the glass transition temperature (PLLA has T_g of 58 - 68°C^{12,13}), where viscoelastic properties have a strong, nonlinear temperature dependence, and involves competing rates of heating, deformation, crystallization, and cooling.¹⁴ Further challenges are present when the material is PLLA and the product is a vascular scaffold. The walls of the current generation BVS are 150 μm thick, imposing unusually tight tolerances¹⁵ (cf., beverage bottles), and the viscoelastic properties of PLLA are sensitive to small variations in, for example, water content¹⁶. Therefore, it is particularly important to characterize the variations of structure after the tubing expansion process.

Here, a combination of polarized light microscopy and synchrotron X-ray scattering is used to examine variations in PLLA morphology after the expansion process. Crystalline and glassy domains in PLLA are interspersed on a scale of tens of nanometers. Of PLLA's four different crystal morphs, only α and α' , which have only recently been distinguished¹⁷, are found in the scaffold. Polarized light microscopy provides a large-scale overall view of variations in structure over distances as large as 10 mm. The resulting overview guides the selection of points at which to use synchrotron x-ray scattering to observe important aspects of the nanostructure (e.g., relative amount of crystalline material, relative amount of α vs α' crystallites, crystallite orientation direction, and distribution).

We studied the axial and azimuthal variations using four specimens from the same the expanded tube; to keep track of their original axial positions, the specimens were labeled A, B, C, and D (Figure 2.2). Each specimen was laser cut to create eight equally spaced axial beams with center-to-center azimuthal separation of 45° (Fig. 2.2, middle). To

keep track of the azimuthal position, a black line was drawn on the same azimuthal location on all four specimens and was assigned the $\theta = 0^\circ$ position.

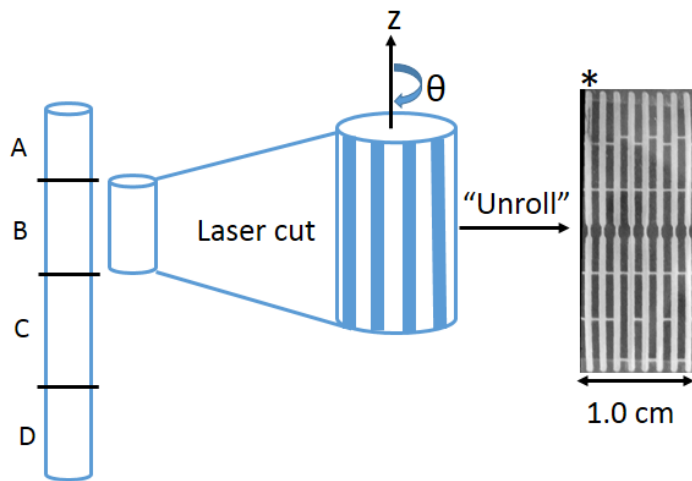


Figure 2.2 Schematic of specimen geometry. An expanded tube (left) is laser cut into four specimens (A-D). Each specimen is laser-cut to create eight, equally spaced axial beams (center) with azimuthal separation of 45° ; the asterisk indicates the assigned $\theta = 0^\circ$ position. The specimens are then “unrolled” (right) and examined with polarized light microscopy and X-ray scattering. Each beam is 25 mm long, 0.6 mm wide, and 150 μm thick.

X-ray scattering characterization has been used to decipher the structure PLLA. For the temperature and pressure conditions of the tube expansion, only the α and α' crystal morphs are relevant. The α' to α ratio determines yielding behavior; high content in α phase results in a more brittle material.⁷ The tube expansion process is done at a range of temperatures where the α phase is very brittle, so a high content of α' is desired. Furthermore, scaffold deployment requires a high elastic modulus, so the high content in α' must be maintained through the rest of the processing steps.

The x-ray diffraction peaks of the α phase are the (103), (010), (015), (110)/(200), (203), (204), and (207). However, for the α' phase, the observed peaks are the (010), (110)/(200), (203), and (206).¹⁸ The (206) peak is extremely important because the peak

becomes more prominent upon deformation, and is related to the fact that α' doesn't readily transform to α at low temperatures.¹⁹ It is important to note that the dimensions of [110] and [200] planes are only slightly different between the two phases. A slight shift toward low q indicates a higher content of α . The most accepted unit cell dimensions for the orthorhombic α phase are $a = 10.68 \text{ \AA}$; $b = 6.17 \text{ \AA}$; $c = 28.86 \text{ \AA}$ ²⁰, and for the hexagonal α' phase $a = b = 6.20 \text{ \AA}$; $c = 28.80 \text{ \AA}$ ^{17,21}.

The orientation of the (110)/(200) peak indicates the primary orientation axis of an expanded tube, with crystals preferentially oriented with the chain axis in the circumferential direction (black arrow, Figure 2.3a). In our data analysis we extracted quantitative information for the q range of $0.6 - 2.0 \text{ \AA}^{-1}$ (Fig. 2.3).

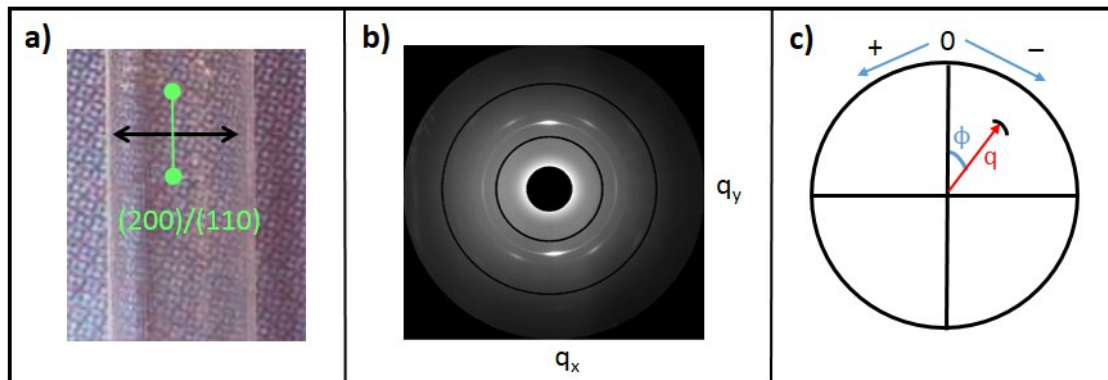


Figure 2.3 a) Schematic diagram showing the relationship between the (110)/(200) peaks (circles on the vertical dumbbell) and the chain axis direction (black arrow) relative to the expanded PLLA tube. b) A representative wide-angle scattering pattern (NSLS X27C) showing the q -range of quantitative analysis (inner and outer circles represent $q = 0.6$ and $q = 2.0 \text{ \AA}^{-1}$, respectively). The two brightest peaks at $q = 1.170 \text{ \AA}^{-1}$ correspond to the (110)/(200) crystal planes. c) Definition of the peak position in terms of the magnitude of the scattering vector, q , and the orientation angle, ϕ (black arc represents a peak). When the (110)/(200) diffraction peaks are oriented along the 0° line (green circles in (a); dominant peaks in (b); ϕ defined in (c)), the polymer chains are oriented in the 90° line.

2.2 Results

2.2.1 Azimuthal and axial variations of the expanded tube

Polarized light examination

All specimens were examined between crossed circular polarizers to survey the variations in orientation in the axial and azimuthal directions (defined in Fig. 2.2). To more accurately record the Michel-Levy colors, each axial beam was examined through crossed linear polarizers in a Zeiss Universal microscope. To assign a retardance value to the observed colors, the shift of the observed colors was analyzed when quarter-wave and full-wave retardation plates were inserted with their orientation along and orthogonal to the axial (z) direction of the PLLA beam. The Michel-Levy chart (Fig. 2.4, right) was used to determine the retardance values. A coarse-grained overview and high quality polarized light micrographs of specimens A-D are shown in Figs. 4 and 5, respectively.

The coarse-grained views of the specimens (Fig. 2.5) show that small variations are predominantly in the azimuthal position; axial variations are even milder. High quality polarized light micrographs (Fig. 2.6) show that the specimens are, in fact, consistent with each other.

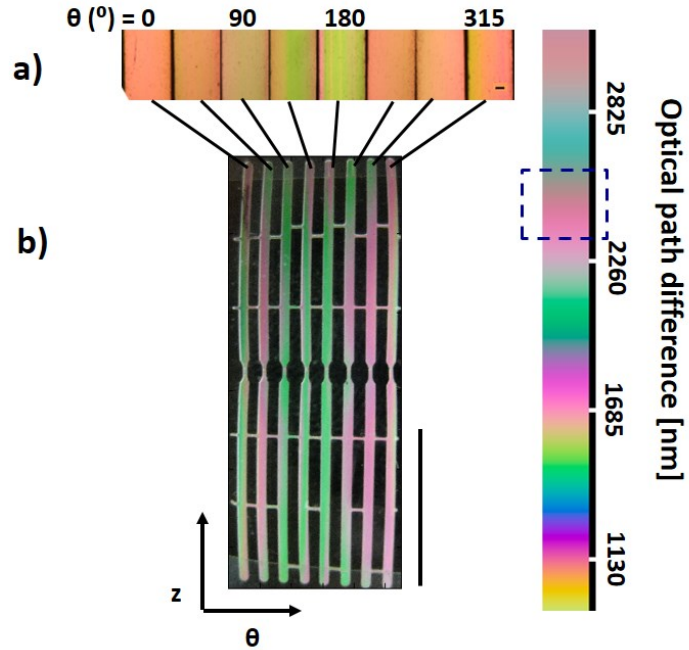


Figure 2.4 Motivation for X-ray scattering experiments. a) Cropped images of specimen D acquired in a Zeiss Universal microscope at 4X magnification through crossed linear polarizers equipped with a Canon DS30 digital camera. Based on the Michel-Levy color chart on the right, the optical path difference is 2300-2500 nm. Scale bar is 100 μ m. b) Coarse-grained view of specimen D acquired with a Canon PowerShot SD770 IS camera through crossed circular polarizers. Scale bar is 1.0 cm.

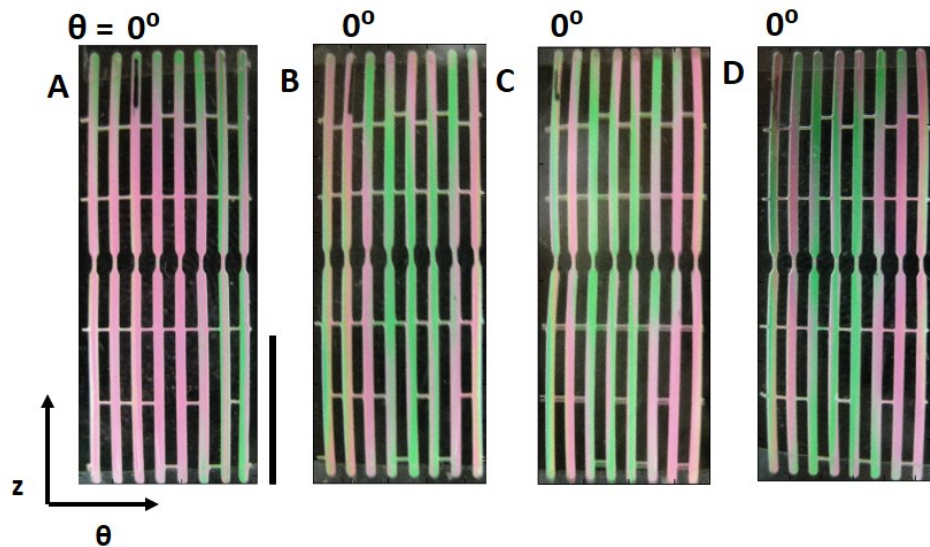


Figure 2.5 Coarse-grain view of the four specimens acquired with a Canon PowerShot SD770 IS camera through crossed circular polarizers. They were cut from the same tube, as shown in Fig. 2.2. All 0° positions are at the same azimuthal position of the expanded tube; the other segments were cut every 45°. Scale bar is 1.0 cm

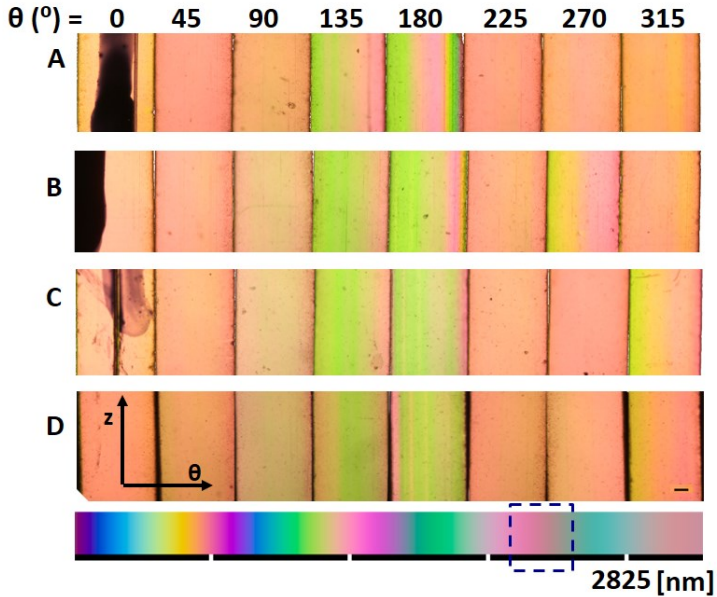


Figure 2.6 Cropped polarized light micrographs of the top edges of specimens A-D between crossed linear polarizers. The azimuthal position of the segments increases from left to right (Fig. 5, A-D). The Michel Levy color chart shows that the optical path difference is 2300-2500 nm. Scale bar is 100 μ m.

Synchrotron X-ray scattering characterization

To characterize the crystalline microstructure of the specimens, we considered the following quantities: I_{\max} , q_{\max} , q -FWHM, crystallinity index, Φ_{\max} , and Φ -FWHM (Fig. 6 shows the definition of the angle Φ for the (110)/(200) peak on the 2D scattering pattern—not to be confused with the scattering angle 2θ). Because all our specimens come from the same batch of material and display the same kind of anisotropy, Φ -FWHM can be used as an orientation strength index and q -FWHM as a measure of crystal perfection.²²

Scattering patterns acquired at both X27C and X9 of the National Synchrotron Light Source, Brookhaven National Lab, have (110/200), (203), and (206) peaks (Fig. 2.7), but no signs of the (103) and (204) peaks. Thus, the dominant crystal phase in the specimens is α' . At the q value of the (110)/(200) peak there are two bright peaks in the meridional direction (one indicated by the red arrow) and two weak peaks in the equatorial

direction. Physically, this corresponds to specimens that are biaxially oriented and have chain orientation axis predominantly in the azimuthal direction and a secondary orientation axis in the axial direction.²³⁻²⁵

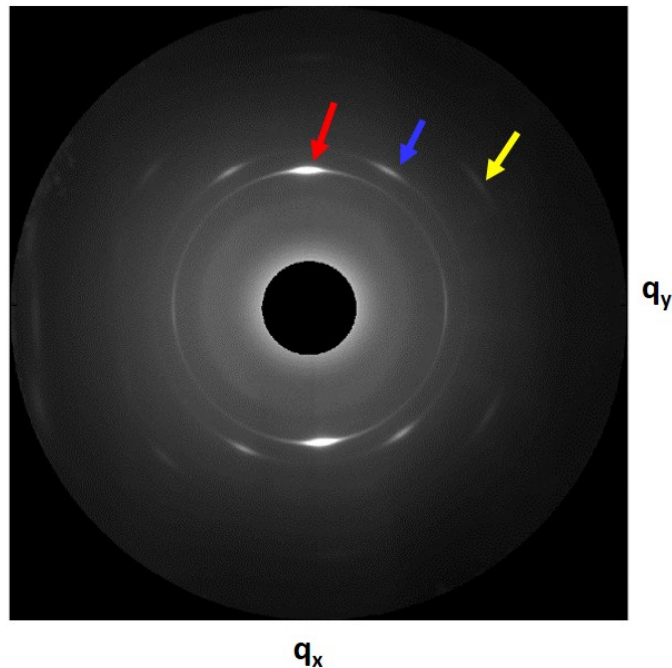


Figure 2.7 Representative scattering pattern of the PLLA specimens acquired at NSLS X27C. The different color arrows point out the three main peaks. From the center out, (110)/(200) peak at $q = 1.17 \text{ \AA}^{-1}$ (red arrow), (203) peak at $q = 1.34 \text{ \AA}^{-1}$ (blue arrow), and (206) peak at $q = 1.78 \text{ \AA}^{-1}$ (yellow arrow).

Small- and wide-angle X-ray scattering data were acquired at NSLS X9. Unfortunately, the SAXS signal was overwhelmed by the Kapton substrate supporting the specimens, precluding further analysis. Therefore, only WAXD data are analyzed to characterize uniformity of specimens A, C, and D (Figure 2.2; time constraints did not allow characterization of specimen B). Only one WAXS quadrant was available due to the special setup of the beamline²⁶ (Fig. 2.16). The q_{\max} for (110)/(200) in every diffraction pattern was 1.17 \AA^{-1} , with negligible standard deviation ($1 \times 10^{-15} \text{ \AA}^{-1}$). The absence of variations in the wavevector of the (110)/(200) peak indicates that the relative amount of

the α and α' phases is relatively constant. The values for I_{\max} , q -FWHM (Figure 2.8), crystallinity index, Φ_{\max} , and Φ -FWHM (Figure 2.8b, Φ defined in Fig. 2.6) were extracted from 88 scattering patterns per specimen (11 z-positions along each of the 8 beams). The mean and standard deviation for the 11 Z-positions on a given beam are given in Tables 2.1-2.4 (rows with azimuthal position of the beam). Variations in the axial direction are evident in the comparison of specimens A, C, and D (averages over all the beams in each specimen are in the last row of each Table). A visual representation of the data in the tables shows how small the variations are (Figure 2.9).

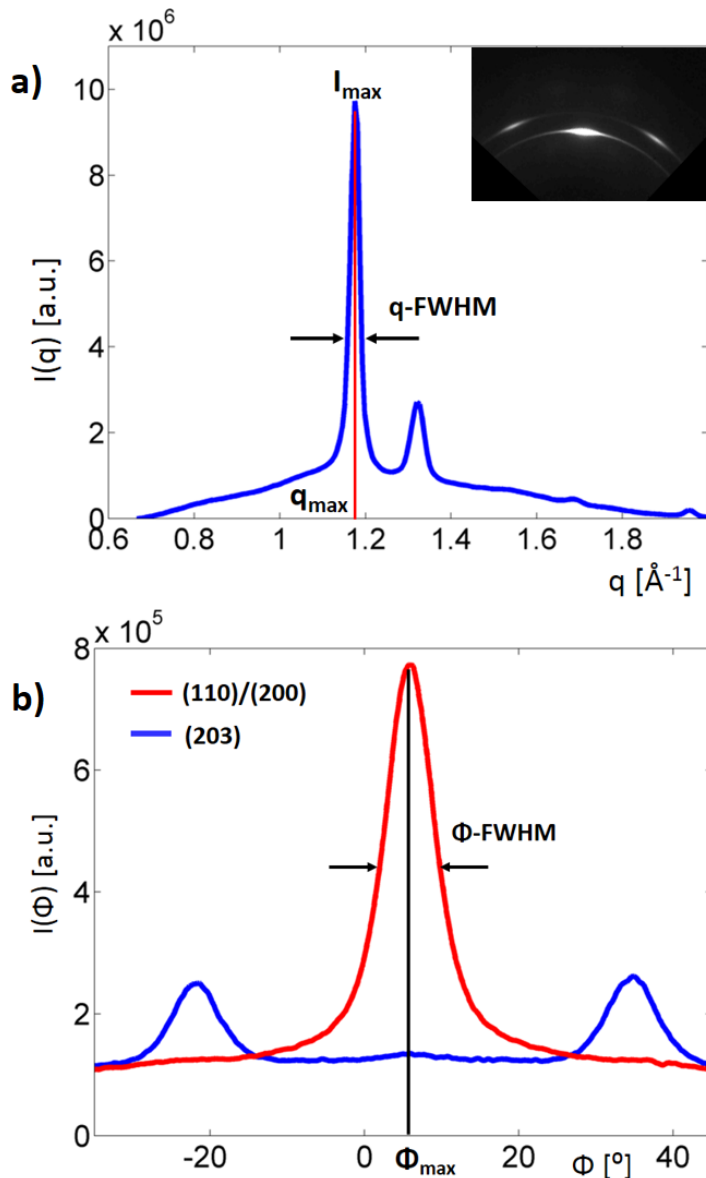


Figure 2.8 Definition of quantities used to characterize uniformity. a) Inset: Representative scattering pattern of the PLLA specimens from NSLS X9. Only the quadrant shown above was acquired due to the beamline setup. Graph: A representative $I(q)$ curve. The quantities I_{\max} , q_{\max} , and $q\text{-FWHM}$ are defined. b) A representative $I(\Phi)$ curve. The quantities Φ_{\max} , and $\Phi\text{-FWHM}$ are defined. The $I(\Phi)$ curve has only one peak because only one quadrant is available (full pattern has two).

The variation in WAXS I_{\max} , $q\text{-FWHM}$, Φ_{\max} , and $\Phi\text{-FWHM}$ in the axial and azimuthal direction are presented in tables 2.1-2.4. Figure 2.9 summarizes the tables 2.1, 2.3, and 2.4.

Table 2.1: Variation of WAXS I_{\max} for each axial beam of specimens A, C, and D.

θ position [$^{\circ}$] ²	I_{\max} [counts $\times 10^{-6}$] ¹		
	A	C	D
0	10.6 ± 0.4	9.6 ± 0.1	8.9 ± 0.3
45	10.0 ± 0.4	9.3 ± 0.9	8.6 ± 0.3
90	10.0 ± 0.4	9.6 ± 0.8	8.8 ± 0.4
135	10.5 ± 0.4	10.2 ± 0.7	9.8 ± 0.4
180	10.7 ± 0.5	10.8 ± 0.2	10.5 ± 0.3
225	10.6 ± 0.7	10.7 ± 0.2	10.1 ± 0.3
270	11.7 ± 0.2	11.0 ± 0.2	9.5 ± 0.3
315	12.9 ± 0.2	10.2 ± 0.1	9.2 ± 0.3
Average	11.0 ± 0.1	10.2 ± 0.1	9.4 ± 0.7

Table 2.2: Variation of WAXS q-FWHM for each axial beam of specimens A, C, and D.

θ position [$^{\circ}$]	q-FWHM [$\text{\AA}^{-1} \times 10^{-2}$]		
	A	C	D
0	3.06 ± 0.03	2.93 ± 0.05	3.01 ± 0.02
45	3.04 ± 0.03	2.86 ± 0.05	2.94 ± 0.04
90	3.02 ± 0.03	2.91 ± 0.08	2.85 ± 0.04
135	3.05 ± 0.02	2.93 ± 0.05	2.90 ± 0.04
180	2.82 ± 0.03	3.00 ± 0.06	3.06 ± 0.03
225	2.94 ± 0.08	2.96 ± 0.07	2.98 ± 0.04
270	2.92 ± 0.03	2.98 ± 0.05	2.95 ± 0.03
315	3.04 ± 0.03	3.00 ± 0.06	3.07 ± 0.02
Average	2.98 ± 0.09	2.94 ± 0.07	2.97 ± 0.01

¹ Each cell of the table represents the average and mean from 11 measurements² θ position defined in Fig. 2.3.

Table 2.3: Variation of Φ_{\max} for each axial beam of specimens A, C, and D.

	$\Phi_{\max}, [{}^{\circ}]$		
	A	C	D
0	-2.2 \pm 0.4	-1.1 \pm 1.0	0.0 \pm 0.7
45	-3.5 \pm 0.2	-1.0 \pm 0.8	-2.3 \pm 0.5
90	0.0 \pm 0.5	0.8 \pm 0.4	-0.9 \pm 0.8
135	1.3 \pm 0.6	0.3 \pm 0.8	0.7 \pm 0.9
180	-0.8 \pm 0.5	-1.4 \pm 1.5	-0.3 \pm 0.7
225	-3.8 \pm 1.0	-1.5 \pm 0.9	-2.2 \pm 0.8
270	0.1 \pm 0.6	1.6 \pm 0.6	-0.3 \pm 0.4
315	0.1 \pm 0.6	2.2 \pm 2.7	3.3 \pm 0.9
Average	1.0 \pm 1.8	0.0 \pm 1.8	-0.3 \pm 1.8

Table 2.4: Variation of Φ -FWHM for each axial beam of specimens A, C, and D.

	Φ -FWHM [{} $^{\circ}$]		
	A	C	D
0	9.39 \pm 0.20	8.16 \pm 0.56	7.48 \pm 0.14
45	10.03 \pm 0.22	8.31 \pm 0.13	7.39 \pm 0.12
90	10.25 \pm 0.21	8.50 \pm 0.84	7.72 \pm 0.13
135	9.34 \pm 0.26	8.12 \pm 0.58	7.63 \pm 0.11
180	10.21 \pm 0.83	7.81 \pm 0.17	7.26 \pm 0.24
225	9.41 \pm 0.64	8.36 \pm 0.16	7.66 \pm 0.37
270	10.18 \pm 0.67	8.76 \pm 0.60	8.26 \pm 0.09
315	9.08 \pm 0.13	8.49 \pm 0.89	8.19 \pm 0.16
Average	9.74 \pm 0.64	8.32 \pm 0.61	7.69 \pm 0.38

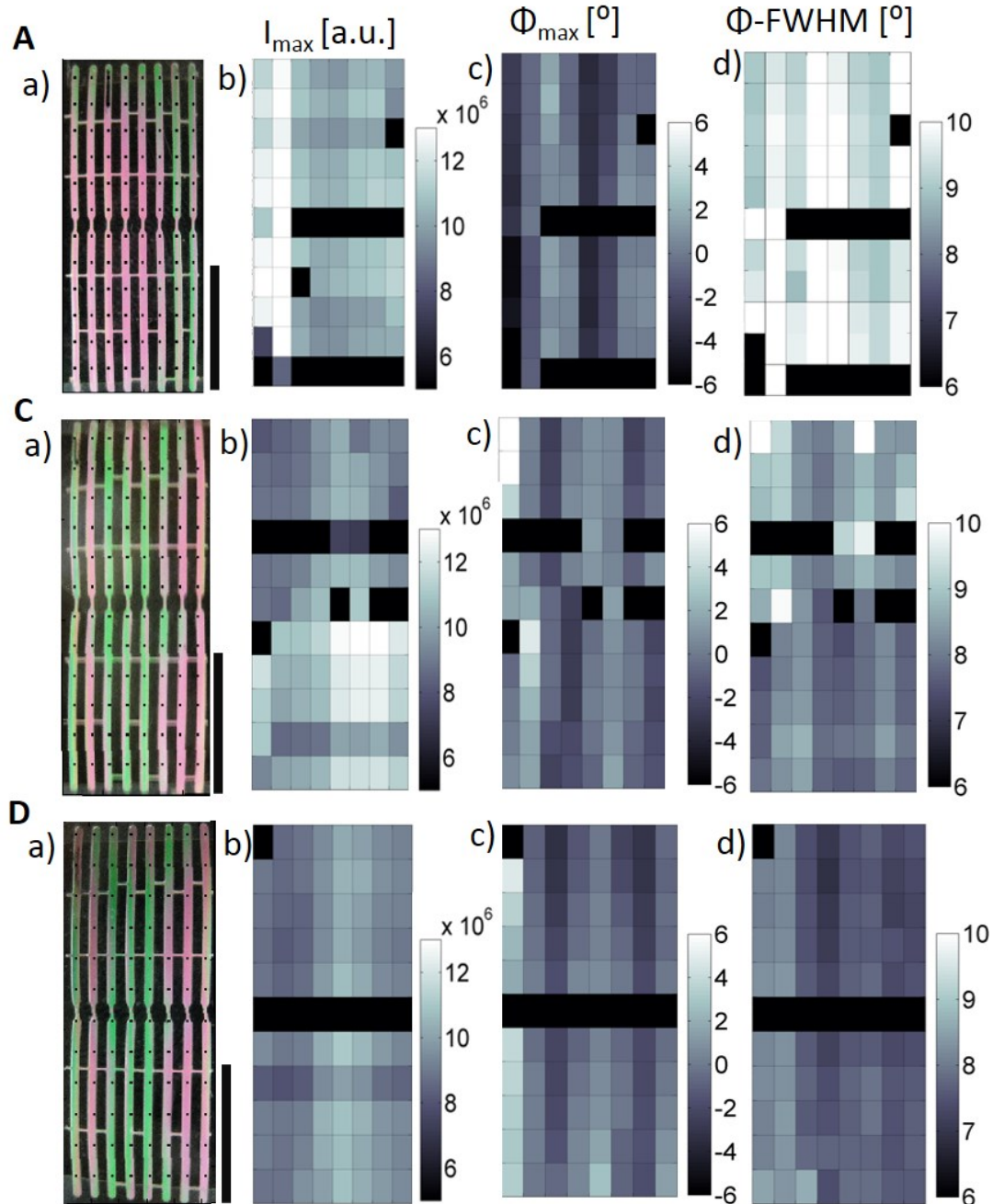


Figure 2.9 A, C, D): Coarse-grain views of specimens A, C, and D between crossed circular polarizers and corresponding maps showing the variation of quantities extracted from X-ray scattering data. a) Coarse-grain view of the specimen (see electronic document for color). The black dots on the image indicate the correspondence between the approximate physical location of the eleven points examined for each segment and each rectangle on the graph. The vertical scale bar is 1.0 cm. b) Variation in the maximum intensity of the dominant diffraction peak. c) Variation in Φ_{\max} [$^{\circ}$]. d) Variation in Φ -FWHM [$^{\circ}$]. For B-D in I-III the black rectangles on the graphs indicate the outliers.

2.2.2 Radial variations in as-cut thin sections

To probe variations in structure as a function of position through the thickness of the expanded PLLA tube, sections 10-15 μm thick were cut starting from the outer diameter toward the inner diameter from an as-cut subassembly (Methods). To keep track of the radial position of each section, they were each assigned a number according to the order they were obtained. Hence, a small number indicates a section closer to the OD and large number (e.g. 10) indicates a section closer to the ID. Sections near the OD tended to remain relatively flat (Fig. 2.10 section 2 and Fig 2.11 sections 2 and 3). Sections taken closer to the ID were observed to curl as soon as they were cut (Fig. 2.10 sections 7, 9, and 12), indicating substantial frozen-in stresses generated by the tubing expansion process. Polarized light examination of the sections showed that the sections that exhibited curling generally had greater retardance, which increased with proximity to the ID (progressing from 7 to 9 to 12 in Fig. 2.10 and from 5 to 7 to 8 in Fig 2.11).



Figure 2.10: Polarized light micrographs of 10-13 μm thick sections acquired in a Zeiss Universal microscope through crossed linear polarizers equipped with a Canon EOS DS30 camera. The thin sections were cut from YW crests (Fig. 2.13, Methods) in the radial direction. The smallest number corresponds to the section closest to the outer diameter of the scaffold subassembly. The onset of curling is about 70 μm and the onset of higher retardance is about 90 μm from the outer surface of the as-cut subassembly. Scale bar is 100 μm .

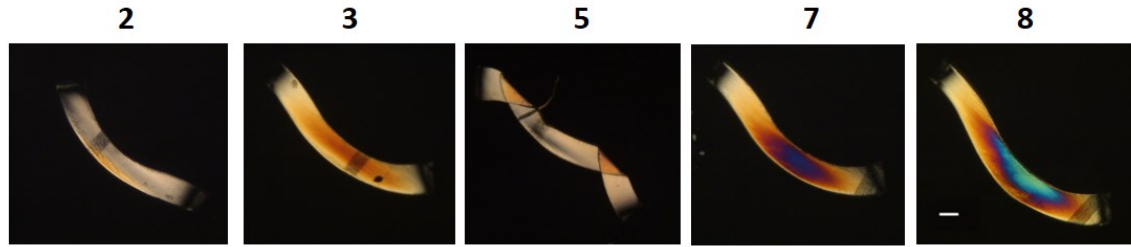


Figure 2.11: Polarized light micrographs of 10-13 μm thick sections acquired in a Zeiss Universal microscope through crossed linear polarizers equipped with a Canon EOS DS30 camera. The thin sections were cut from U crests (Fig. 2.13, Methods) in the radial direction. The smallest number corresponds to the section closest to the outer diameter of the scaffold subassembly. Curling is only observed for section 5; the retardance increases at about 70 μm from the outer surface of the as-cut subassembly. Scale bar is 100 μm .

2.3 Discussion

2.3.1 Axial and Azimuthal variations

The coarse-grained views of the specimens (Fig. 2.4) show that the Michel-Levy colors are almost constant along any individual beam, which indicates that axial variations are very small. Moving from one beam to the next (azimuthal steps of 45° going around the PLLA tube, Fig. 2.2) the Michel-Levy color only varies in the range between a green and an adjacent pink in the same order. Detailed analysis of the specimens using waveplates (Fig. 2.14) indicates that the order of the retardance is beyond the fourth order, such that the change from pink (~2360 nm) to green (~2500 nm) is approximately a 6% change in retardance as a function of azimuthal position. In the axial direction, each individual sample covers a distance of approximately 3 cm (Fig. 2.4) and the set of four specimens spans more than 12 cm (Fig. 2.5). Even across the greater distance of A-D the retardance only ranges from fourth order yellow (~2260 nm) to fourth order green (~2500 nm)—less than 10% variation over a length scale of more than 12 cm (Fig. 2.7). Thus, small variations are present in the azimuthal direction; axial variations are even milder.

A more quantitative interpretation of the birefringence of a semicrystalline material is difficult because it depends on multiple contributions: the degree of crystallinity (volume fraction X_c), the orientation distribution of the crystallites, and the level of frozen-in stresses that leads to birefringence in the amorphous material. Throughout the thickness of the present expanded tube of PLLA, the principal axes are along the azimuthal direction and the axial direction, so the total birefringence can be expressed additively. A primitive two-component equation suffices to show the challenge of interpreting the overall birefringence:

$$\Delta n = f_c \Delta n_c^* X_c + f_{oa} \Delta n_{oa} X_{oa} \quad (2.1)$$

where f_c and f_{oa} are the orientation factors of the crystallites and the oriented amorphous, Δn_c^* is the intrinsic birefringence of the crystallites, Δn_{oa} is the birefringence of the oriented amorphous, and $X_{oa} = 1 - X_c$ are the volume fractions of each component. The literature value of the intrinsic birefringence of PLLA crystals is not precisely known: Furuhashi et al. further determined the intrinsic birefringence for a purely α morph crystalline phase to be 0.031,²⁷ slightly higher than the highest value observed by Kobayashi²⁸ and Okhoshi²⁹ for oriented fibers. The birefringence of oriented amorphous PLLA depends on the magnitude of frozen-in stresses; as a representative value, Furuhashi et al. report a birefringence of 0.015.²⁷

The present PLLA specimens are 150 μm thick and exhibit retardance of 2300 to 2500 nm, corresponding to a birefringence of 0.014 - 0.016. Given the literature values for crystalline and oriented amorphous PLLA, this retardance could be explained by a fully amorphous materials with high frozen-in stress, or by a material that is roughly 50%

crystalline with highly oriented crystallites and 50% unoriented amorphous—or anything in between. This illustrates that polarized light microscopy alone cannot be used to evaluate volume fractions and orientation factors. For that level of detail, we turn to wide-angle X-ray scattering.

The variation in the maximum intensity of the dominant diffraction peak is typically about 4% for the measurements on a particular beam (specified by θ , Figs. 2-3), as indicated by the standard deviations (Table 2.1). Specimen A shows systematically stronger diffracted intensity, but only 0.8% greater than C and approximately 1.5% greater than D. In the azimuthal direction, the variations are readily observable, varying from 10% variation in specimen C to 20% variation in specimens A and D (see variations in I_{\max} values as θ increases from 0° to 315° for each specimen in Table 2.1). These are consistent with inferences made using polarized light microscopy. The above uniformity is also seen in the degree of order of the crystallites (Table 2.2), the dominant orientation directions (Table 2.3), the distribution of orientation (Table 2.4), and the crystallinity index (Table 2.5).

2.3.2 Radial variations

The polarized light micrographs of thin sections progressing from OD to ID (Figs. 2.10-11, left to right) show that the outermost 40-50 microns of the expanded tube have low anisotropy (first order silver Michel-Levy color, retardance ca. 280nm) and low frozen-in stresses (they hardly curl up). Progressing toward the ID, there is evidence of a more strongly oriented region in the innermost 50-70 microns (first order gold to first order red, retardance 420 to 560nm), which has significant frozen-in stresses (tight curl). It is striking that sections that are less than 50 microns apart in the radial direction show greater

differences in retardance than are seen over 12cm in the axial direction. A semi-quantitative comparison of the magnitude of the gradients could be based on the change in retardance divided by the distance over which the change occurs: axially, 10% change over 12 cm; azimuthally, 6% change over 1 cm; and radially, 100% change over 50 μm . Thus, relative to the axial structure variations, the gradients in the azimuthal direction are 10X greater—and those in the radial direction are 10,000X greater.

2.4 Conclusions

Bioresorbable scaffold performance depends on the uniformity of the expanded tube, which is crucial for consistent deformation during subsequent crimping and deployment.³ Processing of PLLA is known to be very difficult because even small fluctuations in water content, processing temperature and stereoregularity have a dramatic effect on the final morphology and material properties⁸. Here, we have used complementary materials characterization methods to interrogate structural variations in the axial, azimuthal, and radial directions. Polarized light microscopy and extensive sampling with synchrotron X-ray scattering have shown that the tube has remarkable axial uniformity and mild azimuthal variations. In contrast, radial gradients are substantial. The strongly oriented structure that is present near the ID of the expanded PLLA tube may provide much of the strength that holds the lumen open in the early months after implantation.³⁰ This materials characterization approach can be extended to examine the time course of hydrolytic degradation *in vitro* or bioresorption *in vivo*. For example, future work may examine the relationship between radial gradients in structure and the spatio-temporal profile of bioresorption after implantation.

2.5 Methods

2.5.1 Materials

Axial beam specimens

Four specimens were laser cut from the same PLLA expanded tube (Fig.2.2). Each specimen was laser cut to create eight equally spaced, 25.0 mm x 0.6 mm axial beams with azimuthal separation 45°. The beams are held together by thin “connectors.” A black mark indicates the 0° azimuthal position. The beam specimens were provided by Abbott Vascular.

Thin sections of as-cut subassemblies

Individual subassembly rings were embedded in TissueTek (Sakure), glued into screws, and then transferred to the microtome to equilibrate at -25 °C for 20 minutes. Thin sections 10-15 μ m thick were microtomed using a glass knife in the radial direction from an as-cut subassembly using a Powertome XL (RMC Products). The thin sections were provided by Abbott Vascular.



Figure 2.12 Image of an as-cut sub-assembly with boxes indicating the W, Y, and U struts.

2.5.2 Polarized light examination

Optically anisotropic materials have a refractive index that varies with the direction of light passing through them.³¹ When a light ray passes through an anisotropic material it

is refracted into two rays: one that travels with the same velocity through the material and one that depends on the propagation direction within the material. These rays are mutually perpendicular and they are referred to as ordinary and extraordinary, respectively.³²

The difference in refractive indices, Δn , between the extraordinary and ordinary rays is called birefringence. In polymers, birefringence may be caused by different crystal orientations and/or frozen-in stresses.³¹ When multiple rays of light pass through a birefringent material of thickness t , one of the rays will be retarded with respect to a faster ray; this velocity difference is referred to as the retardance (Eq. 2.2) and gives rise to the colors observed when the sample is placed between crossed linear polarizers.³² The retardance colors are classified into orders according to the Michel-Levy chart³¹, and can be used to identify the value of birefringence of a specimen of known thickness.

$$\text{Retardance} = t(\text{nm}) \times \Delta n \quad (2.2)$$

Coarse grained-views

Coarse-grained views of each specimen were acquired by placing the specimens between two circularly polarized sheets and taking photographs with a Canon Elf 10.0 MP camera.

Micrographs

Polarized light micrographs were acquired in a Zeiss Universal microscope at 4X magnification through crossed linear polarizers equipped with a Canon EOS DS30 camera.

Assignment of Michel Levy colors

To determine the order of Michel Levy colors, a connector from specimen D was imaged using different wave plate compensators (Fig. 2.14). The color transitions after adding [-1, -1/4, 0, +1/4 and + 1] wavelengths (λ) were observed and compared to the Michel-Levy color chart. In all cases, the yellow color on the bottom half of the connector acts as the

point of symmetry between the same order of red. Using the $+\lambda$ and $-\lambda$ red bands as reference, the sample's middle red band was determined to be a 3° red. Moving toward the upper portion of the connector, the colors transition to a higher order (higher retardance). In the case of $-\lambda$, based on the aforementioned symmetry, the pink band immediately above the 2° red is the 3° red. In the case of $+\lambda$, the absence of a distinct yellow band above the 4° red indicates that the upper pink colored band is the 5° red. Given that the progression of colors toward the upper half is the same, the next band moving up is the 4° red. Comparison with the $-\lambda$ and $+\lambda$ case shows that the green and light peach/pink colors observed in the above the 4° red must then be in the 5° order and they correspond to a retardance of approximately 2500 nm.

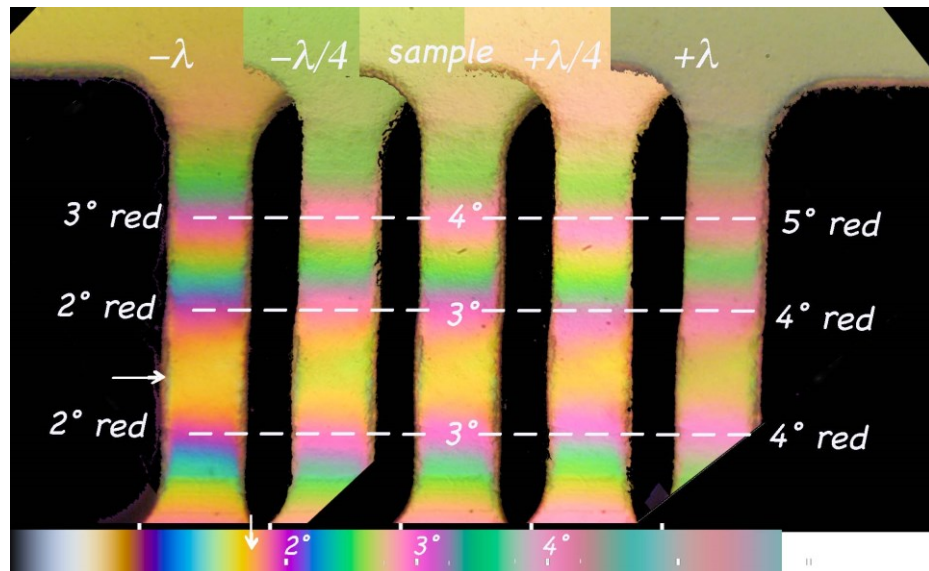


Figure 2.13 Photoshop composite image of polarized light micrographs of a connector from specimen D with different compensators; the centermost image is the sample. Sequence from bottom left to top right: The same connector with $[-1, -1/4, 0, +1/4, \text{ and } +1]$ wavelengths added using full- and quarter-waveplate compensators. Notice that subtracting a full wave brings the interference colors down to the second order (the minimum retardance point is indicated by the arrow, assigned to second order orange; the retardance increases moving away from the arrow, both up and down, indicated by the sequence of colors progressing orange, fuchsia, blue, turquoise,

green, yellow, peach). By assigning the colors obtained with a full wave subtracted, the retardance of the sample (centermost of the five images) is obtained. Moving from the point of least retardance in the connector to the beam at the top of the image, the retardance increases monotonically, allowing us to assign the order of the retardance in the beam (given in Figures 2.4 and 2.6). The thin black border above the Michel-Levy colors at the bottom of the figure has white marks at 565, 1130, 1685, 2260, and 2825nm. Using the Michel Levy Chart, the green color of the beam is found to correspond to an OPD of approximately 2500 nm.

2.5.3 X-ray scattering

X-ray scattering experiments were performed at beamlines X27C and X9 at the National Synchrotron Light Source at Brookhaven National Lab (NSLS).

NSLS X27C: Wide-angle X-ray scattering (WAXS) patterns were collected using a MarCCD detector at a distance of 134.8 mm from the samples. The source wavelength was 1.371 Å and the beam spot size was 380 µm. The diffraction patterns were calibrated for centering and detector distance using an alumina (Al_2O_3) standard. Each specimen was placed between three or four layers of X-ray transparent Kapton tape. Two WAXS patterns were acquired at different axial locations for each set, with two patterns per beam width. Radial and azimuthal integrations were performed using the software Polar® at the beamline's work station. Further data processing was done using Matlab® algorithms developed in-house.

NSLS X9: Wide- and small-angle scattering patterns were collected simultaneously for specimens A, C, and D, with a source wavelength of 0.92 Å and beam spot size of 20 µm. Eleven scattering patterns were acquired at approximately the same axial locations 2.5 mm apart. There was no data acquisition for specimen D due to time limitations. A custom Photonics detector²⁶ placed at 45° with respect to the plane of the sample captured a quadrant of the wide-angle scattering pattern (Fig. 2.15). Small-angle X-ray scattering (SAXS) patterns were collected using a Mar CCD detector at a sample-to-detector distance

of 185 mm. Both WAXS and SAXS diffraction patterns were calibrated for centering and detector distance using silver behenate ($\text{AgC}_{22}\text{H}_{43}\text{O}_2$). Calculation of radial and azimuthal intensity profiles and further data processing was done using Matlab® algorithms developed in-house.

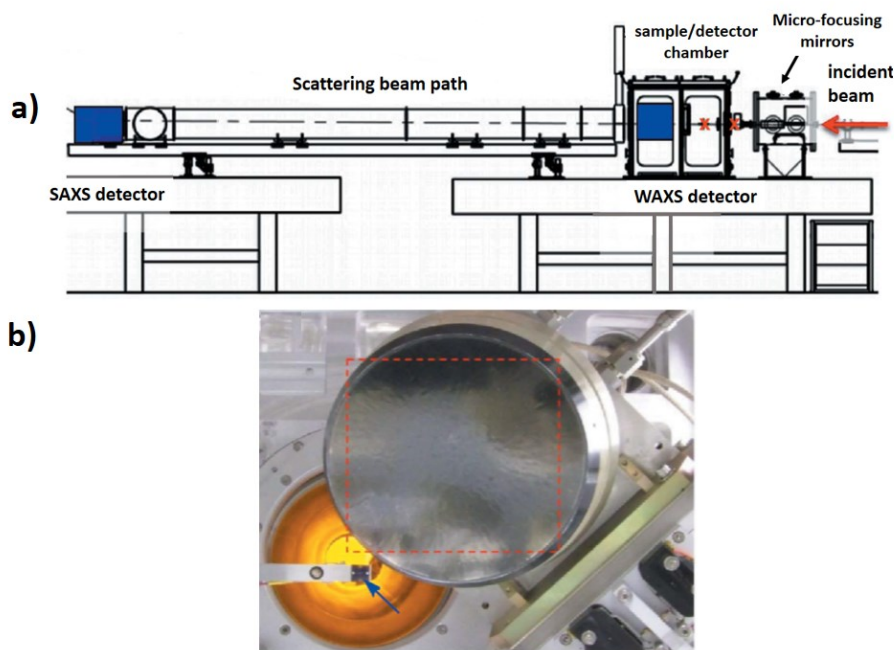


Figure 2.14 The setup of beamline NSLS X9. a) Diagram of the optical train and the detector positions. b) The special Photonics detector is placed to the side of the SAXS detector. Figure adapted from Lin, 2013.

2.5.4 Data analysis

To compare X-ray scattering data from different beamlines, image analysis code was developed using MATLAB®. This code was used to obtain radial and azimuthal intensity profiles, and to extract quantitative values for maximum intensity, crystal orientation, and crystal spacing. All data was pre-processed for background subtraction and incident intensity variation. Some scattering patterns in each set had a very low intensity signal compared to the mean. We attribute this to partial placement of the beam on the

sample due to motor drift during the automated data acquisition. These outliers were removed by excluding the 2D patterns whose maximum intensity was less than 75% of the entire data set's mean intensity.

References

- (1) Onuma, Y.; Serruys, P. W. Bioresorbable Scaffold: The Advent of a New Era in Percutaneous Coronary and Peripheral Revascularization? *Circulation* **2011**, *123*, 779–797.
- (2) Oberhauser, J. P.; Hossainy, S.; Rapoza, R. J. Design Principles and Performance of Bioresorbable Polymeric Vascular Scaffolds BVS ABSORB Cohort B Device. *EuroIntervention* **5**, 15–22.
- (3) City, F. Stent Tubing : Understanding the Desired Attributes. **2003**.
- (4) Sarasua, J. R.; Arraiza, a. L.; Balerdi, P.; Maiza, I. Crystallinity and Mechanical Properties of Optically Pure Polylactides and Their Blends. *Polym. Eng. Sci.* **2005**, *45*, 745–753.
- (5) Takagi, J.; Nemoto, T.; Takahashi, T.; Taniguchi, T.; Koyama, K. Improvement of Mechanical Properties for Poly (L-Lactic Acid) Film through Drawing Process Optimization. *Fiber* **2004**, *60*, 230–234.
- (6) Oca, H. M. D. E.; Ward, I. M. Structure and Mechanical Properties of Poly (L -Lactic Acid) Crystals and Fibers. *J. Polym. Sci. Part B Polym. Phys.* **2007**, *45*, 892–902.
- (7) Cocca, M.; Lorenzo, M. L. Di; Malinconico, M.; Frezza, V. Influence of Crystal Polymorphism on Mechanical and Barrier Properties of Poly(l-Lactic Acid). *Eur. Polym. J.* **2011**, *47*, 1073–1080.
- (8) Lim, L.-T.; Auras, R.; Rubino, M. Processing Technologies for Poly(lactic Acid). *Prog. Polym. Sci.* **2008**, *33*, 820–852.
- (9) Tsuji, H.; Ogiwara, M.; Saha, S. K.; Sakaki, T. Enzymatic, Alkaline, and Autocatalytic Degradation of poly(L-Lactic Acid): Effects of Biaxial Orientation. *Biomacromolecules* **2006**, *7*, 380–387.
- (10) Agrawal, C. M.; Haas, K. F.; Leopold, D. a; Clark, H. G. Evaluation of poly(L-Lactic Acid) as a Material for Intravascular Polymeric Stents. *Biomaterials* **1992**, *13*, 176–182.
- (11) Menary, G. H.; Tan, C. W.; Harkin-Jones, E. M. A.; Armstrong, C. G.; Martin, P. J. Biaxial Deformatio and Experimental Study of PET at Conditions Applicable to Stretch Blow Molding. *Polym. Eng. Sci.* **2012**, *5*, 671–689.

(12) Mano, J. F.; Gómez Ribelles, J. L.; Alves, N. M.; Salmerón Sanchez, M. Glass Transition Dynamics and Structural Relaxation of PLLA Studied by DSC: Influence of Crystallinity. *Polymer* **2005**, *46*, 8258–8265.

(13) Wang, Y.; Funari, S. S.; Mano, J. F. Influence of Semicrystalline Morphology on the Glass Transition of Poly(L-Lactic Acid). *Macromol. Chem. Phys.* **2006**, *207*, 1262–1271.

(14) Pham, X.-T.; Thibault, F.; Lim, L.-T. Modeling and Simulation of Stretch Blow Molding of Polyethylene Terephthalate. *Polym. Eng. Sci.* **2004**, *44*, 1460–1472.

(15) Belcher, S. Blow Molding. In *Encyclopedia of Polymer Science and Technology Vol. 1*; 2002; Vol. 1.

(16) Henton, D. E.; Gruber, P.; Lunt, J.; Randall, J. Natural Fibers, Biopolymers, and Biocomposites 16. Polylactic Acid Technology. In *Natural Fibers, Biopolymers, and Biocomposites*; 2005; pp. 527–578.

(17) Wasanasuk, K.; Tashiro, K. Crystal Structure and Disorder in Poly(l-Lactic Acid) Δ Form (α' Form) and the Phase Transition Mechanism to the Ordered A Form. *Polymer* **2011**, *52*, 6097–6109.

(18) Stoclet, G.; Seguela, R.; Lefebvre, J. M.; Elkoun, S.; Vanmansart, C. Strain-Induced Molecular Ordering in Polylactide upon Uniaxial Stretching. *Macromolecules* **2010**, *43*, 1488–1498.

(19) Stoclet, G.; Séguéla, R.; Lefebvre, J. M.; Li, S.; Vert, M. Thermal and Strain-Induced Chain Ordering in Lactic Acid Stereocopolymers: Influence of the Composition in Stereomers. *Macromolecules* **2011**, *44*, 4961–4969.

(20) Wasanasuk, K.; Tashiro, K.; Hanesaka, M.; Ohhara, T.; Kurihara, K.; Kuroki, R.; Tamada, T.; Ozeki, T.; Kanamoto, T. Crystal Structure Analysis of Poly (L -Lactic Acid) Alpha Form On the Basis of the 2-Dimensional Wide-Angle Synchrotron X-Ray and Neutron Diffraction Measurements. *Macromolecules* **2011**, *44*, 6441–6452.

(21) Kawai, T.; Rahman, N.; Matsuba, G.; Nishida, K.; Kanaya, T.; Nakano, M.; Okamoto, H.; Kawada, J.; Usuki, A.; Honma, N.; et al. Crystallization and Melting Behavior of Poly (L-Lactic Acid). *Macromolecules* **2007**, *40*, 9463–9469.

(22) Alexander, L. E. *X-Ray Diffraction Methods in Polymer Science*; Wiley Interscience: New York, 1969.

(23) Stoclet, G.; Seguela, R.; Vanmansart, C.; Rochas, C.; Lefebvre, J.-M. WAXS Study of the Structural Reorganization of Semi-Crystalline Polylactide under Tensile Drawing. *Polymer* **2012**, *53*, 519–528.

(24) Ania, F.; Calleja, F. J. B.; Bayer, R. K. Structure Formation and Properties of Biaxially Oriented Polyethylene Films by Compression of Injected Mouldings. *Polymer* **1992**, *33*, 233–238.

- (25) Gerrits, N. J. A.; Young, R. J.; Lemstra, P. J. Tensile Properties of Biaxially Drawn Polyethylene. *Polymer* **1990**, *31*, 231–236.
- (26) Yang, L. Using an in-Vacuum CCD Detector for Simultaneous Small- and Wide-Angle Scattering at Beamline X9. *J. Synchrotron Radiat.* **2013**, *20*, 211–218.
- (27) Furuhashi, Y.; Kimura, Y.; Yamane, H. Higher Order Structural Analysis of Stereocomplex-Type Poly (Lactic Acid) Melt-Spun Fibers. **2006**, *4*–6.
- (28) Kobayashi, J.; Asahi, T.; Ichiki, M.; Oikawa, a.; Suzuki, H.; Watanabe, T.; Fukada, E.; Shikinami, Y. Structural and Optical Properties of Poly Lactic Acids. *J. Appl. Phys.* **1995**, *77*, 2957.
- (29) Ohkoshi, Y.; Shirai, H.; Gotoh, Y.; Nagura, M. Intrinsic Birefringence of Poly (L-Lactic Acid). *Sen-I Gakkaishi* **1999**, *55*, 21–27.
- (30) Onuma, Y.; Ormiston, J.; Serruys, P. W. Bioresorbable Scaffold Technologies. *Circ. J.* **2011**, *75*, 509–520.
- (31) Robinson, P. C.; Bradbury, S. *Qualitative Polarized Light Microscopy*; Oxford University Press, Royal Microscopical Society, 1992; pp. 8–14.
- (32) Murphy, D. B.; Spring, K. R.; Fellers, T. J.; Davidson, M. W. Introduction to Optical Birefringence <http://www.microscopyu.com/print/articles/polarized/birefringence-print.html> (accessed Mar 10, 2014).

CHAPTER 3

Effect of Crimping on Scaffold Morphology

3.1 Introduction

Prior to implantation in the artery, the as-cut scaffold subassembly must be crimped (Fig. 3.1) and adhered onto a flexible catheter that can be guided through the vascular system. During crimping, the outer bends of the Y, W, and U crests (Fig. 3.1) of the as-cut subassembly are elongated and the inner bends are compressed until the scaffold is in full contact with the balloon and its outer diameter decreases 50-70%. Most stent effectiveness studies do not take into account the effect of crimping on deployment; in fact, some authors have stated that the crimping has a “minor influence on the overall expansion of the stent.¹” However, a few studies have studied the impact of crimping on commercial metal stents and found that the crest bends store residual stresses from the deformation during crimping.²⁻⁵ Nevertheless, to the best of our knowledge, no studies have addressed the microstructural changes of polymeric scaffolds, which are extremely important for predicting deployment behavior and mechanical stability post-implantation.

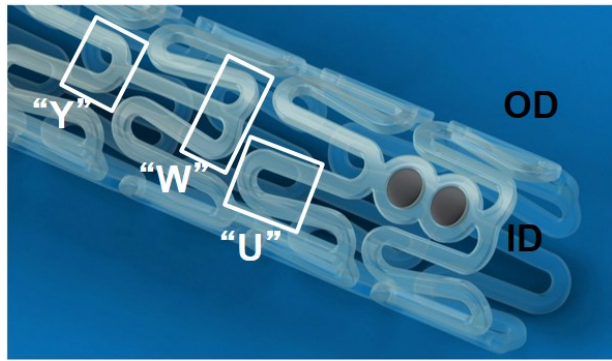


Figure 3.1 Digital rendering of a crimped scaffold subassembly (without the balloon for clarity). The outer and inner diameter of the subassembly are referred to as OD and ID, respectively. The Y, W, and U crests are defined.

Stents and scaffolds must be made from a ductile material that can withstand the compressive deformation during crimping and the subsequent expansion during deployment without losing radial strength. The deformation mechanisms of polymers are plastic deformation, crazing, and fracture. From a crystallographic point of view, this may happen through interlamellar separation, lamellar rotation, lamellar slip, and twinning.⁶⁻⁸ During yielding, plastic flow of the material takes place without change in volume.⁹ Crazing can be considered a precursor to cracks but unlike cracks, the two separated surfaces are spanned by many small fibrils with diameters in the range of 5-30 nm.¹⁰ There is always a competition between plastic deformation and crazing; the resulting behavior depends on the amount of crystallinity, crystal orientation,¹¹⁻¹³ number of entanglements¹⁴, and the deformation temperature (lower temperature increases both plastic deformation and crazing)⁹. When cracks form, they do so by breakdown of fibrils within a craze. In practice, crazing can be beneficial: because crazes store very high local stresses (they are load-bearing), crazing increases the fracture toughness of polymer glasses.^{8,10,15} This is

particularly important if the structure must bear tensile load⁹, as in the case of the scaffold upon deployment.

The deformation mechanisms of poly(L-lactic acid) (PLLA) have been studied in the context of uniaxial or biaxial extension, usually with grades containing at least 2-4% D-isomer and at temperatures typically above the glass transition temperature ($T_g \approx 60^0\text{C}$). Several authors have shown that drawing of amorphous PLLA near T_g ($T = 70\text{-}90^0\text{C}$) results in very highly oriented crystallites of the α' morph along the draw direction.¹⁶⁻¹⁹ Cakmak and coworkers have shown that sequential biaxial stretching of PLLA films results in breakup and rearrangement of the crystallites in the second stretch direction.²⁰⁻²² Nanomechanical tensile testing has shown that PLLA yields by forming highly localized crazes which continue to increase in size and number until failure.^{23,24} Nonetheless, despite the ever-increasing use of PLLA in load-bearing medical applications, there is a surprising dearth of literature on the effects of compression (as in the case of crimping) on the microstructure of PLLA.

Here, we have used a combination of scanning electron and polarized light microscopy and synchrotron X-ray microdiffraction to examine variations in PLLA morphology after crimping. Scanning electron microscopy provides an overview of the bulk morphology of a crimped subassembly as well as micron-scale features. Polarized light microscopy provides a large-scale overall view of variations in polymer chain orientation, and can distinguish features such as shear bands and crazes. The microscopy results guide our X-ray microdiffraction measurements to map the crystalline microstructure.

3.2 Results

3.2.1 Scanning electron microscopy

Scanning electron micrographs (SEM) of crimped scaffold subassemblies show that extreme solid-state deformation occurred in localized regions near the bends of all U, Y, and W crests (Fig. 3.2a). Near the outer perimeter of the bend, the scaffold is thinner than the original thickness of 150 μm and there is a pronounced bulge at the inner bend (Fig. 3.2b).

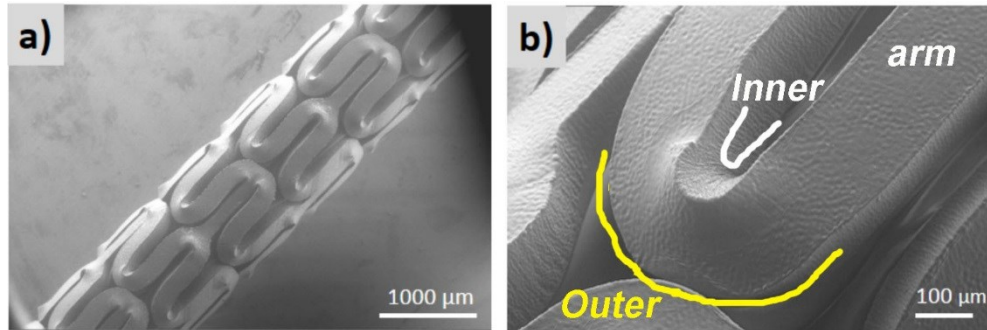


Figure 3.2 a) Scanning Electron Micrograph (SEM) of a crimped subassembly. b) Higher magnification image of a U crest shows the bulging out of the inner bend. Images provided by Abbott Vascular.

High magnification SEM images show the formation of a micro-crack at the inner bend (Fig. 3.3a). The tip of the micro-crack is consistent with a craze front advancing in the z-direction of the bend (Fig. 3.3b). The fibrils (Fig. 3.3c) observed at examination with high magnification of the microcrack's tip further support the interpretation of crazing.

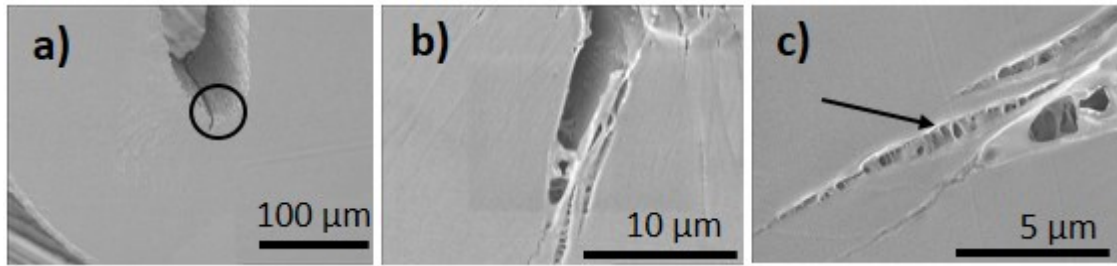


Figure 3.3 SEM images of a micro-fissure on a single U crest (*not* a thin section) at different magnifications. a) At low magnification, a micro-crack is observed at the inner U bend b) at higher magnification, the tip of the micro-crack is consistent with crazing c) Large magnification image of the same area shows the formation of microfibrils. SEM micrographs provided by Abbott Vascular. [FLIP]

3.2.2 Polarized light microscopy

In Chapter 2, we showed that the radial variations in the microstructure of as-cut subassemblies is significant. Hence, we chose to study the microstructure of the crimped subassemblies using thin sections in the radial direction (Methods). Polarized light micrographs of sections cut from W and U bends (defined in Fig. 3.1) show shear bands (Fig. 3.4) in the regions that correspond to the transition zone between the bulge at the inner bend and the plateau of relatively undeformed material on either side of the bulge (Fig. 3.2).

The sequence of colors in the polarized optical micrographs (POM) reveals whether the retardance is increasing or decreasing. For example, moving from the fuchsia color in the left arm of the crimped W (Figure 3.4a) toward the inner bend in the white rectangle, the progression of colors indicates a *decrease* in retardance from approximately 1500 nm (fuchsia) to 1400 nm (yellow) to 1300 nm (green) to 1200 nm (blue) to 1100 nm (purple) to 1000 nm (fuchsia) to 900 nm (yellow) to 700 nm (sky blue) to 600 nm (navy blue) to 500 nm (burgundy) to 400 nm (gold). The decrease of retardance from the arm to the inner bend is also seen in the U crest (Fig. 3.4b) from approximately 1500 nm (fuchsia) to 1400

nm (yellow) to 1300 nm (green) to 1200 nm (blue) to 1100 nm (purple) to 1000 nm (fuchsia) to 900 nm (yellow). If instead one follows a path from the fuchsia region in the left side of the crimped U to its outer bend, the sequence reverses (Figure 3.4b): after passing through the orange region the colors progress to fuchsia, lavender, jade, cream, pink, and aqua near the outer bend. This sequence of colors indicates an increase in retardance from 1450 nm (orange) to 1500 nm (fuchsia) to 1600 nm (lavender) to 1800 nm (jade) to 1950 nm (cream) to 2100 nm (pink) to 2300 nm (aqua). Further analysis of the Michel-Levy colors after rotating the sample between crossed polarizers (Methods) can give an approximation of the chain orientation at the outer bend (Fig. 3.5).

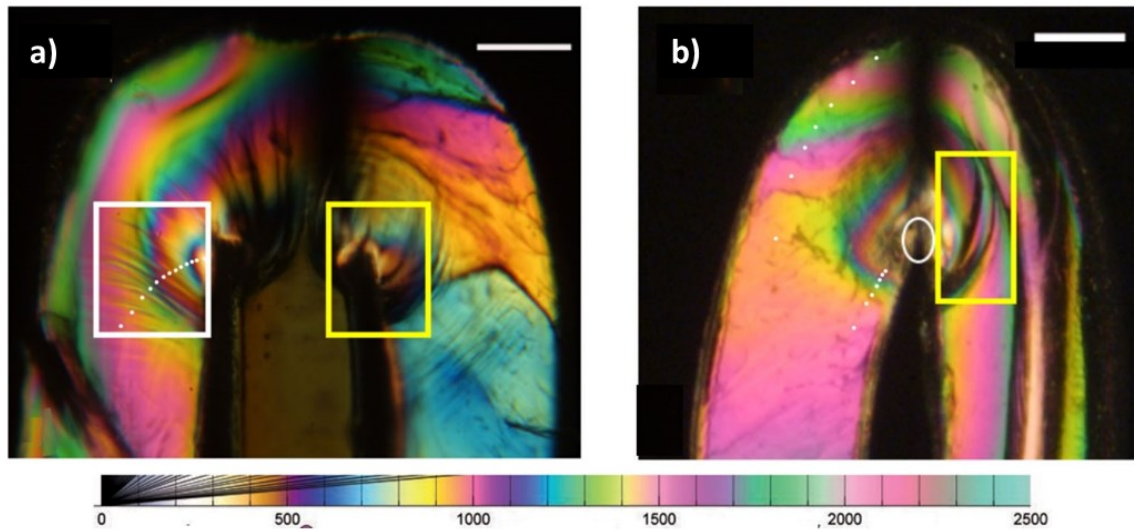


Figure 3.4 Polarized light micrographs of sections cut from a) a W crest about 40 μm away from the OD and b) a U crest about 45 μm away from OD. Rotation under polarized light (see Methods) shows that the features in the white rectangle in part are shear bands, the features in the yellow boxes are crazes, and the feature in the white oval is a micro-crack. See text for explanation of the sequence of Michel-Levy colors along each dotted paths. Both polarized light micrographs were acquired in a Zeiss Universal microscope through crossed linear polarizers equipped with a Canon EOS DS30 camera. Scale bars are 100 μm .

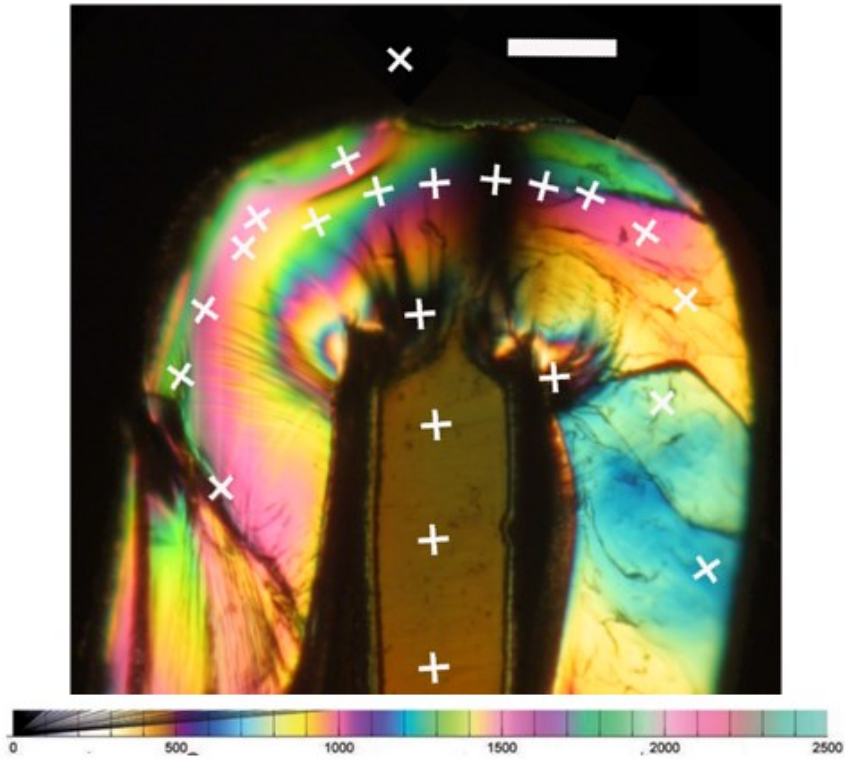


Figure 3.5 Orientation analysis of the W section shown in Fig. 4. The horizontal line of the crosses along the outer bend indicates the chain orientation. The single x mark indicates the direction of the crossed linear polarizers for this particular micrograph. Scale bars are 100 μm .

The common features observed under polarized light are consistent with the bulge formation at the inner bend of all crests (Fig. 3.2a) and indicate that examination of thin sections from one type of crest can teach us about the microstructure of the other two. Mechanical test studies of deployment to failure have shown that failure occurs mainly at U crests. Therefore, we chose thin sections from U crests for X-ray microdiffraction experiments.

3.2.3 Wide-angle X-ray microdiffraction

The microstructure around the inner bend of the thin section shown in Figure 3.4b (and Fig. 3.12, Methods) was examined by X-ray microdiffraction. To characterize the spatial microstructure evolution we considered the following quantities: I_{\max} of $I(\Phi)$, Φ_{\max} ,

and Φ -FWHM (Fig. 2.3c of Chapter 2 shows the definition of the angle Φ for the (110)/(200) peak on the 2D scattering pattern—not to be confused with the scattering angle 2θ). Because we are evaluating the structure within a single specimen, the maximum intensity of the (110)/(200) peak can be used to evaluate the density of crystals aligned in the θ -direction²⁵, Φ_{\max} , to evaluate the crystal orientation, and Φ -FWHM to evaluate the strength of orientation.^{25,26}

Selected X-ray microdiffraction patterns acquired at beamline2-ID-D of the Advanced Photon Source (APS) at Argonne National Lab show that the dominant crystal morph is α' (Fig. 3.6c). Depending on the position of each pattern (white crosses on Fig. 3.6a) away from the symmetry plane (green line, Fig. 3.6a) the crystal orientation axis shifts symmetrically in the θ -direction (any row of patterns, Fig. 3.6c). The quantitative analysis of all diffraction patterns (483 total, 10 μm apart) is shown in Figure 3.7. Diffraction patterns with bright reflections indicative of micro-fibrils are shown in Figure 3.8.

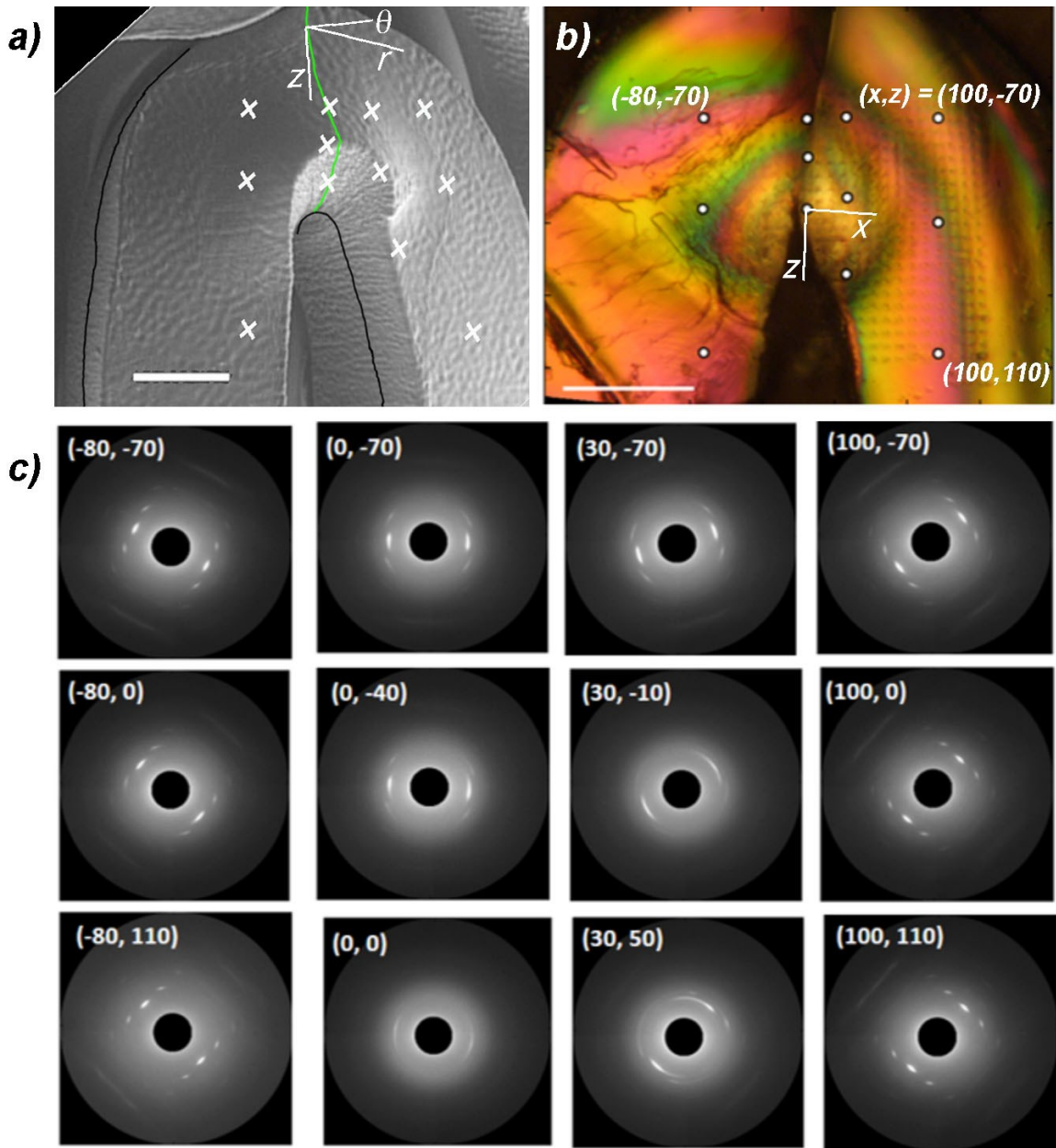


Figure 3.6 a) Schematic showing the approximate positions (white “x”) of the X-ray microdiffraction patterns on an SEM image of a crimped U (different from the one used to obtain the present section). The green line shows the approximate axis of symmetry and the black line shows the approximate depth of the present thin section. Scale bar is 100 μm . b) Polarized light micrograph of the region examined with microdiffraction (Michel-Levy colors are altered by the Kapton substrate used for the experiments). The (x,z)-axes show the origin from which positions are specified in microns. White dots on the micrograph show the location at which the diffraction patterns in c) were acquired. The location of each X-ray measurement was marked using mild beam damage. Scale bar is 100 μm . c) Selected microdiffraction patterns acquired at 2-ID-D with a 0.2 μm beam spot size.

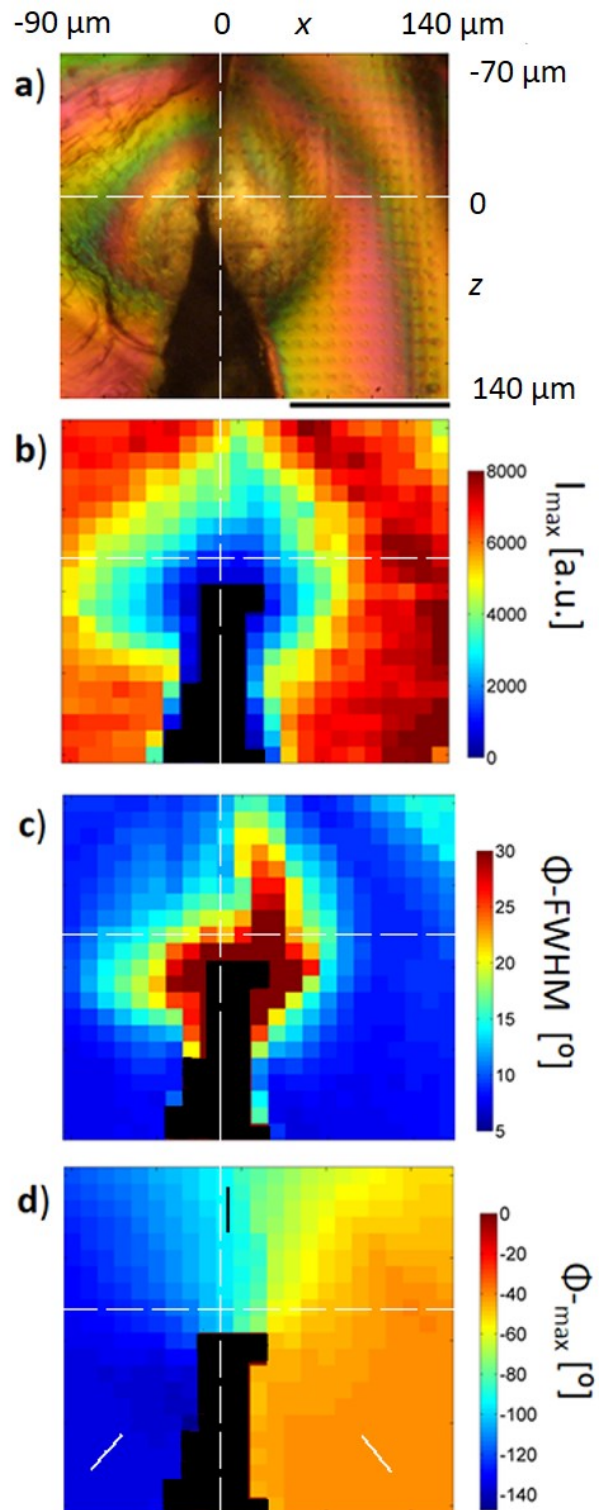


Figure 3.7 Quantitative analysis of the 483 x-ray patterns acquired at the inner bend of the present thin section. a) Polarized light micrograph of the region examined with X-ray microdiffraction (Michel-Levy colors are altered by the Kapton substrate used for the experiments). The boundaries of the data acquisition range are shown with respect to the (0, 0) position. The location of each X-

ray measurement was marked using mild beam damage. Scale bar is 100 μm . b) Spatial variation in the maximum intensity of the $I(\Phi)$ curve. Black color represents the empty space between the arms of the U. c) Spatial variation in Φ -FWHM. Black represents the empty space between the arms of the U. d) Spatial variation in Φ_{\max} . Black represents the empty space between the arms of the U. White lines indicate the orientation of the crest's arms.

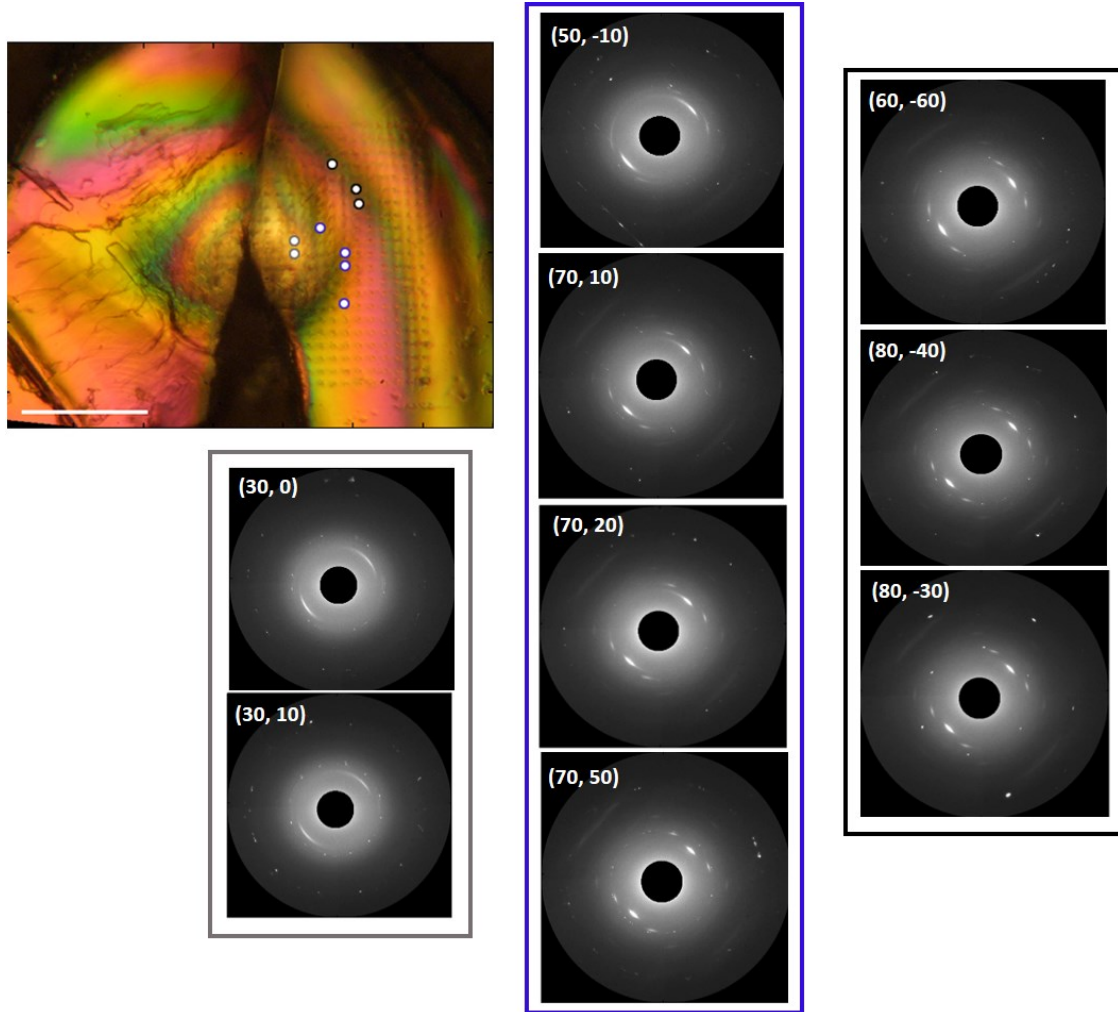


Figure 3.8 Selected microdiffraction patterns acquired at crazes with a 0.2 μm irradiated spot size. The polarized light micrograph shows the region examined with x-ray microdiffraction (Michel-Levy colors are altered by the Kapton substrate used for the experiments). White dots on the micrograph show the location at which the diffraction patterns were acquired. The location of each X-ray measurement was marked using mild beam damage. Scale bar is 100 μm .

3.3 Discussion

A thorough understanding of one specific section cut from a crimped “U” crest provides the foundation for understanding the three-dimensional field of polymer orientation and semicrystalline microstructure that is created during crimping. For this purpose, a microtomed section cut from a depth of approximately 45 μm from the outer diameter (OD) surface (Fig. 3.1) of a crimped U is particularly instructive (black line, Fig. 3.6a). The section is approximately 10 μm thick, representing about 1/15th of the total thickness of the scaffold. During crimping, the “outer bend” is placed under tension in the θ -direction and thins in the r -direction. As will be demonstrated in Chapter 4, this tension orients the chain axis approximately parallel to the outer bend (Fig. 3.9 b and c, curved black lines). In contrast to the relatively simple structure in the arms and the outer bend, dramatic variations in structure are observed near the “inner bend,” where material elements are compressed in the θ -direction and forced to bulge outward in the $+r$ - and $-r$ -directions (Fig. 3.9b). Therefore, X-ray microdiffraction was performed in a region that spans the area under the bulge and extends laterally (θ -direction) beyond it.

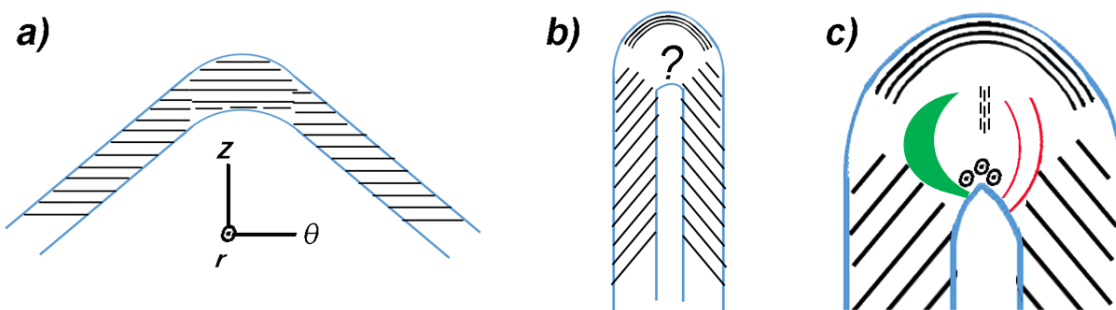


Figure 3.9 Schematic showing the polymer chain orientation evolution during crimping. a) In the as-cut U, the orientation is inherited from the tube expansion and polymer chains are oriented in the θ -direction in both arms and bend. The axes show the r -direction pointing outward. b) During crimping, the arms perform a rigid body rotation; the absence of deformation leaves the

semicrystalline microstructure unchanged, simply rotated 50° (clockwise) on the right and -50° (counter-clockwise) on the left. The outer and inner bend experience elongation and compression in the θ -direction, respectively. The elongation at the outer bend (black lines) is discussed in the next chapter. The chain orientation in the compressive region is more complex. c) The results of this study show that the chain axes are oriented along r (dots in circles indicate c -axis normal to the page). Between the θ -compression and θ -elongation regions, the chain axes are oriented along z . Emanating from the inner bend, there are crazes on the right side (red curved lines) and a plastic deformation zone (green crescent) on the left.

In the as-cut subassembly, the PLLA chains are oriented primarily in the θ -direction (Fig. 3.9a) and the arms of the U bend are at approximately + 50° and -50° (Fig. 3.11a, Methods). After crimping, the arms of the U bend are nearly parallel to the z -direction (Fig. 3.11b, Methods). Over most of their length, the arms rotate as a solid body (Fig. 3.9b). This explains the microdiffraction patterns acquired just outside the deformation field of the bulge, i.e. at positions (-80, -70), (-80, 110), and (100, 110) of Figure 3.5, which are very similar to those observed for the as-cut subassembly, simply rotated by $\pm 50^\circ$ (Fig. 3.6c and Fig. 3.7d). The lack of deformation in the arms also explains the uniformity of the (110)/(200) peak intensity and the breadth of the orientation distribution (Fig. 3.7 b and c, lower left and lower right), which agree with those of the as-cut subassembly (Chapter 2). On a larger length scale, the arms show uniform Michel-Levy color (third-order fuchsia, retardance ~ 1500 nm, Fig. 3.4b; note that the section was inadvertently crumpled on the right edge, causing the apparent variation in retardance on the far right). Thus, in the arms, the semicrystalline structure is simply that inherited from the expanded tube.

Rotation of the arms creates a high pressure zone, where most of the deformation occurs. The deformation zone is surprisingly small, e.g. the (110)/(200) intensity varies from <1000 nm near the origin to 6000 nm over a distance of less than 100 μm (Fig. 3.7b). At the point of strongest θ -compression, denoted as (0, 0), the inner bend forms a cusp

(sharp point where the two legs meet, Fig. 3.5b). Elevated pressure in the θ -compression zone drives material out in the $+r$ and $-r$ directions, creating the bulge seen in SEM (Fig. 3.6a). Inherently, this represents an elongational deformation in the r -direction at the inner bend. The elongation in $\pm r$ results in the rotation of the c -axis out of the (θ, z) -plane manifested by the gradual disappearance of the (110)/(200) and (203) peaks moving from position (0, -70) to (0,0) (Fig. 3.6c). Another consequence of the high pressure is movement of material toward the outer bend along the $-z$ -direction, which results in stretching along z at positions below the bulge (interior of the deformation zone, e.g. (0, -70) of Fig. 3.6c). Thus, understanding the deformation field in 3D is vital to understanding the microstructural changes of the PLLA in the crimping process.

The combination of arm rotation and high pressure results in shear in the (θ, z) -plane at the boundary between the solid body rotation zones and deformation zone. On the $+x$ -side of the deformation zone shear is manifested by the presence of crazes (Figs. 3.7 and 3.9) and on the $-x$ -side, shear is manifested by strong plastic deformation. The asymmetry in the mode of shear deformation explains a striking feature of the deformation zone: its asymmetry (Fig. 3.7 b and c). The asymmetry suggests that during crimping, the initial compression stress causes plastic deformation, but as the stress increases the material deforms by crazing (Fig. 3.9). In view of many other sections from several W, U, and Y crests that were examined, when Michel-Levy colors are observed, the retardances fields usually have this asymmetry. Thus, asymmetry appears to be the result of the competition between crazing and plastic deformation. Having both crazing and plastic deformation is a major component of toughness and resistance to fracture under stress.^{8,10}

Crazing is evidenced by patterns showing discrete bright reflections (Fig. 3.8), which reveal the presence of highly drawn fibrils. The physical location of the fibril patterns corresponds to regions that remain dark at all rotations under polarized light (Fig. 3.12, Methods). The multiplicity of the bright reflections indicates that multiple fibrils with different orientations are present in the 200 nm area probed by the microdiffraction beam (e.g. (30, 10), Fig. 3.8), which agrees with multiple, differently oriented nanofibers that connect opposite faces of the crazes seen in SEM images (Fig. 3.3c). While crazing is evident, the crazes appear to be thin and/or obliquely oriented relative to the microtomed sections: a beam spot that is only 200 nm across and passes through an optical path of 10 μm predominantly samples material outside the craze (diffraction patterns are dominated by the same diffraction pattern as the surrounding material, with weaker signals from the fibrils; we cannot comment on the length of the crazes in the (θ, z) -plane because the step size of the raster scan is 10 μm). Thus, even though the material crazes, it does so in a way that absorbs the imposed stress and resists fracture.⁷ The craze fibril patterns are not seen in the plastic deformation zone on the other side ($x < 0$) of the specimen, which again agrees with crazing at the regions of most intense shear to “protect” the other side⁷.

The characteristic “comet” shape of the (110)/(200) peak is associated with the crazing region (there are no “comet” diffraction patterns in the plastic deformation zone on the $x < 0$). Such patterns are rarely reported in the literature. Wilkes and coworkers^{13,27} observed them in specimens that were subjected to elongation in a direction 45° to the lamellar normal. The findings of Cohen, Argon, and coworkers^{28,29} in relation to transformation of lamellar structure provide a potential link between the formation of the patterns in the region of the bend in which the θ -compression causes elongation in the $\pm r$ -

direction and the shear in the (θ, z) -plane. In both studies, the lamellae were seen to rupture at strains associated with the onset of plastic deformation. The lamellar stack avoids rotation by localizing strain in bands, like fault lines (Fig. 3.10b). Thus, the comet “head” can be attributed to the bulk of the lamellae, which retain an orientation close to that of the surrounding material undergoing solid body rotation with little or no strain: the main peak accords with the rotation of the c-axis in the arms (Fig. 3.10d, blue arrow). In the bands of localized strain where the lamellae rupture, the c-axis tends to orient along a direction that connects the newly exposed edges of the lamellae with the direction that the material used to belong. Thus, while the displacement of the now separated lamellar stacks tracks the shear deformation, the c-axis of the material in the ruptures appears to rotate in the opposite direction to the vorticity (Fig. 3.10c). Therefore, the “tail” reflects a distribution of crystallites rotating opposite from the rotation direction of the arms (Fig. 3.10d, red boxes). The stronger intensity near the main peak tapering away as the angular deviation increases shows that the smaller the angular deviation, the greater the population of distorted crystals (the lower intensity of the tail can be attributed to the additional rotation of the crystal axis in the $\pm r$ -direction).

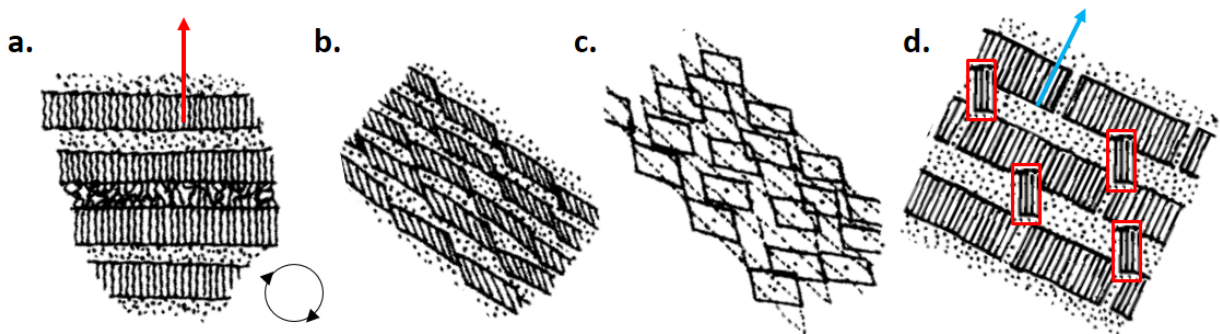


Figure 3.10 Schematic showing the mechanism of lamellar rupture and fragment rotation. a) The undeformed lamellae have the c-axis pointing up (red arrow). They are subjected to shear with the vorticity direction, as shown in the circle. b) The lamella resist rotation by localizing the strain in

bands that will eventually rupture. c) Once the rupture occurs, the ruptured material rotates opposite from the rotation direction, while the bulk of the lamellar stacks tracks the shear deformation. d) In the final configuration after the rotation the lamellar fragments retain the original orientation (framed in red for emphasis), which is angled with respect to the new c-axis (blue arrow). Scheme adapted from Galeski *et al.* (1992).²⁸

3.4 Conclusions

The deformation during the crimping process is a complex three-dimensional process that cannot be understood without considering the forces in all directions. The extreme pressure generated by the compression of the inner bend results in strong elongation out of the plane of the scaffold. These forces draw material from *both* the inner and outer bend to create the bulge, a feature observed at the inner bend of all crests of the crimped subassembly (U, W, and Y, Figures 3.1-3.2). The combination of high pressure and continued rotation of the arms creates shear in the (θ, z) -plane that is dissipated through plastic deformation and crazing on opposite sides of the bulge. These dissipation mechanisms are confined to a small deformation zone (less than 100 μm across), so most of the material maintains its structural integrity. The competing forces of shear in the (θ, z) -plane and extension in the r -direction result in craze formation in a region in which lamellar breakup and coarse chain slip indicate that particularly high stresses developed during the crimping process. This spatial distribution of crazing may have a significant effect in the subsequent deployment of the scaffold (see Chapter 4). Here, we have shown that X-ray microdiffraction with sub-micron spot size is a powerful tool for mapping and understanding the spatial variation of microstructure. In view of the central importance of understanding the fully three-dimensional transformation of structure during crimping, future characterization work should apply X-ray microdiffraction to crimped-scaffold sections cut in the (θ, r) - and (r, z) -planes to directly verify and quantify the orientation

distribution inferred from the present results. Coordinated studies of crimped, deployed, and partially hydrolyzed scaffolds are also recommended as a means of discovering the role of structural transformations during crimping and deployment on the time course of degradation^{30,31}.

3.5 Methods

3.5.1 Materials

Thin sections of as-cut subassemblies

Individual crimped subassembly rings were embedded in TissueTek (Sakure), glued into screws, and then transferred to the microtome to equilibrate at -25 °C for 20 minutes. Thin sections 10 - 15 μm thick were microtomed using a glass knife in the radial direction from an as-cut subassembly using a Powertome XL (RMC Products). The thin sections were provided by Abbott Vascular.

3.5.2 Determination of U crest bend angle

To evaluate the bend angle of a U crest in the as-cut and crimped state, a protractor image was overlaid with a photograph of an as-cut subassembly and the SEM image of a crimped subassembly in Photoshop®. Black lines were used as guides to determine the angles. The angle of arms with respect to the bend is +50° and -50° and +5° and -5° for the as-cut and crimped subassembly, respectively.

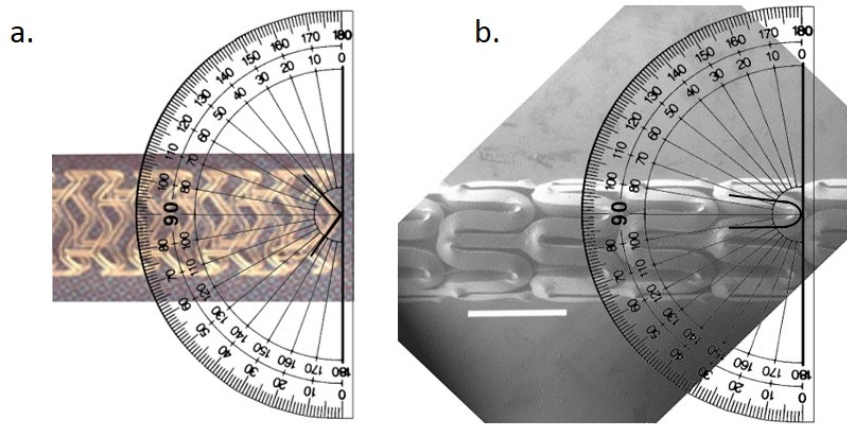


Figure 3.11 Photoshop overlay of a protractor image with a) photograph of an as-cut subassembly and b) an SEM micrograph of a crimped subassembly.

3.5.3 Polarized light microscopy

Micrographs

Polarized light micrographs were acquired in a Zeiss Universal microscope at 4X or 10 X magnification through crossed linear polarizers equipped with a Canon EOS DS30 camera.

Determination of shear bands and crazes

Sections were placed between crossed polarizers and rotated 360°. Images were acquired every 45° to determine the nature of the observed features. When the material remains continuous, light is not reflected or scattered. Therefore, light makes it through the specimen, which alternates between dark and light as the sample is rotated. Where discontinuities occur the interfaces reflect light, and any fibrils or other microscopic features scatter light and appear dark at all orientations as the sample is rotated under polarized light. The bands that remain dark at all orientations of the rotation stage are not shear bands and are consistent with crazes and/or cracks.

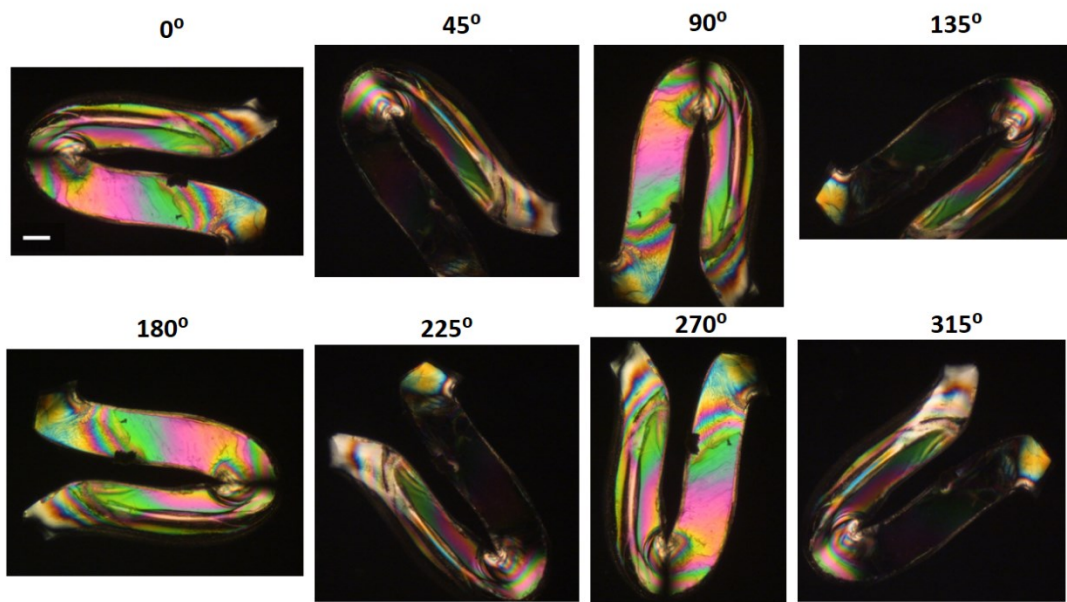


Figure 3.12 Polarized light micrographs of the 10-13 μm thick section acquired in a Zeiss Universal microscope through crossed linear polarizers equipped with a Canon EOS DS30 camera. This section was cut at a distance of about 40 μm from the OD. The sample was rotated at increments of 45° (choice of 0° is arbitrary).

Determination of axis orientation

Rotation of a specimen between crossed linear polarizers can be used to determine the chain axis orientation in the millimeter scale. A specimen is placed between crossed linear polarizers and rotated 360° at small increments (Fig. 3.12a). The regions that appear dark have the chain axis parallel to the direction of either the polarizer or the analyzer (Fig. 3.12b).

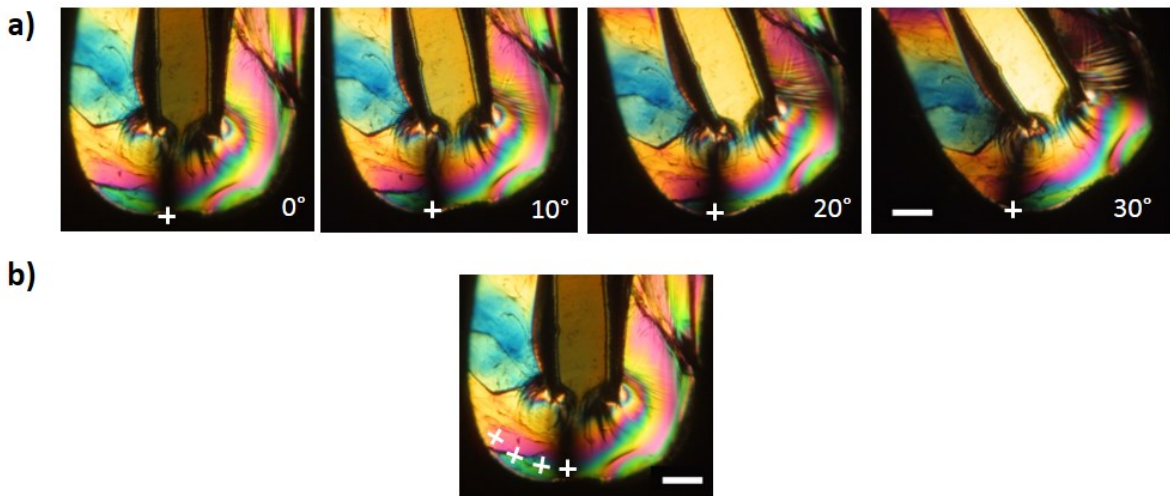


Figure 3.13 Polarized light micrographs of a section cut from a W crest of a crimped subassembly. a) The thin section is rotated counter-clockwise every 10° (choice of 0° is arbitrary). The white cross shows the orientation of the crossed linear polarizers. When a region of the specimen is dark the chain axis is oriented parallel to the horizontal line of the cross. b) A composite image of the shows the chain axis orientation along part of the outer bend. The same procedure can be applied to the rotation of the specimen clockwise. Scale bars are 100 μm .

3.5.4 Wide-angle X-ray microdiffraction

Wide-angle X-ray microdiffraction experiments were performed at beamline 2-ID-D of the Advanced Photon Source at Argonne National Lab. Diffraction patterns were collected using a Mar CCD detector at distance of 119.73 mm from the sample holder. The source wavelength was 1.227 \AA and the beam spot size was 0.2 μm . The diffraction patterns were calibrated for centering and detector distance using a cerium oxide (CeO_2) standard. The thin section was attached on Kapton tape and placed in front of the beam using an aluminum holder. To characterize the crystalline microstructure at the bend of the thin section presented herein, we acquired microdiffraction patterns from a 230 μm x 210 μm (Fig. 3.3) area. Data was acquired at positions spaced 10 μm apart for a total of 483 patterns. The data acquisition time was 30 seconds. Image analysis code was developed using MATLAB®. This code was used for data reduction to obtain radial and azimuthal

intensity profiles, and to extract quantitative values for maximum intensity, crystal orientation, and crystal spacing.

References

- (1) De Beule, M.; Mortier, P.; Ridy, V. I.; Verheghe, B.; Segers, P.; Verdonck, P. Plasticity in the Mechanical Behaviour of Cardiovascular Stents during Stent Preparation (crimping) and Placement (expansion). *Key Eng. Mater.* **2007**, *340-341*, 847–852.
- (2) Möller, D.; Reimers, W.; Pyzalla, A.; Fischer, A. Residual Stresses in Coronary Artery Stents. *J. Biomed. Mater. Res.* **2001**, *58*, 69–74.
- (3) Zhao, S.; Gu, L.; Froemming, S. R. On the Importance of Modeling Stent Procedure for Predicting Arterial Mechanics. *J. Biomech. Eng.* **2012**, *134*, 121005.
- (4) Mehta, A.; Gong, X.-Y.; Imbeni, V.; Pelton, A. R.; Ritchie, R. O. Understanding the Deformation and Fracture of Nitinol Endovascular Stents Using In Situ Synchrotron X-Ray Microdiffraction. *Adv. Mater.* **2007**, *19*, 1183–1186.
- (5) Nematzadeh, F.; Sadrnezhad, S. K. Effects of Crimping on Mechanical Performance of Nitinol Stent Designed for Femoral Artery: Finite Element Analysis. *J. Mater. Eng. Perform.* **2013**, *22*, 3228–3236.
- (6) Bevis, M.; Crellin, E. B. The Geometry of Twinning and Phase Transformations in Crystalline Polyethylene. *Polymer* **1971**, *12*, 666–684.
- (7) Galeski, A. *Strength and Toughness of Crystalline Polymer Systems*; Elsevier, 2003; Vol. 28, pp. 1643–1699.
- (8) Argon, A. S. *The Physics of Deformation and Fracture of Polymers*; Cambridge University Press, 2013; pp. 342–390.
- (9) Roylance, D. Yield and Plastic Flow. In *Modules in Mechanics of Materials*; Cambridge, MA, 2001; pp. 1–19.
- (10) Kramer, E. J. Microscopic and Molecular Fundamentals of Crazing. *Crazing Polym.* **1983**, *52-53*, 1–55.
- (11) De Focatiis, D. S. a.; Buckley, C. P. Craze Initiation in Glassy Polymers: Quantifying the Influence of Molecular Orientation. *Polymer* **2011**, *52*, 4045–4053.
- (12) Chau, C. C.; LaFollette, W. R. Shear Yielding in Blown Oriented Polystyrene Films. *Adv. Mater.* **2000**, *12*, 1859–1864.

(13) Hou, H.; Wilkes, G. L. Orientation-Dependent Mechanical Properties and Deformation Morphologies for Uniaxially Melt-Extruded High-Density Polyethylene Films Having an Initial Stacked Lamellar Texture. *J. Mater. Sci.* **1998**, *33*, 287–303.

(14) Donald, M. D.; Kramer, E. J. The Competition between Shear Deformation and Crazing in Glassy Polymers. *J. Mater. Sci.* **1982**, *17*, 1871–1879.

(15) Estevez, R.; Tijssens, M. G. a.; Van der Giessen, E. Modeling of the Competition between Shear Yielding and Crazing in Glassy Polymers. *J. Mech. Phys. Solids* **2000**, *48*, 2585–2617.

(16) Mahendrasingam, A.; Blundell, D. J.; Parton, M.; Wright, A. K.; Rasburn, J.; Narayanan, T.; Fuller, W. Time Resolved Study of Oriented Crystallisation of Poly(lactic Acid) during Rapid Tensile Deformation. *Polymer* **2005**, *46*, 6009–6015.

(17) Hébert, J.-S.; Wood-Adams, P.; Heuzey, M.-C.; Dubois, C.; Brisson, J. Morphology of Polylactic Acid Crystallized during Annealing after Uniaxial Deformation. *J. Polym. Sci. Part B Polym. Phys.* **2013**, *51*, 430–440.

(18) Stoclet, G.; Seguela, R.; Lefebvre, J. M.; Elkoun, S.; Vanmansart, C. Strain-Induced Molecular Ordering in Polylactide upon Uniaxial Stretching. *Macromolecules* **2010**, *43*, 1488–1498.

(19) Stoclet, G.; Seguela, R.; Vanmansart, C.; Rochas, C.; Lefebvre, J.-M. WAXS Study of the Structural Reorganization of Semi-Crystalline Polylactide under Tensile Drawing. *Polymer* **2012**, *53*, 519–528.

(20) Ou, X.; Cakmak, M. Influence of Biaxial Stretching Mode on the Crystalline Texture in Polylactic Acid Films. *Polymer* **2008**, *49*, 5344–5352.

(21) Mulligan, J.; Cakmak, M. Nonlinear Mechanooptical Behavior of Uniaxially Stretched Poly(lactic Acid): Dynamic Phase Behavior. *Macromolecules* **2005**, *38*, 2333–2344.

(22) Ou, X.; Cakmak, M. Comparative Study on Development of Structural Hierarchy in Constrained Annealed Simultaneous and Sequential Biaxially Stretched Polylactic Acid Films. *Polymer* **2010**, *51*, 783–792.

(23) Liu, H.; Chen, N.; Fujinami, S.; Louguine-Luzgin, D.; Nakajima, K.; Nishi, T. Quantitative Nanomechanical Investigation on Deformation of Poly(lactic Acid). *Macromolecules* **2012**, *45*, 8770–8779.

(24) Renouf-Glauser, A. C.; Rose, J.; Farrar, D. F.; Cameron, R. E. The Effect of Crystallinity on the Deformation Mechanism and Bulk Mechanical Properties of PLLA. *Biomaterials* **2005**, *26*, 5771–5782.

(25) Alexander, L. E. *X-Ray Diffraction Methods in Polymer Science*; Wiley Interscience: New York, 1969.

- (26) Balta-Calleja, F. J.; Vonk, C. G. *X-Ray Scattering of Synthetic Polymers*; Jenkins, A. D., Ed.; Elsevier B.V.: Amsterdam, 1989.
- (27) Godshall, D.; Wilkes, G.; Krishnaswamy, R. K.; Sukhadia, A. M. Processing-Structure-Property Investigation of Blown HDPE Films Containing Both Machine and Transverse Direction Oriented Lamellar Stacks. *Polymer* **2003**, *44*, 5397–5406.
- (28) Galeski, A.; Bartczak, Z.; Argon, A. S.; Cohen, R. E. Morphological Alterations during Texture-Producing Plastic Plane Strain Compression of High-Density Polyethylene. *Macromolecules* **1992**, *25*, 5705–5718.
- (29) Bartczak, Z.; Cohen, R. E.; Argon, A. S. Evolution of the Crystalline Texture of High-Density Polyethylene during Uniaxial Compression. *Macromolecules* **1992**, *25*, 4692–4704.
- (30) Soares, J. S.; Moore, J. E.; Rajagopal, K. R. Modeling of Deformation-Accelerated Breakdown of Polylactic Acid Biodegradable Stents. *J. Med. Device.* **2010**, *4*, 1–10.
- (31) Radu, M. D.; Onuma, Y.; Rapoza, R. J.; Diletti, R.; Serruys, P. W. In Vivo Visualisation by Three-Dimensional Optical Coherence Tomography of Stress Crazing of a Bioresorbable Vascular Scaffold Implanted for Treatment of Human Coronary Stenosis. *EuroIntervention* **2012**, *7*, 1461–1463.

CHAPTER 4

Effect of Deployment on Scaffold Morphology

4.1 Introduction

Successful implantation of a balloon-expandable stent or scaffold in the artery depends on its structural integrity after deployment. Among the factors affecting success are the geometry and mechanical stability of the struts, and the correct sizing of the scaffold diameter and length for the each patient¹⁻⁴. Research on the effect of the expansion stresses during deployment so far has focused on two different aspects: first, the structural properties of metal stents and second, the impact on the artery itself.^{5,6} The pioneering work of Dumoulin and Cochelin demonstrated that Finite Element Analysis (FEA) can be used to predict the stresses on the stent struts⁷ and since then, FEA has become a standard tool for the development of new products. For example, other studies have investigated the pressure limit to avoid failure during expansion⁸; the importance of the balloon's dimensions and uniformity of the balloon's folding pattern^{9,10}; the relationship between fracture and strut thickness¹¹; and the coupling of the stresses on the artery and the retraction of the stent¹².

The overwhelming majority of FEA deal with metallic stents and studies simplify the material as homogenous and isotropic. However, it has been demonstrated that because the dimensions of metallic stents are in the order of the individual grains, the specifics of microstructure plays a great role in the mechanics of fracture and stability during deployment^{13,14}. For biodegradable polymeric scaffolds the presence of crystalline and

amorphous phases dictates both the stress dissipation during deployment and the scaffold's subsequent degradation¹⁵. Thus, understanding the microstructure evolution of the PLLA scaffold during deployment is extremely important for understanding its in-vivo performance.

During deployment, scaffolds are expanded by inflation of a balloonⁱ. Once the desired diameter is reached, the balloon is deflated and withdrawn, leaving the scaffold in the expanded state to hold the blood vessel open. The scaffold strength is provided by rings connected by links parallel to the axial direction. Each ring is composed by alternating Y, W, and U crests (Fig. 4.1). Research on the expansion of various designs of biodegradable scaffolds has focused on bulk properties to assess their mechanical stability^{16–20}. However, understanding the bulk behavior of polymers requires understanding of the underlying microstructure, e.g. crimping leads to the coexistence of very different microstructures in close proximity in the inner bends (see Chapter 3 and Fig. 4.1). Here, we combine scanning electron and polarized light microscopy with synchrotron X-ray microdiffraction to investigate the consequences of the structure formed during crimping on the physical changes during deployment.

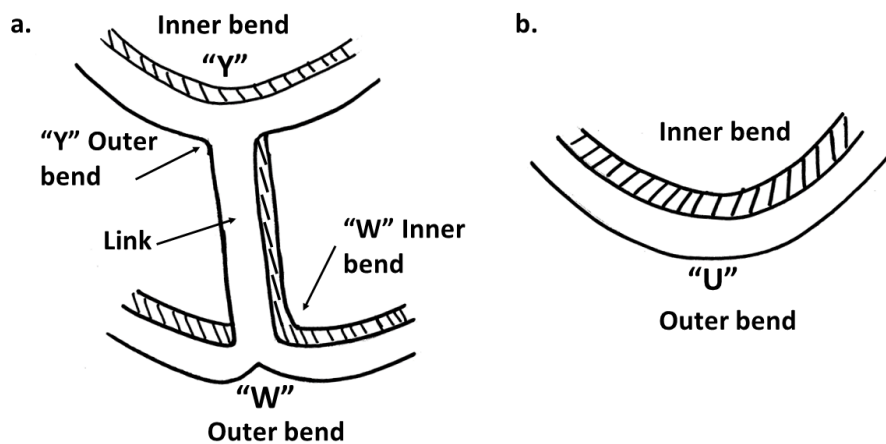


Figure 4.1 Schematic showing the location of inner and outer bends for a) “W”, “Y, and b) “U” crests.

4.2 Results

4.2.1 Scanning electron microscopy

Scanning electron microscopy (SEM) micrographs of expanded scaffolds show the diamond-shaped voids at the inner bends of U, Y, and W crests (Fig. 4.2). It is not possible to compare the size of the diamond-shaped voids of the Y and W crests (Fig. 4.2 a-b) to those of U crests (Fig. 4.2 c-d) because they are on opposite sides of the circumferential rings of the scaffold. Nevertheless, it appears that the diamond-shaped voids on the inner bends of Y and W crests are systematically smaller than those on U crests. High magnification SEM micrographs of diamond-shaped voids under U crests in both regularly expanded (Fig. 4.3 a) and expanded to failure (Fig. 4.3 b-c) show that the fundamental deformation mechanism of void formation does not change with expansion ratio.

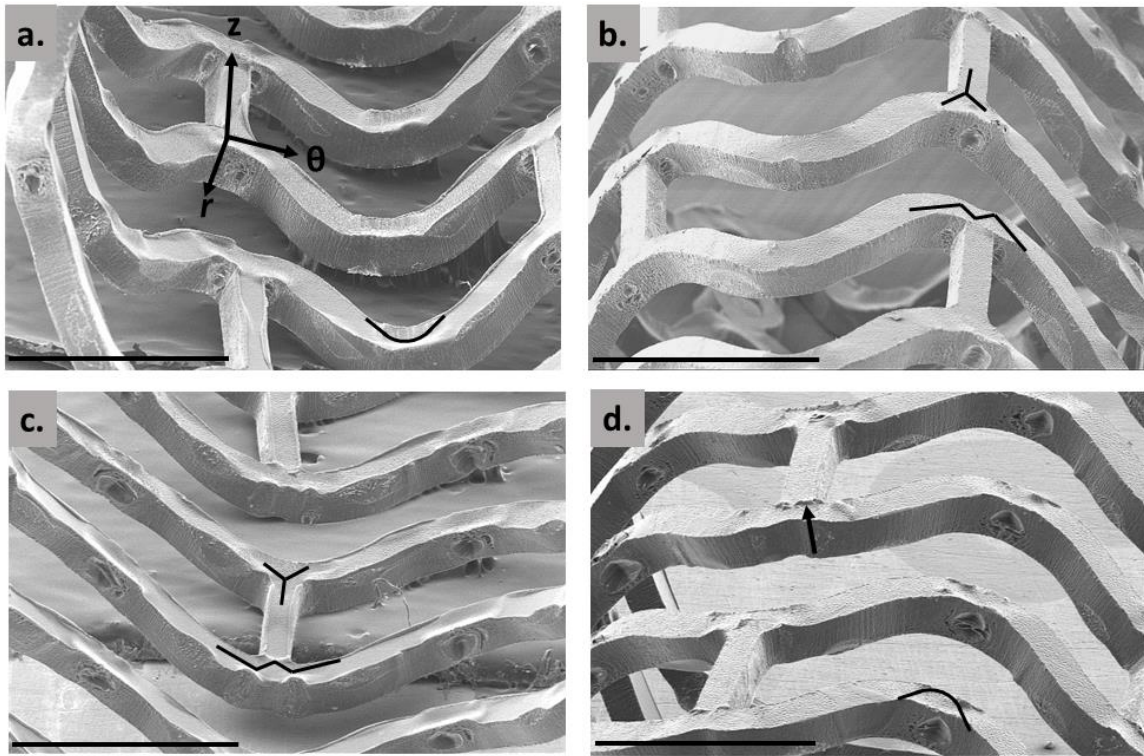


Figure 4.2 Scanning electron microscopy (SEM) micrographs of scaffolds subjected to expansion to failure *in vitro*. The letters indicate the Y, W, and U crests. View of the inner bends Y and W crests from a) the inner diameter of the scaffold (the relationship to the cylindrical coordinate system is shown) and b) from the outer diameter. c) View of U crests from the inner diameter and b) from the outer diameter of the scaffold. The W crests have a diamond shaped void on each side of the link and Y and U crests have one. The material that appears to peeling off (black arrow) is from the drug coating (not the PLLA core). Scale bars are 1000 μm . Image contrast has been adjusted for uniformity. Micrographs provided by Abbott Vascular.

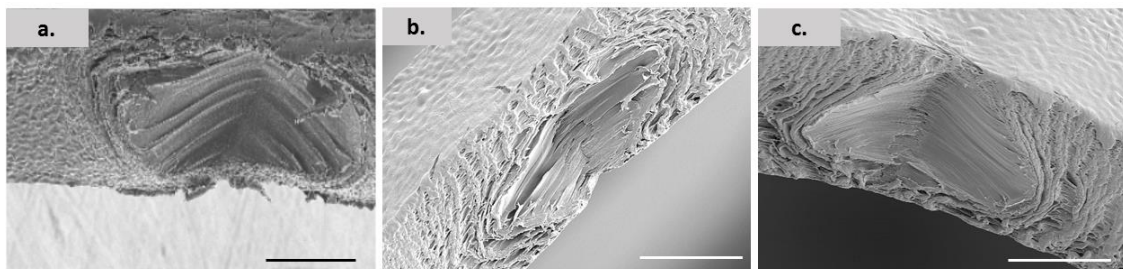


Figure 4.3 High magnification SEM micrographs of diamond-shaped voids under U crests of an expanded scaffold. a) Void created under regular expansion ratio. b) and c) Voids created under high expansion ratio. Scale bars are 100 μm .

4.2.2 Polarized light microscopy

In view of the common features amongst the Y, W, and U crests observed with SEM, we continue our analysis using one type of crests (U) as a model. Thin sections in the (θ, z) -plane show the retardance increasing and the decreasing from the arms to inner bend (Fig. 4.4). For example moving left to right in the deployed U cut from about 90 μm from the OD (Fig. 4.4) the retardance increases from 400 nm (gold) to 500 nm (burgundy) to 600 nm (navy blue) to 700 nm (sky blue) to 900 nm (yellow) and then decreases again sequentially from 700 nm to 600 nm to 500 nm. The inner bend region has a retardance of about of 400 nm and a micro-crack is observed (white rectangle, Fig. 4.4a)ⁱⁱ. Moving away from the center of the inner bend toward the right arm and the outer bend, the reverse sequence of colors is observed.

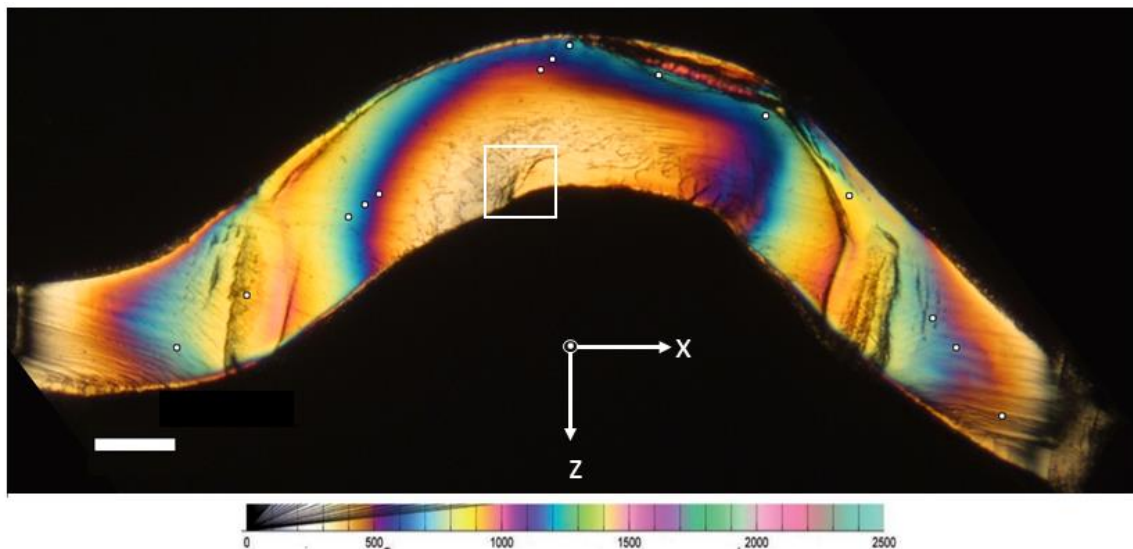


Figure 4.4 Polarized light micrographs of sections cut from deployed U crest about 90 μm away from the OD. The dots on this image are used in the text to describe the increase and decrease of retardance. The micrograph was acquired in a Zeiss Universal microscope through crossed linear polarizers equipped with a Canon EOS DS30 camera. Scale bars are 100 μm .

4.2.3 X-ray microdiffraction

The microstructure of the thin section shown in Figure 4.3 was examined by X-ray microdiffraction at beamline 2-ID-D of the Advanced Photon Source (APS) of Argonne National Lab. Selected diffraction patterns acquired from the line scans show that the dominant crystal form is α' (Figs. 4.5 and 4.6). To quantify the spatial microstructure evolution we considered the following quantities: I_{\max} of $I(\Phi)$, $I(\Phi)*P$, Φ_{\max} , and Φ -FWHM (Fig. 4.7). (The maximum intensity of the (110)/(200) peak is weighted by a weighting factor, P , to account for the intersection of the diffraction sphere with the orientation sphere of the crystal population²¹ (see Methods, section 4.5.4)). The diffraction patterns correspond to crystals oriented mainly along the θ -direction. Selected diffraction patterns acquired at the inner bend of the section are shown in Figure 4.8.

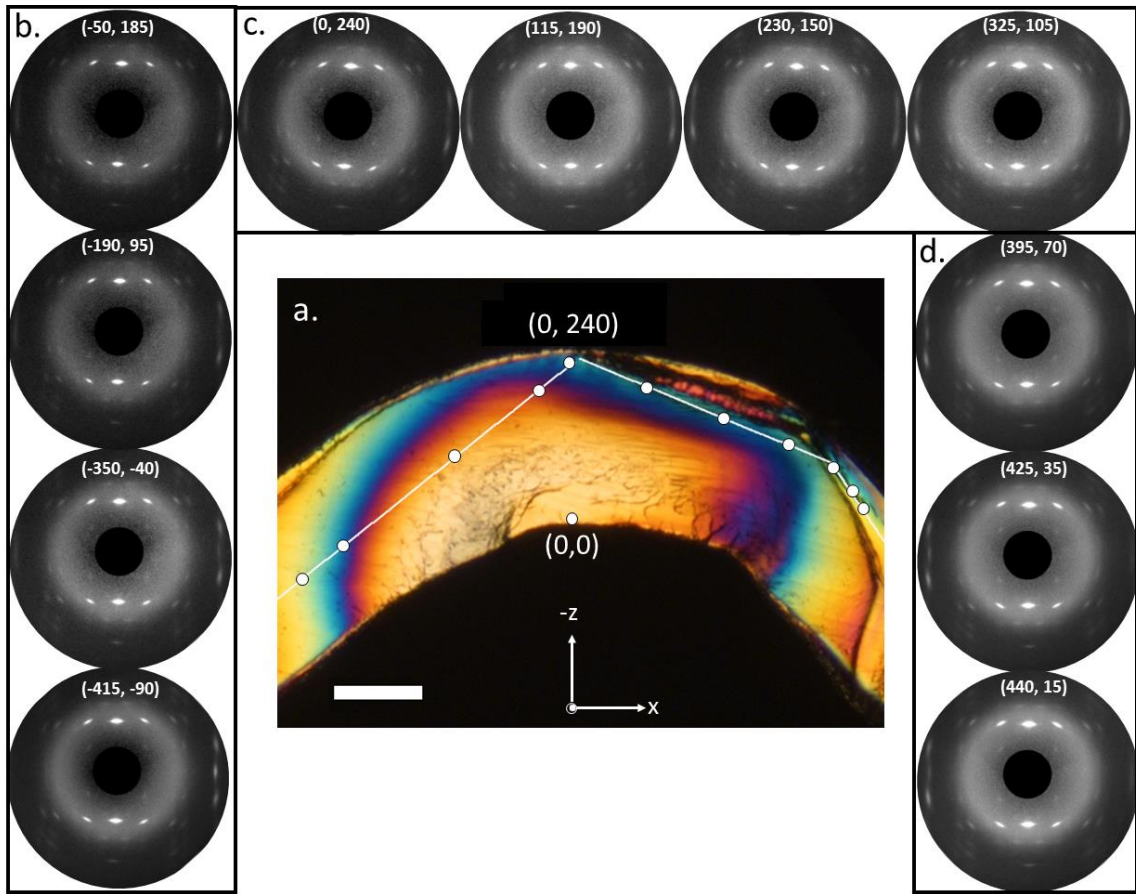


Figure 4.5 a) Polarized light micrograph of the thin section that was examined with X-ray microdiffraction. The (x,z)-axes show the coordinate system. White dots on the micrograph show the location at which the diffraction patterns in a-c were acquired. Scale bar is 100 μm . b-d) Selected microdiffraction patterns acquired at 2-ID-D with a 0.2 μm beam spot size. The patterns have been rotated 138° from their original laboratory frame to match the orientation of the polarized light micrograph.

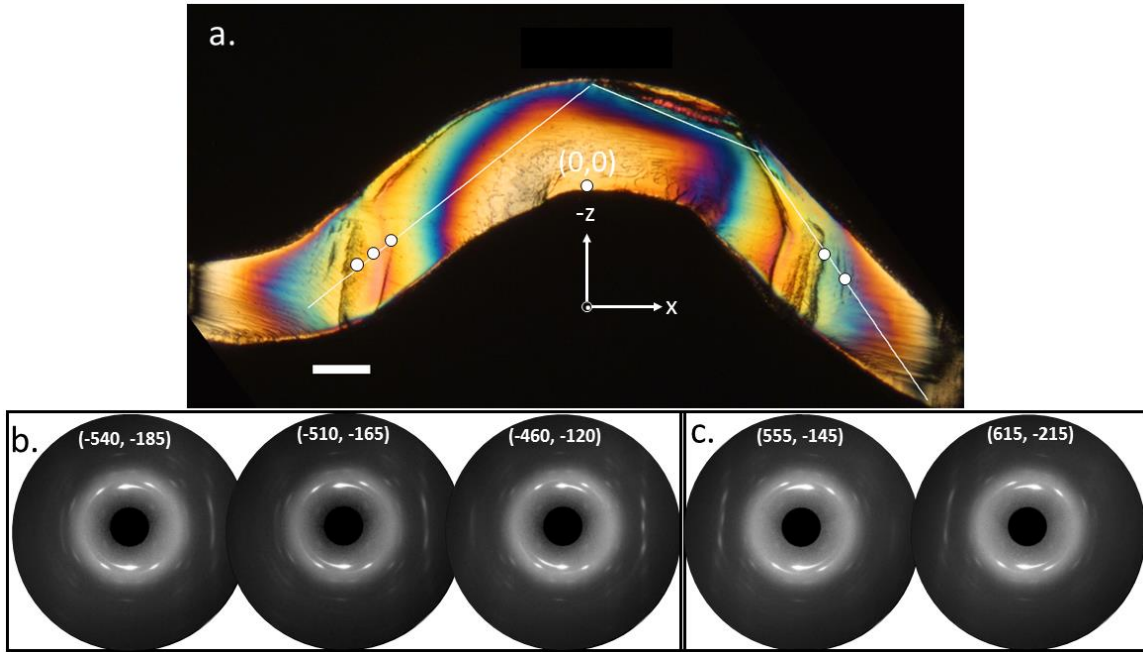


Figure 4.6 a) Polarized light micrograph of the thin section that was examined with X-ray microdiffraction. The (x,z)-axes show the coordinate system. White dots on the micrograph show the location at which the diffraction patterns in b and c were acquired. Scale bar is 100 μm . b) and c) Selected microdiffraction patterns acquired at 2-ID-D with a 0.2 μm beam spot size. The patterns have been rotated 138° from their original laboratory frame to match the orientation of the polarized light micrograph.

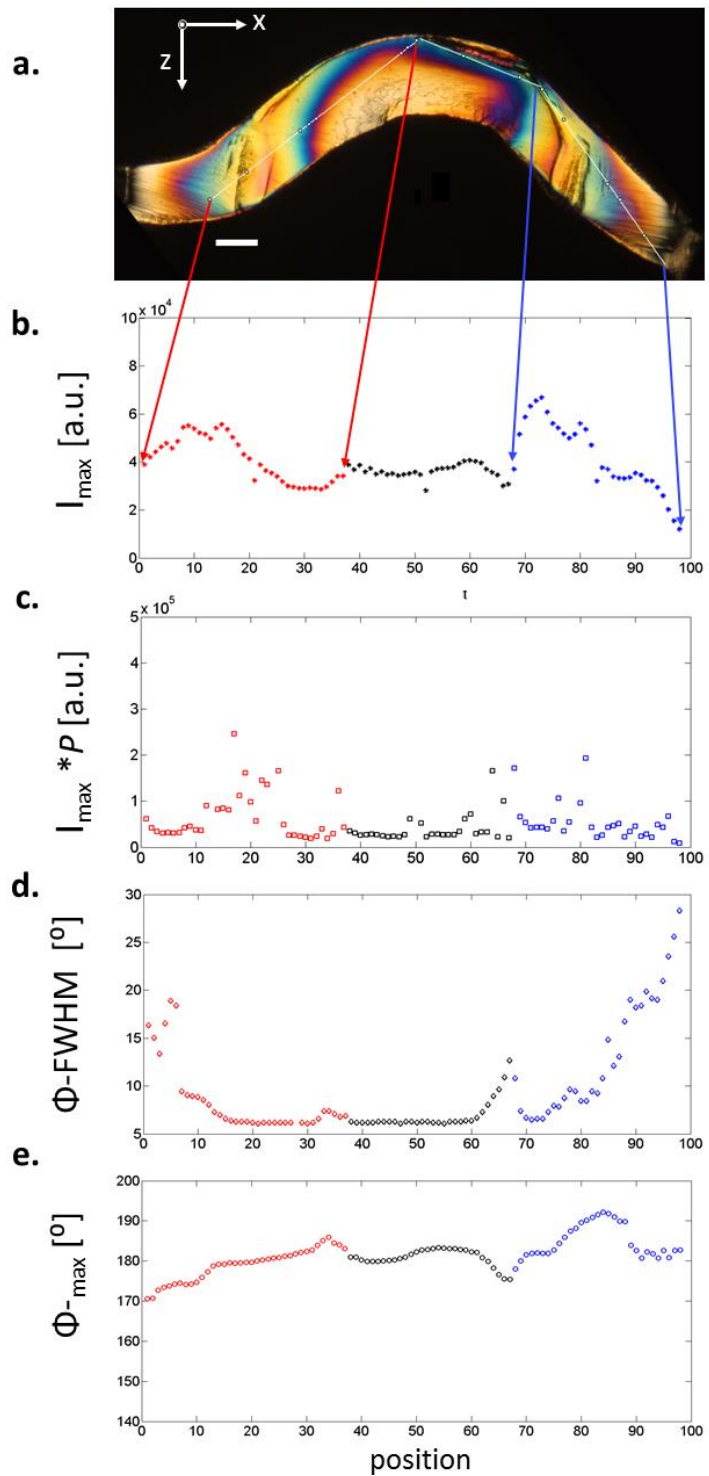


Figure 4.7 Quantitative analysis of the 98 microdiffractions patterns along the arms and outer bend of the thin section. a) Polarized light micrograph of the thin section with an overlay showing the line scans. From left to right, each scan has 37, 30, and 31 points. Scale bar is 100 μm . The red and blue lines indicate the first and last point of the first and third line scan, respectively. b) Variation in the maximum intensity of the $I(\Phi)$ curve. c) Variation in the maximum intensity of the $I(\Phi)$ curve

multiplied by the orientation weighing factor f . d) Spatial variation in Φ -FWHM. e) Spatial variation in Φ .

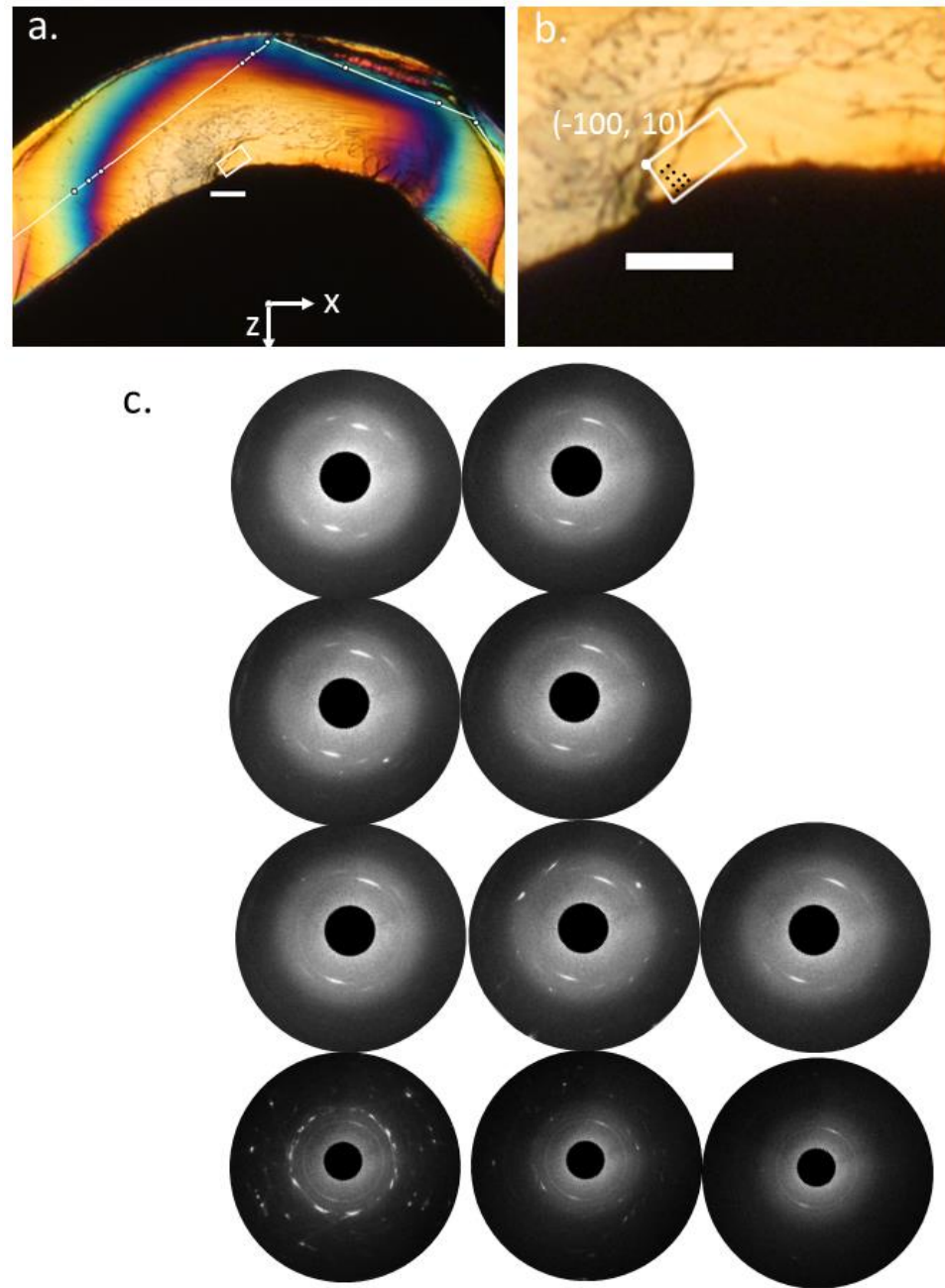


Figure 4.8 a) Cropped polarized light micrograph shows the position of the 2D scan with respect to the line scans. Scale bar is 50 μm . b) Higher magnification polarized light micrograph of the 20 μm x 40 μm area scan. Scale bar is 50 μm . c) Representative microdiffraction patterns from the area scan, rotated 138° to match the orientation of the polarized light micrograph. Their positions are indicated by the black dots on part b. Patterns are 2 μm x 4 μm apart.

4.3 Discussion

To understand the structure of a deployed scaffold in relation to the structure created during crimping, we chose to study a section cut in the (r, θ) -plane of a U crest, like the section examined in Chapter 3. Here, the section was taken approximately 90 μm from the outer diameter, about 15 μm past the midplane (i.e., closer to the inner diameter (ID) than the outer diameter (OD), and past the deepest point of the diamond-shaped void). In the crimped state, material this close to the midplane was not displaced out of the (θ, z) -plane. Similar to Chapter 3, the section is about 10 μm thick, representing 1/15th of the total thickness of the scaffold. During deployment, the outer bend experiences θ -compression (top of Fig. 4.9) and the inner bend experiences θ -elongation, (bottom of Fig. 4.9); the magnitude of the stress field varies strongly between the outer and inner bends, with the steepest gradient near the inner bend.²² It is interesting to note, however, that the structure at the outer bend shows no indication of compressive deformation.

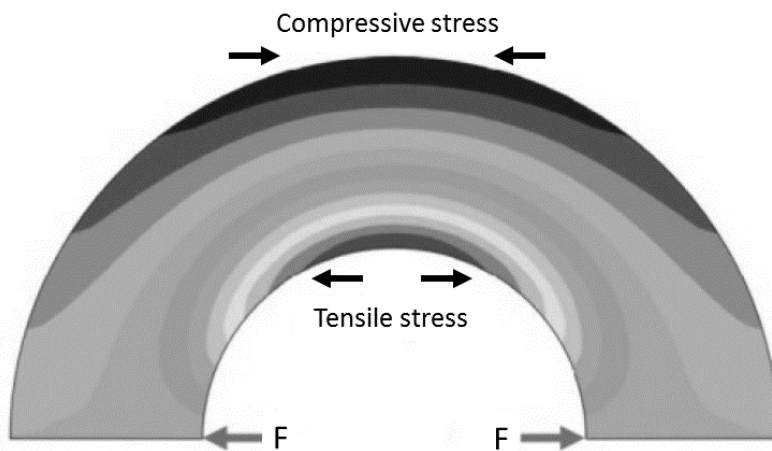


Figure 4.9: Schematic showing the forces involved in deployment. The expansion forces drive the arms away from each other. This imposes tensile stress on the inner bend and compressive

stress at the outer bend. The area of compressive stress is larger than the area of tensile stress. Schematic from Jang *et al.*²²

At the outer bend, the PLLA chains are strongly aligned with c-axis in the θ -direction and are highly ordered as seen from the presence of higher order peaks (Fig. 4.5c and d). This type of microstructure can only be formed after stretching at a high draw ratio²³⁻²⁶ so it must be inherited from the elongation of the outer bend during the crimping process. During deployment, the outer bend is under compression, yet the strong orientation is not lost (Fig. 4. 5b-d, patterns (-415, -90) to (230, 150)) and there is no evidence of fracture or buckling (see SEM of outer bends, Fig. 4.2b and d). The Φ -FWHM near the outer bend is remarkably uniform (Fig. 4.7d) and corresponds to a very narrow distribution of oriented crystals. This evidence points strongly to a dominant effect of crimping on the creation of order at the outer bend; during subsequent deployment, the structure in the outer bend constrains deformation and remains unmodified.

The region of highly aligned crystals in the deployed sample can be compared to the microdiffraction results in the crimped state (Chapter 3, Fig. 3.6) to understand its shape and extent. The present section has an approximately semi-circular area of high retardance (approximately 650 nm, turquoise/purple on Fig. 4.5a), which extends away from the outer bend (e.g., positions (-415, -90) and (-350, -40) in Fig. 4.5b). Although quantitative comparison between the deployed and crimped sections is not possible, the overall appearance of the broad arc of high orientation in the deployed one corresponds to a narrow arc in the crimped one. For example, the displacement that occurs during deployment, would move the points at coordinates (-80, 70) and (100, -70) in the crimped section shown in Figure 3.6 to approximately (-190, 95) and an intermediate point between (230, 150) and

(325, 105) in the deployed section in Figure 4.5. The reorientation of the arms during deployment accounts for the change in orientation direction of the c-axis between the corresponding diffraction patterns (cf. Figures 3.6 and 4.5). Thus, the semicrystalline structure in the deployed scaffold accords with that present in the crimped state.

A surprising feature was discovered in the microdiffraction patterns in the arms of the deployed U crest, which show “comet”-shaped (100)/(200) peaks (Fig. 4.6 b and c) far away from the deformation zone of the bend (see Chapter 3). The orientation of the comet “heads” corresponds to the arms rotating in the $\pm x$ -direction. In a crimped section (e.g., Fig. 3.6, pattern (30, 50)), comet shaped peaks were observed near the inner bend and in the small zone of intense deformation. Here in the deployed U, the comet shaped patterns are observed over a large area: in the line scans shown in Figure 4.6a, the patterns with comet shaped peaks in Figure 4.6b and c are representative of 10 consecutive patterns that extend over approximately. Although we do not understand how these could form during deployment, the comets “tails” in the crimped state accord with lamellar fragments created during plastic deformation (Fig. 3.6).

A striking feature of the diamond shaped voids is the absence of fibrils bridging across their surfaces (SEM micrographs Figs. 4.2 and 4.3). Furthermore, in contrast to the microdiffraction results in the crimped state, very few patterns show the discrete bright reflections associated with craze fibrils (Fig 4.8, patterns that are within 10 μm of the inner edge of the U crest). This is particularly interesting because hydration has been shown to facilitate craze formation in PLLA²⁷ and deployment in vitro is performed in an aqueous medium. In view of many other sections that were examined with X-ray microdiffraction, the low occurrence of fibril patterns in the diamond shaped voids indicates that the

deformation of the inner bend during deployment does not involve additional crazing or fracture. Instead, the faces of diamond-shaped voids (Figs. 4.2 and 4.3) separate cleanly, which is characteristic of surfaces that are tangent to the c-axis orientation. In the literature on semicrystalline polymers, it is known that very low loads are required to open surfaces tangent to the chain direction²⁸. Therefore, we hypothesize that during deployment, the outer bend does not compress because the inner bend so easily elongates due to formation of the diamond-shaped voids. Indeed, the integrity of the outer bend appears to be protected by the low stress required to open the diamond shaped void.

At first glance, it may seem surprising that the chain axis is not orthogonal to the surfaces of the diamond shaped voids: after the expansion process, the chains are oriented in the θ -direction, which would result in craze formation across the diamond shaped voids. However, the restructuring during crimping results in c-axis oriented along the r-direction the inner bend of a U crest (Fig. 4.10 and Chapter 3). During deployment, tensile stress is imposed in the θ -direction—orthogonal to the c-axis orientation along r. Consequently, the newly exposed surfaces form without breaking chains or forming crazes (Fig. 4.11). This accords with clinical studies that observed diamond-shaped voids and found that they do not compromise the *in vivo* mechanical performance of the scaffold.²⁹

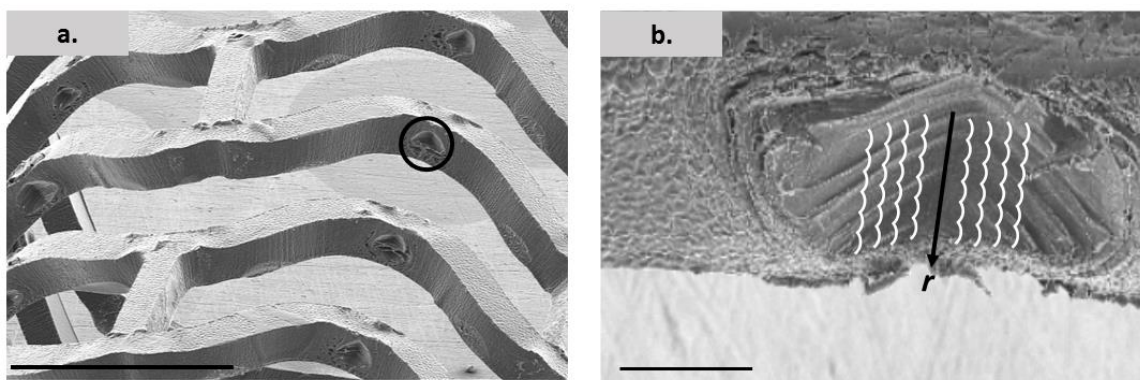


Figure 4.10 Chain orientation at the inner surface of a diamond-shaped void. a) Scanning electron microscopy (SEM) micrograph of a scaffold subjected to expansion to failure *in vitro*. The black circle shows the diamond-shaped void at the inner bend of a U crest. Scale bar is 1000 μm . b) High magnification SEM micrograph of a diamond-shaped void created under regular expansion ratio. The white curved lines show that the chain c-axis is aligned in the r direction. Scale bar is 100 μm . Micrographs provided by Abbott Vascular.

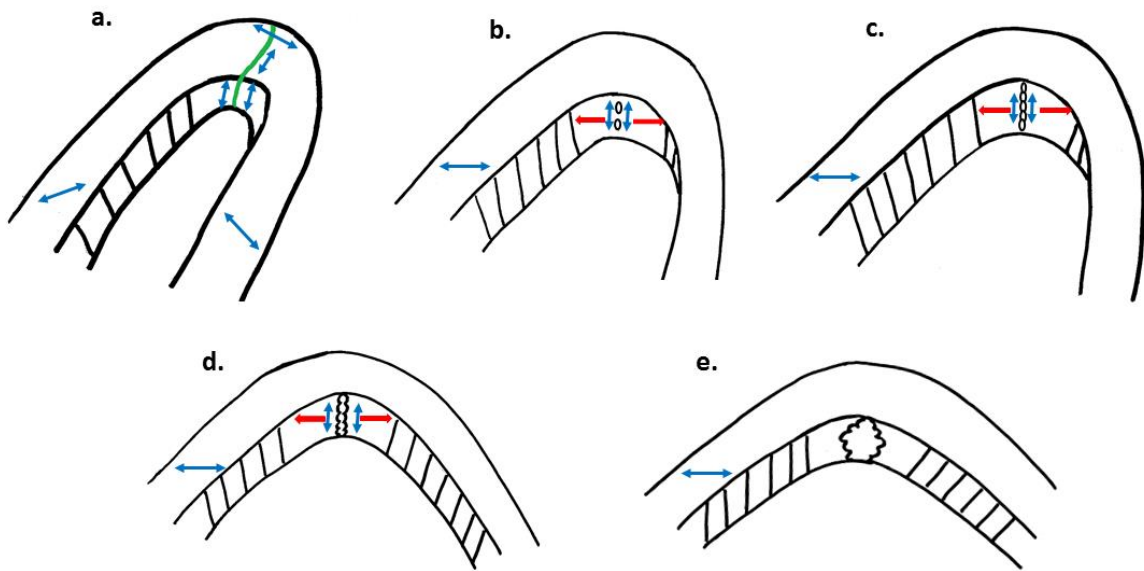


Figure 4.11 Schematic showing the formation mechanism of a diamond-shaped void at the inner bend of a U crest. The blue double arrows indicate the polymer chain orientation and the red thick arrows indicate the tensile stress direction. a) In the crimped U, the chains at the inner bend are aligned in the $\pm r$ direction. b) Shortly after expansion begins, micro-voids form. c) As the expansion continues, the number of micro-voids increases. d) Eventually, the micro-voids will start separating. e) Finally, the complete separation of surfaces results in diamond-shaped voids.

4.4 Conclusions

The microstructure of the deployed scaffolds cannot be understood without considering the crimping step. The outer bend experienced significant elongation during crimping, which introduced a strongly oriented population of crystallites. During deployment, the outer bend is under compression, yet the orientation is not lost and there is no evidence of fracture or buckling. Rather, the material resists deformation as a result of the structure that was created during crimping. Thus, structure formation during

crimping governs the behavior during deployment by creating an “iron band” along the outer bend that deforms only minimally and protects the crests from fracture during deployment.

The salient feature of the inner bend is the diamond-shaped void. Its formation also has roots in the microstructure created during crimping, which causes the c-axis to orient in the r-direction at the inner bend. It is striking that these diamond-shaped voids do not involve crazes. There are no fibrils bridging across the fracture surfaces inspected by SEM, in which a large number of diamond-shaped voids are seen. This is particularly interesting, since deployment is performed in an aqueous environment, which facilitates formation and enlargement of crazes. This interesting behavior results from the relative orientation of the chains axis and the loading geometry: chains oriented along r peel apart relatively easily when a tensile stress is imposed along the θ -direction. This separation is manifested as diamond-shaped voids. Thus, the formation of diamond-shaped voids happens with no loss of material.

Here, we have demonstrated that the microstructure created during crimping dictates the microstructure in the deployed state. The strong outer bend and pliable inner bend contribute to successful deployment³⁰: the inner bend allows for gracefulⁱⁱⁱ expansion from the crimped state due to the mutually orthogonal directions of the chains and the tensile stress. This leaves the strong outer bend unperturbed during deployment, leaving intact the structure that resists the compressive forces of the artery. Together with results on the microstructure of crimped bioresorbable scaffolds (Chapter 3), the present study of the deployed state provides a foundation for further investigation, for example, of the relationships between microstructure and hydrolytic degradation.

4.5 Methods

4.5.1 Materials

To simulate the deformation the scaffolds experience upon deployment in the artery, a crimped subassembly was deployed *in vitro* before studying it. The crimped subassembly was submerged in a buffer solution at 37 °C and after a two-minute incubation, the balloon was inflated to expand the scaffold to its nominal, product-specific, diameter. After the expansion, the balloon was withdrawn and the scaffold was handled individually.

Individual rings from a deployed scaffold were embedded in TissueTek (Sakure), glued into screws, and then transferred to the microtome to equilibrate at -25 °C for 20 minutes. Thin sections 10 - 15 μm thick were microtomed using a glass knife in the radial direction from an as-cut subassembly using a Powertome XL (RMC Products). The thin sections were provided by Abbott Vascular.

4.5.2 Polarized light microscopy

Polarized light micrographs were acquired in a Zeiss Universal microscope at 4X or 10 X magnification through crossed linear polarizers equipped with a Canon EOS DS30 camera.

4.5.3 Wide-angle X-ray microdiffraction

Wide-angle X-ray microdiffraction experiments were performed at beamline 2-ID-D at the Advanced Photon Source of Argonne National Lab. Diffraction patterns were collected using a Mar CCD detector at distance of 119.73 mm from the sample holder. The source wavelength was 1.227 Å and the beam spot size was 0.2 μm . The diffraction

patterns were calibrated for centering and detector distance using a cerium oxide (CeO_2) standard. The thin sections were “sandwiched” between two 500 μm thick silicon nitride membranes (Silson Ltd.) placed in front of the beam using an aluminum holder. The data acquisition time was 300 seconds. Image analysis code was developed using MATLAB® and was used for data reduction to obtain radial and azimuthal intensity profiles, and to extract quantitative values for maximum intensity, crystal orientation, and crystal orientation distribution.

The thin section presented in this chapter was investigated with line scans and an area map. The line scans had a step size of 15 μm along the arms and 9.6 μm along the outer bend; the map covered an area of 40 $\mu\text{m} \times$ 20 μm with a step size of 2 μm and 4 μm in the x- and z-directions of the laboratory frame.

4.5.4 Calculation of orientation weighing factors

The following discussion is adapted from Dean *et al.*²¹

The scattered intensity from a diffraction plane depends on the orientation distribution of poles (plane normals) in the diffraction sphere (Fig. 4.12). In the experimental system described herein, the distribution arises after deformations during crimping and deployment create three different chain axes orientations.

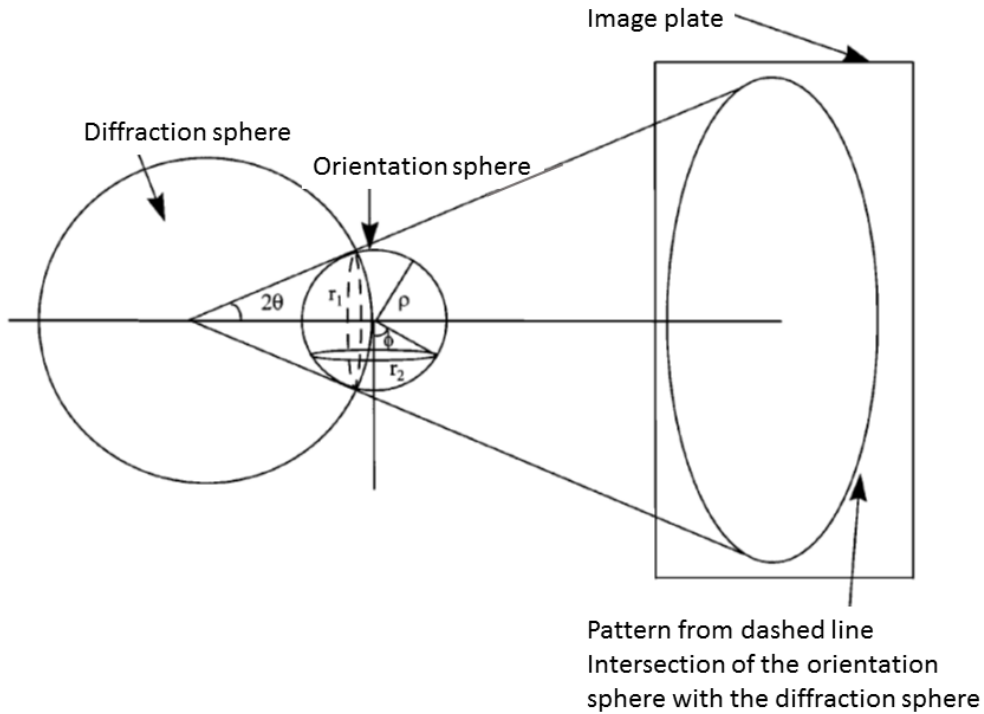


Figure 4.12 Schematic showing the X-ray scattering geometry of the intersection of the orientation sphere with the diffraction sphere (dashed circle of radius r_1 and width w). Scheme from Dean *et al.*²¹

The relative intensity of an oriented peak can be related to the intensity diffracted by an equal number of unit cells if they were isotropically distributed over the orientation sphere (i.e., a uniform distribution of poles):

$$\text{Unoriented Pole Density (UPD)} = \frac{2\pi r_1 w}{4\pi \rho^2} = \frac{2\pi f w}{4\pi \rho} \quad (4.1)$$

where r_1 represents the radius of the circle formed by the intersection of the diffraction sphere with the orientation sphere and w is the finite width of this circle, due to the variation in unit-cell dimensions; w is assumed to be the same for oriented and unoriented cases. The radius of the orientation sphere (ρ) for a particular diffraction is given Bragg's Law,

$$\rho = \frac{\sin(\theta)}{\lambda} \quad (4.2)$$

where λ is the radiation wavelength and θ is the scattering angle (see equation 4.6 below).

It is convenient to eliminate r_1 using the ratio of the radii of the intersection circle and the orientation sphere, denoted f , which is related simply to the scattering angle of the diffraction plane of interest:

$$f = \frac{r_1}{\rho} = \sin\left(\frac{\pi}{2} - \theta\right). \quad (4.3)$$

If the same number of unit cells were present with a fiber-type orientation with plane normals oriented at an angle ϕ to the fiber axis, a different fraction of them would satisfy the diffraction condition. Specifically, the whole population could then be viewed as populating a ring of area $(2 \pi r_2)$ rather than the entire orientation sphere; out of this ring, just two short segments of length w contribute to the observed diffraction:

$$\text{Oriented Pole Density (OPD)} = \frac{2w}{2\pi r_2} \quad (4.4)$$

For an equal number of unit cells, the relative diffracted intensity for crystallites having a fiber-like orientation distribution with the (hkl) plane normal at angle ϕ with respect to an axis orthogonal to the X-ray beam (Figure 4.12) compared to an unoriented distribution is

$$P = \frac{2}{\pi f \sin(\phi)} \quad (4.5)$$

Using equations 4.1 and 4.2 and $r_2 = \rho \sin(\phi)$. For the hexagonal unit cell, the value of θ for an (hkl) plane can be calculated using

$$\sin^2 \theta = \frac{\lambda}{4a^2} \left[\frac{4}{3} (h^2 + k^2 + hk) + \left(\frac{a}{c} \right)^2 l^2 \right] \quad (4.6)$$

where a , and c are the unit cell dimensions.

Using of $\alpha = 6.2 \text{ \AA}$ for the α' phase of PLLA and $\lambda = 1.2276 \text{ \AA}$ (the X-ray wavelength at APS 2-ID-D) for the (110) plane, the scattering angle is $\theta_{110} = 11.42^\circ$ and $f_{110} = 0.98$. Similarly, $\theta_{200} = 7.59^\circ$ and $f_{200} = 0.99$ for the (200) plane.

The angle ϕ is defined as the angle between the (hkl)-plane unit normal vector and the symmetry axis of the system. For a hexagonal system, such as PLLA's α' morph, the primary axis of symmetry is the c-axis.³¹ By definition, the plane unit normal of (110) is $P_{\vec{n}_{110}} = \vec{x} + \vec{y}$ and the angle between it and the c-axis unit normal ($\vec{n}_c = \vec{z}$) is 90° (Fig. 4.13). For calculation purposes, ϕ can be taken to be the (110) peak angle, Φ_{\max} .³² Using the above values, P_{110} varies from 0.918 to 0.649 for $45^\circ \leq \phi \leq 90^\circ$ and, similarly, P_{200} varies from 0.908 to 0.642 for $45^\circ \leq \phi \leq 90^\circ$. Hence, the intensity must be weighed to accurately to represent the system properties.

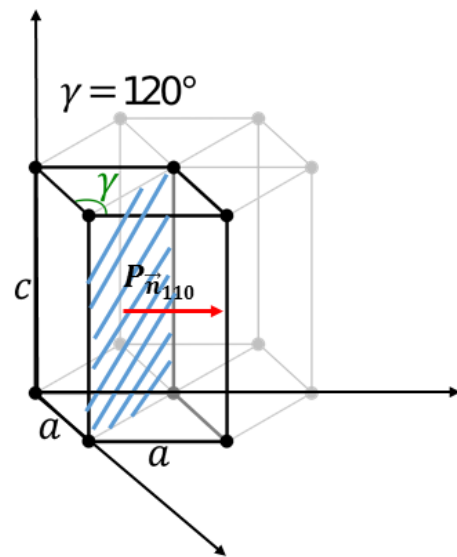


Figure 4.13 Schematic of the (110) plane (diagonal blue lines) and the plane unit normal, $P_{\vec{n}_{110}}$, (red arrow) are shown in the frame of the hexagonal unit cell.

References

- (1) Russo, R. J.; Silva, P. D.; Yeager, M. Coronary Artery Overexpansion Increases Neointimal Hyperplasia after Stent Placement in a Porcine Model. *Heart* **2007**, *93*, 1609–1615.
- (2) Aziz, S.; Morris, J. L.; Perry, R. a; Stables, R. H. Stent Expansion: A Combination of Delivery Balloon Underexpansion and Acute Stent Recoil Reduces Predicted Stent Diameter Irrespective of Reference Vessel Size. *Heart* **2007**, *93*, 1562–1566.
- (3) Sera, F.; Awata, M.; Uematsu, M.; Kotani, J.; Nanto, S.; Nagata, S. Optimal Stent-Sizing with Intravascular Ultrasound Contributes to Complete Neointimal Coverage after Sirolimus-Eluting Stent Implantation Assessed by Angioscopy. *JACC Cardiovasc. Interv.* **2009**, *2*, 989–994.
- (4) Chen, H. Y.; Hermiller, J.; Sinha, A. K.; Sturek, M.; Zhu, L.; Kassab, G. S. Effects of Stent Sizing on Endothelial and Vessel Wall Stress: Potential Mechanisms for in-Stent Restenosis. *J. Appl. Physiol.* **2009**, *106*, 1686–1691.
- (5) Martin, D.; Boyle, F. J. Computational Structural Modelling of Coronary Stent Deployment: A Review. *Comput. Methods Biomed. Engin.* **2011**, *14*, 331–348.
- (6) Squire, J. C. Dynamics of Endovascular Stent Expansion, Massachusetts Institute of Technology, 2000.
- (7) Dumoulin, C.; Cochelin, B. Mechanical Behaviour Modelling of Balloon-Expandable Stents. *J. Biomech.* **2000**, *33*, 1461–1470.
- (8) Yang, J.; Huang, N. Mechanical Formula for the Plastic Limit Pressure of Stent during Expansion. *Acta Mech. Sin.* **2009**, *25*, 795–801.
- (9) Wang, Y.; Gada, M. Polymer Scaffold with Multi-Pleated Balloon. WO 2013/173186 A1, 2013.
- (10) Mortier, P.; De Beule, M.; Carlier, S. G.; Van Impe, R.; Verhegge, B.; Verdonck, P. Numerical Study of the Uniformity of Balloon-Expandable Stent Deployment. *J. Biomech. Eng.* **2008**, *130*, 021018.
- (11) Gijsen, F. J. H.; Migliavacca, F.; Schievano, S.; Socci, L.; Petrini, L.; Thury, A.; Wentzel, J. J.; van der Steen, A. F. W.; Serruys, P. W. S.; Dubini, G. Simulation of Stent Deployment in a Realistic Human Coronary Artery. *Biomed. Eng. Online* **2008**, *7*, 23.
- (12) Lally, C.; Dolan, F.; Prendergast, P. J. Cardiovascular Stent Design and Vessel Stresses: A Finite Element Analysis. *J. Biomech.* **2005**, *38*, 1574–1581.
- (13) Harewood, F. J.; McHugh, P. E. Modeling of Size Dependent Failure in Cardiovascular Stent Struts under Tension and Bending. *Ann. Biomed. Eng.* **2007**, *35*, 1539–1553.

(14) McGarry, J. P.; O'Donnell, B. P.; McHugh, P. E.; O'Cearbhaill, E.; McMeeking, R. M. Computational Examination of the Effect of Material Inhomogeneity on the Necking of Stent Struts Under Tensile Loading. *J. Appl. Mech.* **2007**, *74*, 978.

(15) Soares, J. S.; Moore, J. E.; Rajagopal, K. R. Modeling of Deformation-Accelerated Breakdown of Polylactic Acid Biodegradable Stents. *J. Med. Device.* **2010**, *4*, 1–10.

(16) Paryab, N.; Cronin, D.; Lee-Sullivan, P.; Ying, X.; Boey, F. Y. C.; Venkatraman, S. Uniform Expansion of a Polymeric Helical Stent. *J. Med. Device.* **2012**, *6*, 021012.

(17) Agrawal, C. M.; Haas, K. F.; Leopold, D. a; Clark, H. G. Evaluation of poly(L-Lactic Acid) as a Material for Intravascular Polymeric Stents. *Biomaterials* **1992**, *13*, 176–182.

(18) Welch, T.; Eberhart, R. C.; Chuong, C.-J. Characterizing the Expansive Deformation of a Bioresorbable Polymer Fiber Stent. *Ann. Biomed. Eng.* **2008**, *36*, 742–751.

(19) Su, S.-H.; Chao, R. Y. N.; Landau, C. L.; Nelson, K. D.; Timmons, R. B.; Meidell, R. S.; Eberhart, R. C. Expandable Bioresorbable Endovascular Stent. I. Fabrication and Properties. *Ann. Biomed. Eng.* **2003**, *31*, 667–677.

(20) Grabow, N.; Schlun, M.; Sternberg, K.; Hakansson, N.; Kramer, S.; Schmitz, K.-P. Mechanical Properties of Laser Cut Poly(L-Lactide) Micro-Specimens: Implications for Stent Design, Manufacture, and Sterilization. *J. Biomech. Eng.* **2005**, *127*, 25.

(21) Dean, D. M.; Rebenfeld, L.; Register, R. A.; Hsiao, B. S. Matrix Molecular Orientation in Fiber-Reinforced Polypropylene Composites. *J. Mater. Sci.* **1998**, *33*, 4797–4812.

(22) Jang, K. S.; Kang, T. W.; Lee, K. S.; Kim, C.; Kim, T.-W. The Effect of Change in Width on Stress Distribution along the Curved Segments of Stents. *J. Mech. Sci. Technol.* **2010**, *24*, 1265–1271.

(23) Mahendrasingam, A.; Blundell, D. J.; Parton, M.; Wright, A. K.; Rasburn, J.; Narayanan, T.; Fuller, W. Time Resolved Study of Oriented Crystallisation of Poly(lactic Acid) during Rapid Tensile Deformation. *Polymer* **2005**, *46*, 6009–6015.

(24) Hébert, J.-S.; Wood-Adams, P.; Heuzey, M.-C.; Dubois, C.; Brisson, J. Morphology of Polylactic Acid Crystallized during Annealing after Uniaxial Deformation. *J. Polym. Sci. Part B Polym. Phys.* **2013**, *51*, 430–440.

(25) Stoclet, G.; Seguela, R.; Lefebvre, J. M.; Elkoun, S.; Vanmansart, C. Strain-Induced Molecular Ordering in Polylactide upon Uniaxial Stretching. *Macromolecules* **2010**, *43*, 1488–1498.

(26) Stoclet, G.; Seguela, R.; Vanmansart, C.; Rochas, C.; Lefebvre, J.-M. WAXS Study of the Structural Reorganization of Semi-Crystalline Polylactide under Tensile Drawing. *Polymer* **2012**, *53*, 519–528.

(27) Renouf-Glauser, A. C.; Rose, J.; Farrar, D. F.; Cameron, R. E. The Effect of Crystallinity on the Deformation Mechanism and Bulk Mechanical Properties of PLLA. *Biomaterials* **2005**, *26*, 5771–5782.

(28) Argon, A. S. *The Physics of Deformation and Fracture of Polymers*; Cambridge University Press, 2013; pp. 342–390.

(29) Radu, M. D.; Onuma, Y.; Rapoza, R. J.; Diletti, R.; Serruys, P. W. In Vivo Visualisation by Three-Dimensional Optical Coherence Tomography of Stress Crazing of a Bioresorbable Vascular Scaffold Implanted for Treatment of Human Coronary Stenosis. *EuroIntervention* **2012**, *7*, 1461–1463.

(30) Ormiston, J. a; Serruys, P. W.; Onuma, Y.; van Geuns, R.-J.; de Bruyne, B.; Dudek, D.; Thuesen, L.; Smits, P. C.; Chevalier, B.; McClean, D.; et al. First Serial Assessment at 6 Months and 2 Years of the Second Generation of Absorb Everolimus-Eluting Bioresorbable Vascular Scaffold: A Multi-Imaging Modality Study. *Circ. Cardiovasc. Interv.* **2012**, *5*, 620–632.

(31) Massa, W. *Crystal Structure Determination*; 2nd ed.; Springer-Verlag Berlin Heidelberg, 2004; pp. 13–31.

(32) Alexander, L. E. *X-Ray Diffraction Methods in Polymer Science*; Wiley Interscience: New York, 1969.

ⁱ Metallic self-expandable stents are also available in the market for peripheral applications (e.g. InnovaTM by Boston Scientific).

ⁱⁱ The micro-crack is identified by rotating the specimen between crossed linear polarizers. No light is refracted where discontinuities occur and the regions remain dark at all orientations.

ⁱⁱⁱ In solid mechanics, “graceful” fracture or failure refers to separation of surfaces without alteration of the material’s load-bearing capabilities.

Appendix A

Data Analysis Code

The following code was used to analyze the wide-angle X-ray scattering and microdiffraction data. I would like to acknowledge Esteban Hufstedler's advice on handling images when developing this code.

A.1 Reduction of data to acquire $I(\Phi)$

```

load S2Crimp3map1Names.mat % load the names of the data files

% experimental parameters
lamda = 1.2276*10^-10;
Np = 2048;
pixsize = 79.138 *10^-6;
xc = 988;
yc = 1060;
SaDet = 119.7321* 10^-3;
w= Np * pixsize;

% setup of matrices that will be used for the following interpolations
[X, Y] = meshgrid(1:Np, 1:Np);
X = X-xc; % rescale with center position
Y = Y-yc;
X = X*pixsize; %convert to actual distances
Y = Y*pixsize;
r = (X.^2 + Y.^2).^.5;
q = 4 * 10^-10*pi*sin(0.5*atan(r/SaDet))/lamda;

rmin = 315; % rmin and rmax define the radius for the 110/200 peak.
rmax = 370;
nt = round(2*pi*rmax); % number of phi points
nr = rmax-rmin;
phi1 = deg2rad(-90); % Full circle of phi points the with matlab's default config.
phi2 = deg2rad(270);

for i = 1:483
    im = medfilt2(imread(S2Crimp3map1Names{i}), [5 5]);
    %create the mesh in x, y that the elemens of the 2D image will be mapped on
    [x,y] = meshgrid(1:size(im,2),1:size(im,1));
    % create the mesh in phi and r

```

```

[phi, radius] = meshgrid(linspace(th1,th2,nt), linspace(rmin,rmax,nr));
xi = xc+radius.*cos(phi); % these are the cartesian coordinates of each pixel
yi = yc+radius.*sin(phi);
% 2D interpolation: interpolate the values at (xi, yi) of the original
% the image im so that each pixel corresponds to an (xi, yi) of the
% unwrapped image
unwrapped = interp2(x, y, double(im), xi, yi);
unwrapped(isnan(unwrapped)) = 0; % fill out the NaN values with zero

% The summation gives IvsPhi
IvsPhi1(:,i) = sum(unwrapped);

end

phi1 = phi(1,:)*180/pi-90 ; % azimuthal angle on detector
                           % 0 is top middle and + is
                           % clockwise

save('Crimp3map1_IvsPhi', 'IvsPhi')
save('phi1', 'phi1')

```

A.2 Extraction of quantitative values from $I(\Phi)$

```

load Crimp3map1_IvsPhi.mat
load bkg.mat % background frame
load phi1.mat
I1 = IvsPhi1;

xx = ones(3500,1);
Int = ones(3500, 483);

for i = 1: size(I1, 2)
    x = phi2;
    y = I1(:,i) - bkg;

    pp = spline(x,y); % pp form of the spline
    xx = linspace(x(1), x(length(x)), 3500)'; % xmesh
    Int(:,i) = ppval(pp, xx); % evaluate spline
    [phiMax(i), maxI1(i), w1(i)] = fwhmPhi(xx, Int(:, i));

end

```

```
% plot the data
% mesh of the data positions
z = 0:10:200; % xpos
az = 0:10:220; % ypos
Imax = reshape(maxI1, 23, 21);
fig= figure('Units','pixels','Position',[100, 400, 600, 500]);
f1 = 'Crimp3_map1_IntPhiMax';
imagesc(z, az, Imax, [0 8000])
axis image
colorbar
print(fig, f1,'-dpng', '-r300')
```

A.3 Function used to extract values from the $I(\Phi)$ curves

```
function [phi, maxI, w] = fwhmPhi(X, Y)
% phi =  $\Phi_{\max}$ ; maxI = value of maximum intensity; w = FWHM

num = numel(Y);
f = Y(num/2:end);
f = f-min(f);
x = 1:numel(f);
[maxVal,peakI] = max(f);

% determine noise levels
sf = smooth(f,5);
noiseLevel = std(f-sf);
maxs = max(sf);
mins = min(sf);

% use S/N to determine outliers
if (maxs-mins)/noiseLevel > 120
    halfMaxVal = maxVal/2;
    halfMaxX1 = round(interp1(f(1:peakI),x(1:peakI),halfMaxVal));
    halfMaxX2 = round(interp1(f(peakI:end),x(peakI:end),halfMaxVal));
    w = X(halfMaxX2) - X(halfMaxX1);
    phi= X(peakI + num/2);
    maxI = maxVal;
elseif (maxs-mins)/noiseLevel <= 120
    w = 40;
    phi= 0;
    maxI = 0;
end

end
```